

Atomic force microscopy study on the mechanics of influenza viruses and liposomes

Dissertation

for the award of the degree

“Doctor rerum naturalium”

In the program of Physics of Biological and Complex Systems

Göttingen Graduate School for Neurosciences, Biophysics, and Molecular Biosciences

of the Georg-August-Universität Göttingen

submitted by

Sai Li

from **Hubei, China**

Göttingen, 2012

Members of the Thesis Committee

Dr. Iwan A.T. Schaap (Reviewer, Examination board)
Atomic Force Microscopy group at the III. Physikalisches Institut
Faculty of Physics

Prof. Dr. Andreas Janshoff (Reviewer, Examination board)
Institute for Physical Chemistry
Faculty of Chemistry

Prof. Dr. Christoph F. Schmidt (Examination board)
III. Physikalisches Institut
Faculty of Physics

Prof. Dr. Jörg Enderlein (Examination board)
III. Physikalisches Institut
Faculty of Physics

Prof. Dr. Sarah Köster (Examination board)
Institute for X-Ray Physics
Faculty of Physics

Prof. Dr. Bert de Groot (Examination board)
Computational Biomolecular Dynamics Group
Max Planck Institute for Biophysical Chemistry

Date of oral examination: November, 2012

I, Sai Li, hereby certify that my doctoral thesis entitled "Atomic force microscopy study on the mechanics of influenza viruses and liposomes" has been written independently and with no other sources and aids than quoted.

Signature:

Sai Li 李璿

Table of contents

Abbreviations	1
Abstract	3
1. introduction.....	5
1.1. Viruses.....	5
1.1.1. The structure, activity and mechanics of viruses.....	5
1.1.2. Influenza A virus.....	13
1.2. Small unilamellar vesicles	24
1.2.1. Lipid bilayers and liposomes	24
1.2.2. Mechanics of lipid bilayers.....	25
1.2.3. Parameters that influence the mechanics of lipid bilayer	28
1.3. Atomic force microscopy	31
1.3.1. General introduction.....	31
1.3.2. AFM cantilever calibration.....	33
1.3.3. Application of the AFM: imaging	37
1.3.4. Application of the AFM: Mechanics.....	39
1.3.5. Tip shape characterization and tip-induced image artifacts.....	41
1.3.6. Outlook of novel AFM methods.....	43
2. Mechanics of liposomes	45
2.1. Introduction to the experiments	45
2.2. Materials and methods.....	47
2.3. Results.....	54
2.3.1. Mechanics of liposomes made from pure lipids.....	54
2.3.2. Mechanics of liposomes made from myelin lipids.....	55
2.3.3. Mechanics of liposomes made from influenza viral lipid	57
2.4. Discussion.....	70
3. Mechanics of the influenza A virus	73
3.1. Introduction to the experiments	73
3.2. Materials and methods.....	74
3.3. Results.....	76
3.3.1. Morphology of influenza viruses.....	76
3.3.2. pH-controlled unpacking of Influenza virus	77

3.3.3.	Both softening steps are required for complete virus disassembly	83
3.4.	Discussion.....	87
4.	Appendices	91
4.1.	Nano-particle size determination	91
4.1.1.	Dynamic light scattering	91
4.1.2.	Viral particle size determination by single virus tracking	92
4.2.	Characterization of AFM tip induced image artifacts	101
4.2.1.	Tip shape characterization.....	101
4.2.2.	Shape dilation function calculation.....	103
4.3.	Low force mechanical measurements with AFM and optical tweezers	105
4.3.1.	Mechanics of the cell membrane by AFM pulling experiments	105
4.3.2.	Mechanics of cells by optical tweezers pushing	108
	References.....	113
	Curriculum Vitae	125
	Acknowledgements	129

ABBREVIATIONS

AFM: Atomic force microscopy

CCMV: Cowpea chlorotic mottle virus

CCPs: Clathrin coated pits

Cm1: Cellular export factor

CME: Clathrin-mediated endocytosis

cRNA: Complimentary RNA

DAPI: 4',6-diamidino-2-phenylindole

DETA: 3-[2-(2-Aminoethylamino)ethylamino] propyltrimethoxysilane

DMPC: 1,2-dimyristoyl(d54)-sn-glycero-3-phosphocholine

DOPC: 1,2-dioleoyl-sn-glycero-3-phosphocholine

DSC: Differential scanning calorimetry

EE: Early endosome

EM: Electron microscopy

FDQ: Fluorescence dequenching

FEM: Finite element methods

FZ: Force-distance

GUV: Giant unilamellar vesicle

HA: Hemagglutinin

HIV: Human immunodeficiency virus

HOPG: Highly ordered pyrolytic graphite

HSV: Herpes simplex virus

LE: Late endosome

MDCK: Madin-darby canine kidney

mRNA: Messenger RNA

MSD: Mean square displacement

MVM: Minute virus of mice

N.A.: Numerical aperture

NA: Neuraminidase

NP: Nucleoprotein

PA: Polymerase acidic protein

PB: Polymerase basic protein

PBS: Phosphate buffered saline

PSD: Power spectral density

PTA: Phosphotungstic acid

RES: Reticuloendothelial system

RNP: Ribonucleoprotein

SDE: Stochastic differential equation

SEM: Scanning electron microscopy

SFV: Semliki forest virus

SHO: simple harmonic oscillator

STED: Stimulated emission depletion microscopy

SUV: Small unilamellar vesicle

TMV: Tobacco mosaic virus

tRNA: transfer RNA

vRNA: Viral RNA

VSV: Vesicular stomatitis virus

WT: Wild-type

ABSTRACT

Physics exists wherever there is matter: measures such as energy, mass, temperature, speed, dimension and stiffness are all examples of the physical properties. Such quantities are important characterizations for biological organisms: they are changing all the time during the life cycle. For a bio-mechanist, stiffness is an important measure to understand biological design. Because biological building blocks can be as small as 1 nm (protein/DNA/lipid), special techniques are required to study their stiffness. Both atomic force microscopy (AFM) and optical tweezers can be used to actively deform the objects at pN-nN forces and measure the deformation on nanometer length scales. In this thesis AFM is applied to study the mechanics of influenza viruses, liposomes and living cells.

The genome of viruses is packed by a protein shell and in some cases an additional lipid envelope. This composite shell has conflicting roles: it has to protect the viral genome, but it should also allow unpacking during the viral infection to release the genome. Influenza virus is the softest virus ever found, but at the same time a very persistent virus causing yearly pandemics. A better understanding of the mechanical properties of influenza virus may help us to understand why this virus is so successful. The mechanical properties of influenza viruses were measured by AFM and compared with the liposomes made of the viral lipid. We have found that, the influenza virus mechanics are dominated by its lipid envelope (~70%). In chapter 2 we proved that instead of using a rigid protein capsid, the lipid envelope is sufficient to protect the influenza viral genome. In chapter 3, we further looked into the function of the M1 protein shell during viral infection. An intermediate unpacking step was discovered by measuring the influenza viral stiffness at pH 7, 6, 5.5, and 5, conditions that mimic the acidifying environments on the viral infection pathway. The intermediate step was further proven to be essential for successful infection. We propose that the influenza virus has evolved to tightly synchronize the different steps of its unpacking with pH changes in its biological environment while traveling through the cell.

By carrying out the aforementioned investigations, I have increased our understanding of how the influenza virus protects itself and how the virus structure disassembles in multiple steps during infection. The methods described in this thesis are innovative and will also be useful for the mechanical characterization of other samples. The results are also important from a virological point of view, since they indicate that enveloped viruses taken up by endocytosis may have to undergo a gradual acidification in order to reach infectivity.

1. INTRODUCTION

1.1. Viruses

1.1.1. The structure, activity and mechanics of viruses

Virus structure

A virus is an infectious micro-organism which depends on the living cells to reproduce itself. Viruses have probably existed since the first living cell has evolved, and are infectious to almost all kinds of living organisms (1). The morphology of viruses can be very different, from long rod-shaped (e.g. Tobacco mosaic virus (TMV), ~300 nm in length and ~18 nm in diameter); to mosquito-shaped (e.g. Bacteriophage T4, 90 nm wide and 200 nm long); to bullet-shaped (e.g. Vesicular stomatitis virus (VSV), 70 nm wide and 180 nm long). However, the majorities are quasi-spherical. Commonly, the dimension of viruses is between 20-300 nm. Recently giant viruses were discovered with diameters of 400 nm (Mimivirus) (2) and even 440 nm (Megavirus) (3).

The basic structure of viruses usually consists of viral nucleic acid encapsidated by a shell. Viruses can be differentiated into enveloped and non-enveloped depending on the composition of the shell. The shell of an enveloped virus consists of a protein layer and a lipid envelope, the latter is inherited from the host cell membrane. The lipid envelope also contains the spike proteins, which are essential for virus binding to the cell surface. The shell of a non-enveloped virus only consists of a protein capsid. Of all the non-enveloped virus capsids, icosahedral symmetry is very typical. The simplest example of icosahedral capsids is an icosahedron, which consists of 20 identical equilateral triangular faces, 30 edges and 12 vertices. The minute virus of mice (MVM) possesses an icosahedron capsid (4), which has on each vertex a capsomer (capsid subunit), each capsomer contains 5 identical capsid protein unit. However, most icosahedral viruses possess more complicated capsids, which consist of both hexamers and pentamers, and in total more than 60 capsid protein units. To classify the icosahedral symmetry types, *Casper* and *Klug* invented the quasi-equivalence principle (5):

$$T = h^2 + h * k + k^2 \tag{1.1.1}$$

where T is the triangulation number, h and k are positive integers.

Hence T can only be a limited number of integers as: 1, 3, 4, 7, 8,... Any icosahedral capsid contains a fixed number of 12 pentamers and 10(T-1) hexamers. For example, the cowpea chlorotic mottle virus (CCMV) is a T=3 virus, which contains 12 pentamers and 20 hexamers and in total 180 capsid protein units. Forming from identical sub-units, the designs of the capsids are shown in **Fig 1.1.1**.

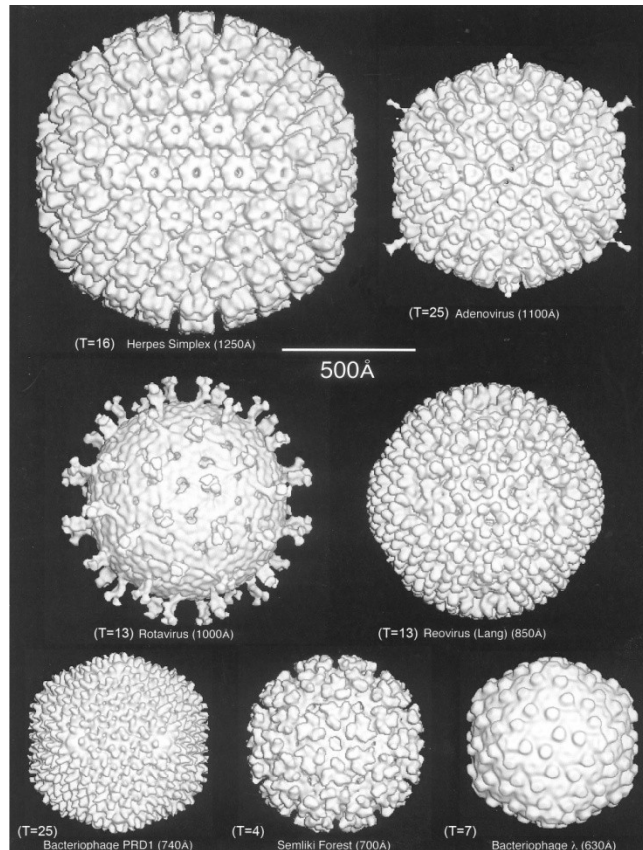


Fig 1.1.1 Gallery of representative icosahedral viruses reconstructed from cryo-EM images, the triangulation number T is shown for each virus. All virus structures which surface is shaded are viewed along a twofold axis of symmetry. The HSV is reconstructed from its icosahedral core only. The image is taken from (6).

Viruses are so small that they are beyond the resolution of most optical microscopy methods. The electron microscopy (EM) is usually applied to image viruses, aiming at resolving fine structure of their organization. Instant freezing techniques are commonly applied on viruses before imaging them in EM, in order to fix the sample without damaging the structure. In some cases heavy metal staining methods are applied to obtain better contrast. A good example is the observation of the herpes simplex virus (HSV) uncoating using EM (**Fig 1.1.2**), in which both heavy metal staining and frozen-hydration method were applied (7). Better resolution of the viral protein structure may be achieved by means of X-ray crystallography. Viral proteins are first crystallized and the diffraction pattern of the X-ray is used to reconstruct the viral protein structure. For example, the structure of bacteriophage P29 packaging motor protein was successfully resolved by X-ray crystallography. The structure was used to explain the mechanism of the motor in packaging and releasing the double stranded DNA (8). The same technique was applied to find the changes in influenza M1 protein structure at neutral and acidic pH (9). Both EM

and crystallography have strong resolving power in discovering details of the virus; however, the methods are also subjected to tedious sample preparation, which has the risk of damaging the sample. For example, the difficulties of crystallography lie in 2 aspects. Firstly, the crystallization of protein is sometimes very difficult, especially when the protein is large and possesses long chains. Secondly, the crystallization can also be selective, since by forcing the proteins in a crystal, it is likely that the crystallization-favorable conformations will be best presented instead of the real conformations in the virus. One drawback of EM is the intensive image postprocessing work. For example, a high resolution EM image usually comes from the overlay of thousands of images, therefore the parts that have a variable structure cannot be resolved.

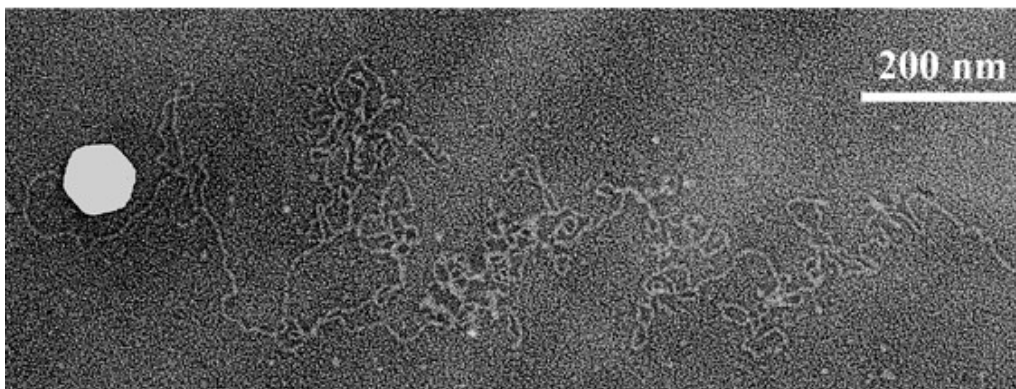


Fig 1.1.2 Electron micrograph shows a HSV-1 C capsid releasing its DNA. The image is taken from (7).

Virus entry and replication

Viruses are incapable of reproducing themselves without the host cell machinery. They were found in almost all living organisms, ranging from bacteria, yeast, plants to animals. The life cycle of a virus is simple: the only mission in its life is to replicate itself. Viruses cannot do this on their own, as compared to most other species; they need the aid of other organisms, e.g. cells. They use different strategies to send their genome into the cell, where thousands of copies are multiplied and finally leave the host cell ready to infect other cells. The infection usually leads to the death of cells and inflammatory response in the host organisms, and consequently causes symptoms. Studying the infection of viruses is of great importance: not only to understand the viral life cycle, but also to provide methods of prognosis, vaccination, and treatment.

Although some viruses are small enough to penetrate the cell membrane (e.g. Parvovirus), most of them depend on cell endocytosis. The type of endocytic uptake can be differentiated by the type of cell

proteins involved (10). Of all the endocytic mechanisms, the clathrin mediated endocytosis is one of the most common methods, which is also adopted by the influenza virus.

The viral replication process in eukaryotic cells is different between enveloped and non-enveloped viruses, probably due to their difference in size as well. Non-enveloped viruses are usually smaller (20-50 nm) which allows them to enter the cell nucleus directly. They mature as early as in the cytoplasm (e.g. picornaviruses) or the nucleus (e.g. adenoviruses) and then disintegrate the host cell. Enveloped viruses are usually larger (50-300 nm), they have to unpack to release the genome before the endosomes (which ferry the viruses to the perinuclear region) merge with the lysosomes.

Enveloped viruses are assembled before budding from the cell. During budding, their nucleocapsids together with the genome bind to the regions of the host cell membranes where their surface proteins are inserted, and then they form a bud into the extracellular space and depart. To show differences in viral replication, typical entry and uncoating mechanisms of 6 viruses are shown in **Fig 1.1.3**.

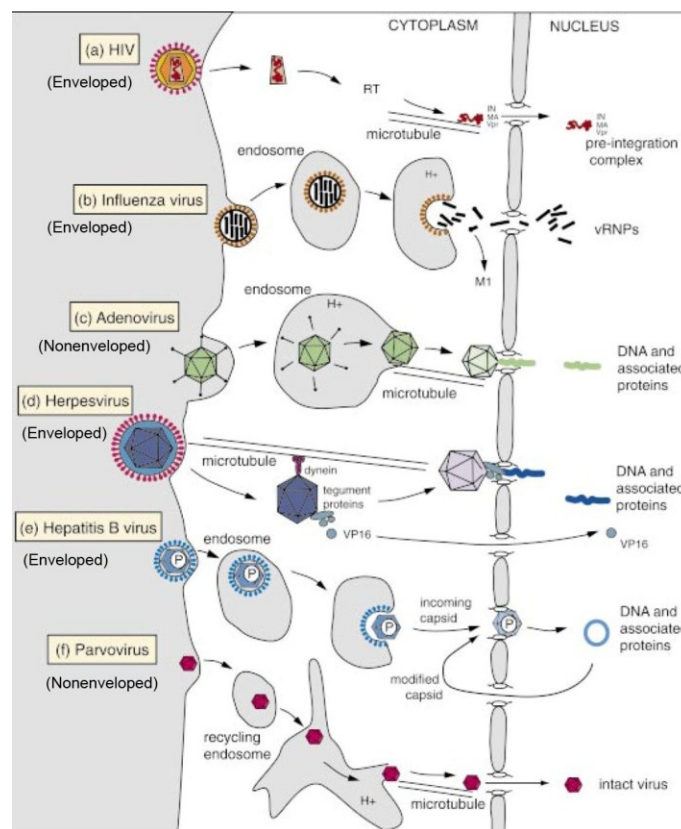


Fig 1.1.3 Typical entry and uncoating mechanisms of 6 types of viruses, of which 4 are enveloped, 2 are non-enveloped. (a) The human immunodeficiency virus (HIV) and (b) influenza virus first unpack in the cytoplasm and then release the genome into the cell nucleus; (c) adenovirus and (d) HSV dock to the

nuclear pore complexes on the surface of the cell nucleus and unpack the genome; (e) hepatitis B virus may disassemble in the nuclear pore; and (f) parvovirus is small enough to enter the nucleus directly. The image is taken from (11).

Although various strategies were found to be employed by viruses for infection and replication, they share some common distinguishable steps. Taking the example of the influenza virus, the infection steps can be distinguished as 1) Binding: influenza virus binds to the sialic acid receptors on the cell surface by its glycoprotein spikes. 2) Entering: the virus is then taken into the cell cytoplasm by endocytosis. 3) Unpacking: triggered by the low pH in the late endosomes, the virus unpacks itself and releases its genome. 4) Replication: the genome is reproduced in the cell nucleus. 5) Assembly: viral proteins are assembled by the cell's ribosomes. 6) Budding: the proteins and genome are finally assembled in the cell periphery, and buds out of the cell. The lipid envelope of the influenza virus is inherited from the cell membrane at this time. The details of these steps will be enriched in the influenza virus section.

Virus mechanics

Viruses are masterpieces of nano-engineering. They use their shells (protein capsid or protein capsid and lipid envelope in case of enveloped viruses) to protect the genome from being damaged during their travel extracellularly. For most viruses, their protein capsids reveal minimalistic and highly symmetric architecture. Despite this simplicity, the design is sufficient for genome protection, viral infection and replication. The shell must fulfill contradictory roles: it shall be strong and flexible enough against pressure, mechanical deformation and certain environmental variance, such as temperature and pH. For example, the internal genome pressure of bacteriophages and many other dsDNA viruses reaches tens of atmosphere: so that their genome can be ejected into the cell after attaching to the cell surface; yet the pressure has to be sustained by the shells before infection (12). The shell shall also be unpackable so that during infection the viral genome can be released. For example, triggered by low pH in the endosomes, influenza viruses unpack their protein capsid and lipid envelope, their vRNPs are released and enter the nucleus. The mechanical studies of the viral structure are helpful in understanding the organization of the viral shells, their responses to environmental changes, and correlation between the viral mechanics and viral functions in their life cycle.

There are multiple ways to study the mechanics of virus. First example is the osmotic shock method, by which bacteriophages were first incubated in high salt solutions and quickly diluted. Upon dilution, phages with capsids which are more permeable to water than to metal ions will burst. The T2, T4 and T6 phages were found to be easier to break, whereas T1, T3, T5 and T7 phages remained intact when exposed to the same treatment (13). The mechanics of crystals formed from viruses were examined by Brillouin light-scattering (14). The aforementioned methods were performed on samples with a large number of particles and gained information over the average behavior; also the direction-dependent mechanical information was lost due to the inhomogeneity of the sample. New mechanical methods such as optical tweezers were performed to study single viruses. For example, one bead bound to a DNA

molecule and another bead to a bacteriophage Phi29 prohead were trapped by two laser beams (or 1 trap and 1 micro pipette). By approaching the beads, the packing motion and force of DNA by the viral motor was recorded by the optical tweezers. 10 bp step size was resolved (15); the motor can work against a force of up to 57 pN on average, which is one of the strongest molecular motors reported (16). Due to the limited resolution of the optical microscopy, such measurements are usually invisible, but the forces and displacements can be deduced from the diffracted laser beam from the trapped beads (17).

AFM provides a direct way to image and probe a single virus. As will be described in details in section 1.3, an AFM image is made by touching the sample with a very sharp tip, and has the resolution down to 1 nm in liquid. Protein organization on the surface of the virus can be clearly visualized by AFM, as was shown on mimivirus (18), vaccinia virus (19) and MVM (20). It is not only capable of imaging, but also of manipulating the viruses. The first mechanical investigation with AFM on a virus appeared in 1997, when *Falvo et al.* manipulated TMV with an AFM (21). The rod-like TMV, with ~300 nm in length and ~18 nm in diameter, was shown rotated, dissected and translated by an AFM tip. Using beam theory (**equation (1.3.2)**), the axial Young's modulus (1.1 GPa) of the virus was calculated. Later in 2004, mechanical properties of viruses were shown to be directly measurable by performing point force indentation on the bacteriophage Phi29 by the AFM tip (12). Since then, the method has been applied to study more than 10 kinds of viruses, including HSV (22), bacteriophages (23, 24), CCMV (25) and HIV (26). The majority of viruses, enveloped or not, were found to be as stiff as 0.2-1 N/m (12, 25, 26). The stiffness is usually converted to material properties (e.g. Young's modulus) via mechanical modeling (analytical or finite element methods) to enable better understanding of the viral protein shell. The Young's moduli of most viruses were found to be around 1 GPa (27), comparable to that of polypropylene (soft plastic material). Excellent reviews of AFM investigation on virus mechanics are available (13, 27, 28).

The AFM study on the viral mechanics was initiated to investigate the material properties of the viral shell and to understand how the shell manages to protect the viral genome. For example, the first of such studies measured the distribution of the elastic constant over a bacteriophage Phi29 capsid, which reflected the protein distribution on the surface, and punctured the capsid on purpose to see the limits of the protection (12). Similar work has been applied to HSV (22). In later studies, the viral stiffness was measured at different conditions and the differences were correlated to viral activities. For example, the stiffness of mature and immature HIV was measured. The significant difference between the two indicates a major conformational change when HIV viruses develop from the immature to the mature state (26). In the case of MVM, different orientations of MVM could be clearly resolved, and the stiffness of the virus was found to be dependent on these orientations (**Fig 1.1.4**).

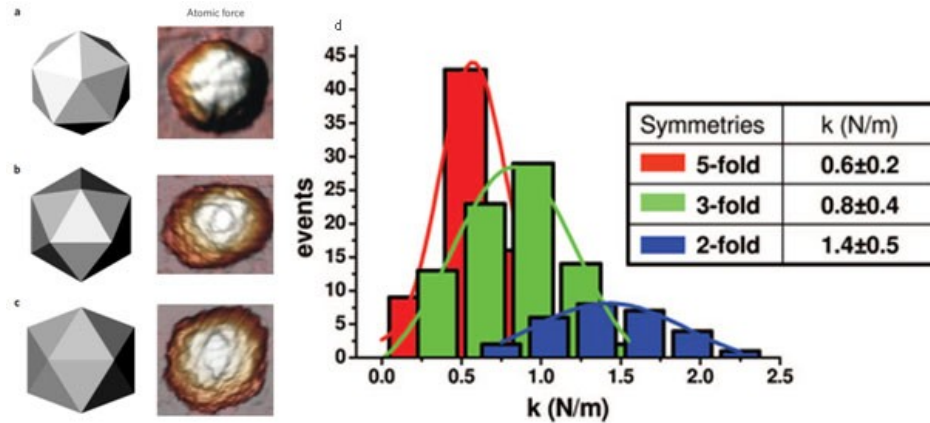


Fig 1.1.4 The MVM particles as viewed along fivefold (a), threefold (b), and twofold(c) symmetry axes, and the viral stiffness dependence on the symmetries. (Left) Simplified models. (Right) AFM images of MVM showed clear correspondence to the model. (d) Depending on the symmetries, the MVM virus exhibited different stiffness. The image is taken from (20).

Summarizing this, AFM is a powerful tool in decoding the nano-world, and enables nano-indentations at forces from tens of piconewton to nanonewtons. For this thesis, I explored the mechanics of the influenza virus.

Mechanics of influenza A virus

As mentioned before, the stiffness of most viruses was found to be 0.2-1 N/m (12, 25, 26). However, the stiffness of influenza virus was found to be significantly less, at least ten folds softer compared to most other viruses (29). The influenza virus stiffness is almost identical to that of its lipid envelope alone. Despite its softness, it is sufficient to survive even when subjected to high magnitude of deformation (30), or dehydrated for days on banknotes (31). What mechanisms are used by the influenza virus to protect itself? This was the initial impulse of our work. The comparison of mechanical properties of viruses is shown in **Fig 1.1.5**.

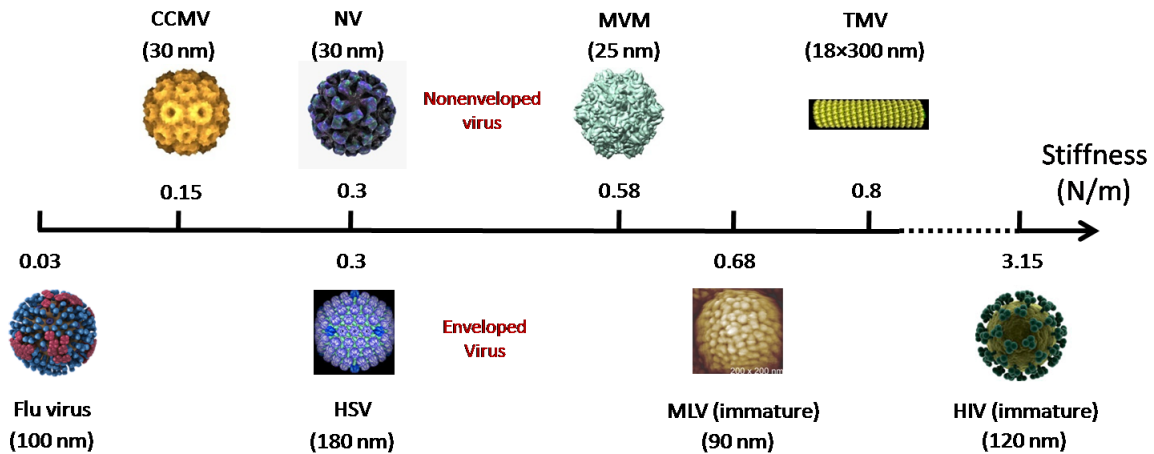


Fig 1.1.5 Scalar representation of the stiffness of viruses. For comparison, the non-enveloped viruses are listed above the scale, the enveloped viruses are listed below. The viruses are not presented according to their dimensional scale, however, their approximate diameters are given. The influenza virus is clearly the softest virus ever found. The data used to construct this representation is taken from (32).

Positive roles of viruses

Viruses do not always play a negative role by threatening the health of all living organisms. Novel applications based on the modification of viruses were made to improve drug delivery and inspire new biomaterials. For example, virus-like-nanocontainers were designed to deliver drugs to the cell (33-35). These containers are especially good at targeting the pathological cells by binding to specific receptors on the cell surface to release drugs. These modified viruses can even be designed to move on to other cells where the process can be repeated to release more drugs (34). Moreover, a considerable amount of biomaterial applications based on the arrangement of viruses (36, 37) was developed. Most of these applications, either based on single viruses (virus-like-nanocontainer) or on an assembly of viruses (virus-inspired-material), require investigation of the mechanical properties of the material to improve their stability and study their environment-dependent activities. For example, the stiffness of newly designed piezoelectric energy generating material constructed from M13 bacteriophage was investigated by AFM (38).

Viruses also play an important role in increasing the genetic diversity in a population. By infection, genes can be transferred by viruses from one species to another, resulting in an increase of genetic diversity among the host organisms which is essential for their adaptation to different environments and facilitates their evolution. A good example showing the bacteriophage's role as gene transfer agent is given in (39).

1.1.2. Influenza A virus

In general

The earliest description of an influenza virus caused epidemic was probably in 412 BC, described by Hippocrates (40), therefore the virus has been with us for at least 2400 years. Of all the catastrophes caused by influenza carved in human history, the 1918 Spanish flu pandemic was the most severe one, which lead to estimated 50 million deaths worldwide. The influenza is also fatally infectious to many animal species, e.g. chicken, swine and birds. The consequences usually leads to huge economic and ecological threats. Even today, the mortality toll caused by influenza still ranks the third worldwide, almost double as high as HIV, according to the data showed by the World Health Organization (**Fig 1.1.6**).

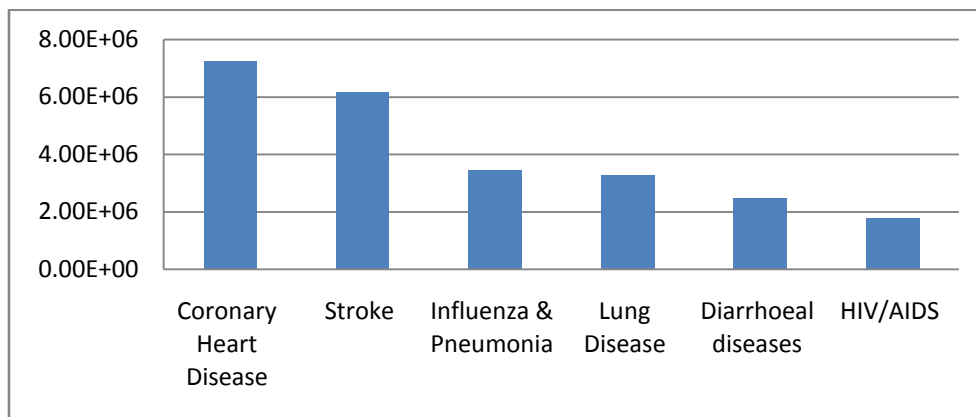


Fig 1.1.6 World's mortality toll ranking (2010), sorted by causes of death. The data is taken from WHO.

Influenza viruses are mostly observed as spherical particles, although some species show a filamentous or irregular shape. Their diameters are around 100 nm. As is shown in **Fig 1.1.7**, influenza virus is coated with an envelope of lipid bilayer. Beneath the envelope lies a protein matrix called M1. Two kinds of glycoprotein called hemagglutinin (HA) and neuraminidase (NA) are embedded in the lipid envelope, of which tails are interacting with M1 (41). Besides HA and NA, M2 proteins perforate through the viral shell, and serve as the ion channel of the virus. The viral genomes that consist of the RNA molecules are bound to eight rod-like segments of ribonucleoprotein (RNP), which contain 12000-15000 nucleotides in total.

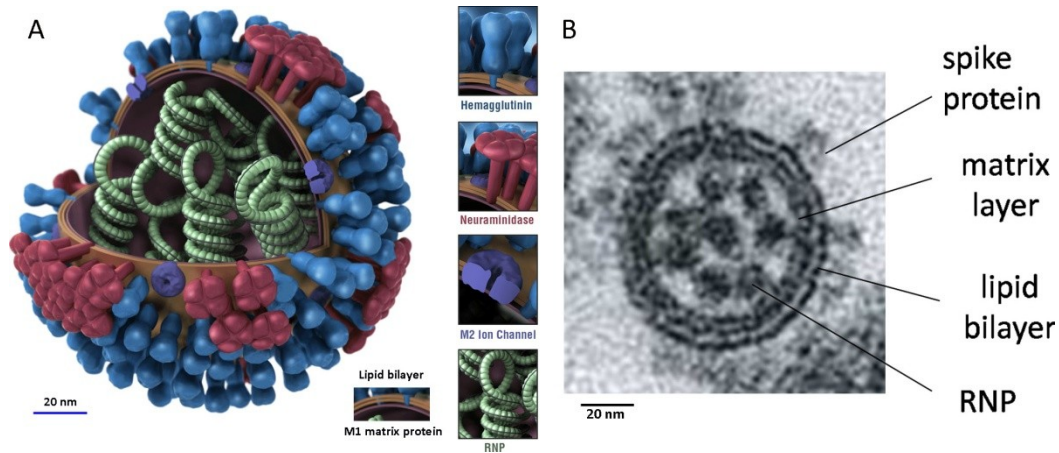


Fig 1.1.7 Anatomy of influenza A virus. (A) Cartoon of influenza A virus. The components of influenza viruses: spike proteins (HA and NA), lipid bilayer, M1 matrix protein layer, M2 ion channel proteins and ribonucleoproteins are indicated in the inserts. This image is reproduced from Center for Disease Control and Prevention. (B) EM image of influenza A virus clearly showed eight rod-like RNPs, and other components. This image is taken from (42).

Taxonomy

Influenza virus, together with isavirus, thogotovirus and the newly discovered quaranfil, Johnston atoll, and Lake Chad viruses comprise the family of Orthomyxoviridae. The viruses of the Orthomyxoviridae family have negative-sense, single-stranded and segmented RNA genomes. There are three types of influenza viruses: influenza A, B and C virus. Influenza A and C viruses are infectious to multiple species, while influenza B virus is almost exclusively infectious to human. The virus type studied in this thesis is the Influenza A virus. Only influenza A virus is further categorized by subtypes according to the two main surface glycoproteins HA and NA. There are 17 known types of HA and 9 types of NA based on their antibody responses, the subtypes are named by the combination of them. For example, H1N1 refers to an influenza virus subtype which surface spike proteins consist of HA1 and NA1. Although any combination of HA and NA is possible, only a few of the subtypes are found to be infectious to human: H1N1, H1N2, H5N1 and H3N2. The glycoproteins HA and NA are important antigens for immune system recognition.

Being a RNA virus, the influenza virus reproduces itself based on its negative-strand vRNA. During the replication process, the negative strand RNA is transcribed into positive-strand messenger RNA (mRNA) and complementary RNA (cRNA). The former is sent to ribosomes to be translated into proteins; the latter stays in the nucleus to serve as template to replicate the viral RNA (vRNA). Since the RNA polymerase enzymes does not perform proofreading, the vRNA \leftrightarrow cRNA transcription results in very high error probability: approximately 1×10^{-3} to 8×10^{-3} substitutions per site per year (43). Therefore the influenza virus is evolutionarily dynamic and is continuously evolving. The influenza viruses change in

two different ways: antigenic drift and antigenic shift (44). The antigenic shift, which happens only occasionally, refers to a sudden change of HA or NA, and new subtypes of influenza viruses are “born” as a consequence. The more common way of evolving is called antigenic drift, by which only small changes occur on HA or NA. For example, the H1N1 influenza virus strain which causes the pandemic in 2009 is different from the H1N1 strain during the 1918 Spanish flu. The antigenic drift happens all the time, and has resulted in thousands of slightly different strains in each subtype, and millions of strains in total. In this thesis, the type/subtype/strains of influenza viruses we studied are: A/H1N1/X-31, A/H1N1/PR8, A/H1N1/Japan and A/H3N2/panama.

Functions of the viral components

Although the influenza virus is composed of only a few different components, each of them is essential in the viral life cycle. The two surface glycoproteins (HA and NA) of the influenza A virus represent respectively about 85 and 15% of the surface spike proteins: there are approximately 300 HA and 40 NA spikes on the surface of each spherical virus (45). The glycoprotein HA is a trimeric rod-like molecule, which is approximately 13.5 nm in length (46). Its tail inserts into the viral lipid envelope, interacting with M1 (41), and its hydrophilic end points like a spike out of the viral body. Three spherical heads containing the sialic acid binding sites are located at the tip of the three monomers. Two proved functions of HA are binding to the sialic acid cell receptor and initiation of fusion with the target membrane, which description will be enriched in the following section. A model of HA is shown in **Fig 1.1.8 A**. NA is a tetrameric rod-like molecule, which is approximately 16 nm in length (47). Similar to HA, the cytoplasmic tail of NA is also inserted in the viral membrane and interacts with M1. NA is essential in viral budding, as it scissors the sialic acid receptor from HA and prevents self-aggregation of viruses and reattachment to the cells (48). The third surface protein is M2, which serves as the ion channel of the virus and controls the flow of protons. The activity of M2 is regulated by pH, it opens up around pH 6 ($\text{pH} \sim 6-6.5$) (49) and remains open at lower pH values.

The lipid bilayer envelope of the influenza virus is derived from the membrane of the infected cells. It is a harbor for the anchoring of HA, NA and M2. We also quantified its role in the protection against different environmental changes. (Although for HIV, the lipid envelope was found to have an additional function: The glycosphingolipids in the virus envelope are also involved in triggering dendritic cell recognition (50).) Beneath the viral envelope, the M1 matrix forms another layer around the vRNPs. The M1 matrix is constructed from the lateral arrangement of single M1 proteins, which are dimers and 6 nm × 3 nm × 3 nm in dimension (**Fig 1.1.8 B**) (51). It is the most abundant protein of the virus, and has many functions. Firstly, it serves as a bridge between viral internal and external components, interacting with HA, NA on the outer layer (41), and with vRNPs on the inner layer (52). Many works reported the insertion of M1 into viral membranes (53-55), while the observation was questioned by others (56). Secondly, M1 was found to be essential during the vRNP entry and exit in and out of the cell nucleus (52) as well as during assembly and budding (57). Lastly, besides its role as a mediator, M1 serves as the skeleton of influenza virus. It bends the viral membrane from inside and confines the shape of the virus (58). In some strains, the M1 protein exhibits a helical arrangement (58). The RNA of the influenza A

virus is segmented into 8 pieces, containing 11 genes (HA, NA, NP, M1, M2, NS1, NEP, PA, PB1, PB1-F2, PB2). The influenza C virus has only 7 pieces of RNA segments, which encode 9 proteins. The vRNAs are coated by nucleoprotein (NP). Three polymerase subunits, namely polymerase acidic protein (PA), polymerase basic protein 1 (PB1) and polymerase basic protein 2 (PB2) are associated to the NP, forming a panhandle structure. The unit containing NP, PA, PB1 and PB2 is called a mini ribonucleoprotein. Multiple RNPs stack together and form a helical structure called ribonucleoprotein complex, which is ~10-20 nm in width, 30-150 nm in length (42). vRNP is functional in importing the RNA into the cell nucleus by interacting with the nuclear pore proteins (59).

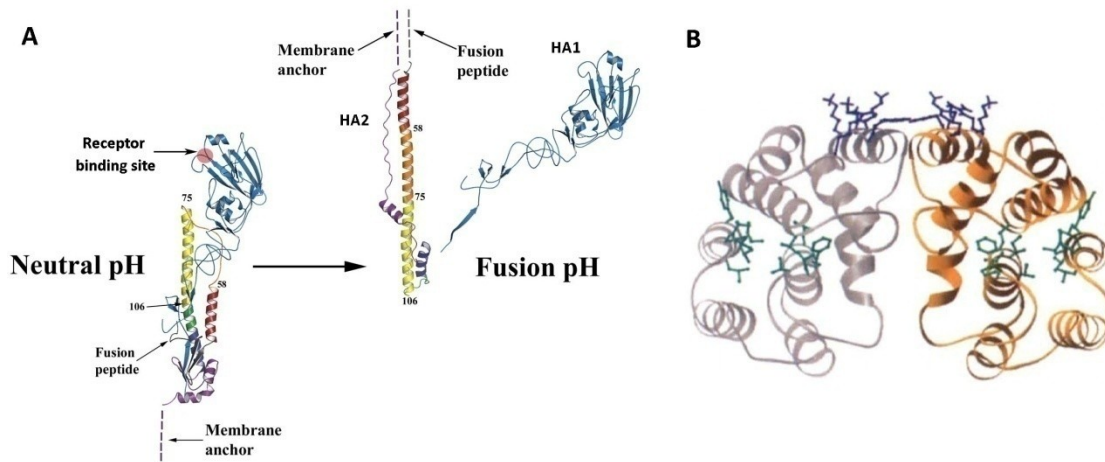


Fig 1.1.8 (A) Molecular structure of a hemagglutinin monomer from X-31 influenza virus at neutral (left) and after incubation at fusion pH (pH 5) (right). Arrows show the receptor binding site, membrane anchor and fusion peptide. At fusion pH, the HA unfolds into two parts: HA1 and HA2, the fusion peptide is exposed. The numbers 58, 75, and 106 are the HA2 residues at which position the HA refolds itself at fusion pH. The image is reproduced from (60), which is obtained by X-ray crystallography. (B) Molecular structure of a single M1 protein dimer. The image is taken from (51).

Influenza infection process

As the main work presented in this thesis is about the unpacking of influenza virus during infection, it is inevitable to describe its entire infection process in detail, by which one would have a better impression about how the components of the virus and host cell function together to achieve successful infection. Meanwhile, the infection pathway of the influenza virus shares great similarity to that of other enveloped viruses (**Fig 1.1.3**); therefore it can be considered as a model for the studies of other viruses.

The replication of influenza virus only occurs in living cells (61), to be more specific, epithelial cells in the respiratory tract (nose, throat, and lungs) of mammals, and the intestines of birds (62). The symptoms of influenza are commonly known as fever, headaches and fatigue, which are dependent on the subtype of influenza virus. For example, H1N1 infects the epithelial cells in the upper part of the respiratory tract, such as in the nose, throat and mouth; it spreads easily but is less fatal. However, H5N1 mostly infects the epithelial cells deep in the lungs; natural H5N1 does not spread between human, but once infected, it is often fatal (63). More and more attention, both scientific and public, are paid to the “dangerous” H5N1, especially when two recent reports indicate that, if artificially mutated, H5N1 can be transmissible and infectious between ferrets, and may be between humans (64, 65).

The infection steps of an influenza virus can be distinguished as 1) Binding, 2) Entering, 3) Unpacking, 4) Replication, 5) Assembly, and 6) Budding.

1) Binding and signaling: The first step of infection is binding to receptors and triggering cellular signaling for the sake of viral entry. Both factors contribute to the effectiveness of viral infection. After receptor binding, the signals trigger the endocytic response. In this way, the viral entry is promoted and the infection is optimized. In the case of influenza virus, the receptor binding site on its HA is specific to the sialic acid receptor on the cell surface. The binding of HA to the sialic acid receptors leads to the activation of kinases, which will trigger inward curving of the plasma membrane. Tyrosine, an amino acid, was proven to be involved and crucial in the case of influenza virus, as control experiments with inhibited tyrosine showed that the influenza virus was incapable of infection (66, 67). Many questions regarding the signaling of influenza viruses are still open. For instance, are there other kinases involved in this process? How does the cell further process the signals?

2) Entering: Cells have their own defense systems, the first of which is the membrane. To overcome these barriers, viruses developed many methods, adapted to the target barrier type. The influenza virus takes advantage of an existing cell mechanism called “endocytosis”, which is a natural way of cells to absorb nutrition. Excellent reviews are available in describing such phenomena (10, 68, 69). To overcome the barriers into the cell cytoplasm, some viruses are small enough to directly penetrate through the plasma membrane; however, most of them need to take advantage of an existing cell mechanism “endocytosis”. There are two ways of endocytosis: phagocytosis and pinocytosis (70). Phagocytosis is used to engulf large particles and bacteria. For instance, the giant mimivirus take this way to enter the cell (71). Pinocytosis is used to uptake particles such as molecules and smaller viruses. Pinocytosis occurs by several different mechanisms: macropinocytosis, clathrin-mediated endocytosis, caveolin-mediated endocytosis, and clathrin- and caveolae independent pathways (72). Earlier investigations on the influenza virus way of endocytosis were based on EM, by which viruses were seen wrapped inside coated pits on the cell surface (73). Such observations provided direct evidence that the virus enters the cell by clathrin-mediated endocytosis. Later work showed that influenza virus can enter and infect cells also in the absence of clathrin-mediated endocytosis (74). Using fluorescence

microscopy, it was shown that the influenza virus can employ both clathrin-mediated and clathrin- and caveolin-independent endocytic pathways in parallel, and both pathways lead to viral fusion with similar efficiency (75). Taking the clathrin-mediated endocytosis (76) of influenza virus for example, in the initial state, clathrin and dynamin-2 can be seen accumulating quickly under the binding site of the virus. The clathrin molecules pocket the membrane inwardly in that area to engulf the virus and the dynamin-2 accumulates to the edge of the pit to scissor it off the membrane surface. The endocytosis is shown schematically in **Fig 1.1.9**.

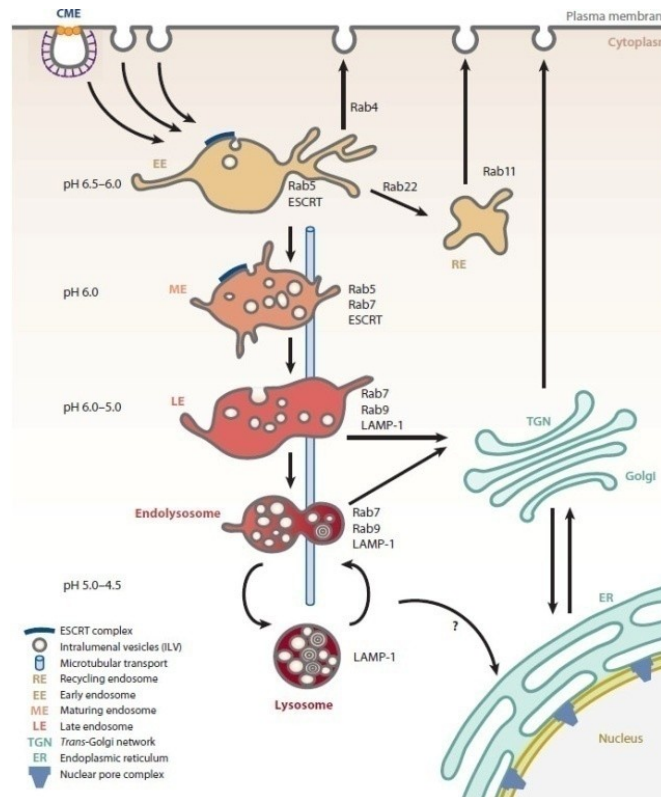


Fig 1.1.9 Schematic of influenza virus entry pathway into the cell. Clathrin-mediated endocytosis (CME) forms clathrin-coated-pits (CCPs) in which the influenza viruses are coated. The CCPs are cut off the plasma membrane and escort the virus into the early endosome (EE). The EE matures to the late endosome (LE). During the stay in endosomes, influenza viruses are subjected to a gradual acidification, which triggers the unpacking of the viral shells, and the release of the viral genome into the cell nucleus. The image is reproduced from (10).

3) Unpacking: Once the clathrin-coated-pits are detached from the cell plasma membrane, the viruses are escorted along the cytoskeleton to the early endosomes and then ferried from the cell periphery to the perinuclear area by endosomes. During the transportation process, the influenza viruses are

exposed to a decreasing pH, which enables them to “sense” their location in the cell and prepare for the unpacking. In fact, two distinct acidification steps respectively in the early endosomes (pH~5.5-6) and late endosomes (pH~5-5.5) were found to be essential for the infectivity of influenza viruses (77). A series of activities happen as early as in the early endosomes, preparing for the unpacking of the virus. At ~pH 6.5, M2 of the virus starts to open up (49), allowing for the acidification of the viral interior; at ~pH 6, the dissociation of M1 with vRNPs is initiated, preparing the vRNPs to enter the cell nucleus (56). Many structural and functional changes of the influenza viruses were observed at the post-acidification stage (pH~5). At pH~5.5, the viral HA cleave into two parts: HA1 and HA2, the fusion peptides are released, which will insert into the endosomal membrane. The HA membrane anchor parts in the viral membrane function together with the fusion peptides in the endosomal membrane, will pull the membranes together and result in membrane fusion. After the fusion process, the viral interior is exposed to the cytoplasm, enabling the release of vRNPs (73, 78, 79). The schematic of HA fusion is shown in **Fig 1.1.10**.

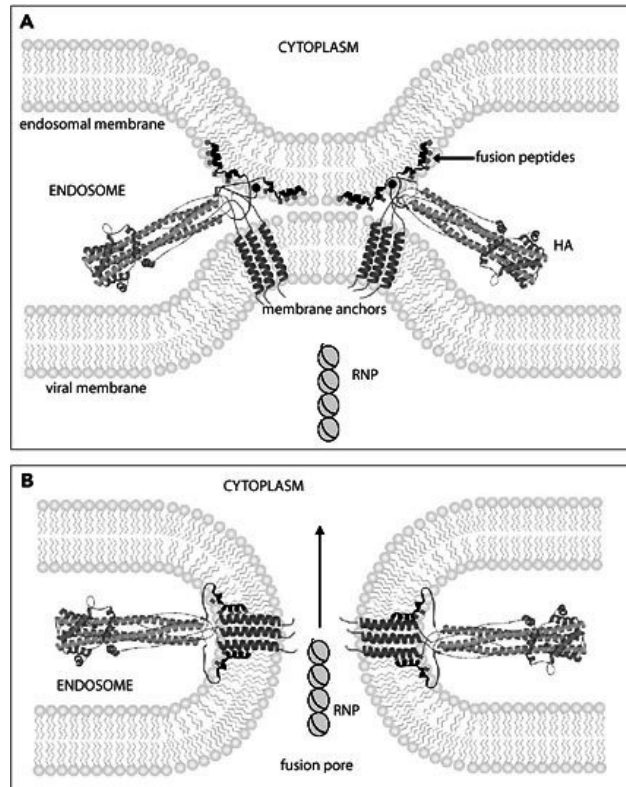


Fig 1.1.10 Schematic of influenza virus HA fusion activity. (A) At pH~5.6, the fusion peptides insert into the endosomal membrane, together with the help of anchors in the viral membrane, the peptides pull the endosomal membrane towards the viral membrane. (B) The endosomal membrane is fused with the viral membrane; the viral interior is exposed to the cytoplasm, enabling the release of vRNPs. The image is taken from (80).

4) Replication: Before describing the replication of viral RNA in the nucleus, one question still needs to be answered: how do the vRNPs find their way into the nucleus? At ~pH 5 both the M1 matrix and lipid bilayer are unpacked, the vRNPs detached from M1 and released into the cytoplasm in the perinuclear area. Comparing to the width of nuclear pore (9 nm), the import of vRNPs (width 10-20 nm) into the nucleus has to be positively regulated. In fact, the nuclear localization signals (NLS) on the NP interact with karyopherin α . Karyopherin α binds to karyopherin β (both are from the host cell), which mediates with the nuclear pore proteins and promotes the import of vRNPs into the nucleus. The process is shown in **Fig 1.1.11 A**.

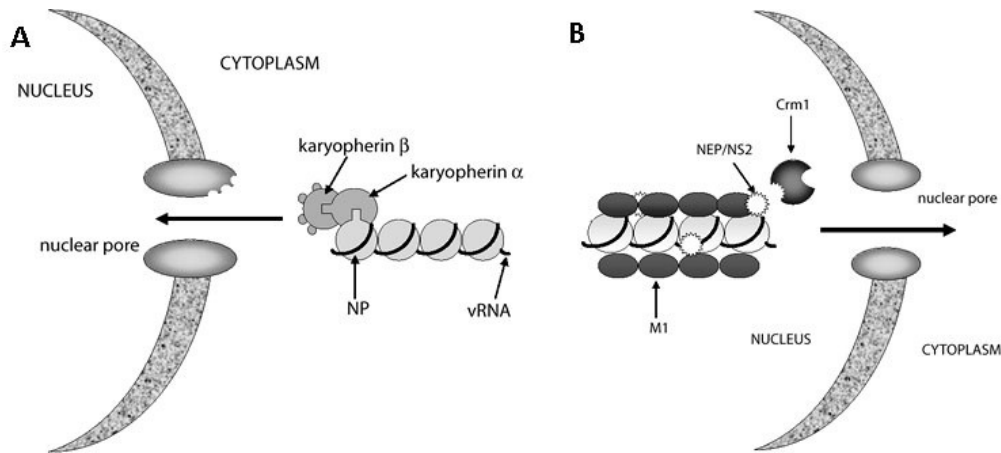


Fig 1.1.11 Diagram showing the import and export of vRNPs into and out of the host-cell nucleus. (A) The vRNP is imported into the nucleus by interacting with karyopherin β via Karyopherin α . The karyopherin β further interacts with nuclear pore proteins and promote the import. (B) The M1-bound NEP/NS2 interacts with a cellular export factor (Crm1), and exports the newly synthesized vRNP out of the nucleus. The image is taken from (80).

As mentioned before, the influenza viral RNA is negative sensed, all the genetic information needs to be converted into positive sense to be translated. Once entering the nucleus, vRNA is transcribed into viral mRNA and cRNA, both of which are positive sense. The viral cRNA is used to replicate vRNA in the nucleus; and the viral mRNA is exported out of the nucleus, being translated into viral proteins by the ribosomes. Three vRNA polymerase proteins are essential in this transcription process: PB1, PB2 and PA. The function of PB1 and PB2 are best known. The transcription must be initiated with the presence of PB2 (81); while the sequential addition of nucleotides during RNA chain elongation must be catalyzed by PB1 (82).

Some of the proteins translated by mRNA, e.g. HA and NA, are secreted through the Golgi apparatus into the plasma membrane; others are transported into the nucleus. Of the latter proteins, M1 was

found to be crucial in promoting the export of vRNPs (52), as control experiments in which the entry of M1 back into the nucleus was inhibited showed defective influenza viral infection (83). Moreover, the heat shock protein 70 was found bound to RNP at high temperature, inhibiting viral infection by blocking the binding between M1 and RNP (84). NS1 protein is employed by influenza virus as “destroyer”. Its functions include degrading cellular mRNA into nucleotides for vRNA synthesis and also inhibiting the translation of host-cell mRNAs (85). The newly synthesized vRNPs and vRNA bind together as early as in the nucleus, and are exported out of the nucleus. Nuclear export protein (NEP/NS2) and M1 play important roles during the export, which is shown in **Fig 1.1.11 B**. Upon export out of the nucleus, the bond between M1 and vRNP will inhibit the reentering of vRNPs back into the infected nucleus (52); the infected cells are exhausted and die afterwards.

5) Assembly and budding: After the virus has multiplied its components into many copies, they now have to be assembled into new viruses and released from the cell. The whole assembly and budding process includes: delivery of viral components to the cell membrane; assembly of the components; budding of the new virus; release of the new virus. Excellent reviews are available which give details of the processes (45, 57, 86).

The apical plasma membrane of polarized epithelial cells is the assembling and budding site of influenza viruses (57). Of all the components, the delivery of membrane proteins (HA, NA and M2) to the budding site is clear. After being synthesized by the ribosomes, they are transported to the Golgi-apparatus via the endoplasmic reticulum, from where they are transported to the membrane. The apical targeting signals on HA and NA were shown to be associated to lipid rafts (87), which transport the proteins to the membrane. The apical targeting signals of M2 are unclear. Cholesterol is believed to be a mediator which binds to M2 and regulates the transportation (88). The delivery of M1 and vRNP to the budding site is also still unclear. It was suggested that M1 and M1-vRNP complexes are likely to be directed to the budding site by a piggy-back interaction during the transport of HA and NA (41).

One set of influenza viral genomes contains 8 segments of different pieces of RNA, each of which is organized into a vRNP. Two models were proposed to describe the packaging of the genome into one virus: random incorporation model and selective incorporation model. The random incorporation model assumes that the incorporation of the viral genome is a random process; the success rate of the incorporation of 8 different segments is 0.24%, calculated mathematically. This model is supported by the observation that occasionally more than 8 segments are observed inside a virus (89). The second model assumes the viral genome contains a certain “recognition signal”, which enables the genome to selectively sense the type of other genomes, and direct the way of genome packaging. Obviously, the latter way is more efficient in producing infection-effective progenies. Increasing evidence is supporting the selective incorporation model (42, 90, 91). For example, high resolution electron micrographs of influenza virus showed that the RNPs of influenza A virus are organized in a discrete pattern (seven segments of different lengths surrounding a central segment), indicating the 8 segments may contain selective signals which may recognize each other and help the selective incorporation (42).

M1 plays essential roles in virus budding. Virus budding cannot happen without M1, even M1 expressed alone can form virus-like particles in cells (92, 93). Firstly, M1 is the major budding force to create curvatures on the cell membrane. Secondly, M1 was believed to be the key protein in recruiting, concentrating and assembling viral components on the assembly site. Lastly, M1 was shown to be an important determinant of the morphology of the influenza viral particles (58, 94-96); the M1 matrix plays the role of the skeleton of the virus. After budding, NA scissors the virus off the host cell and prevents self-aggregation of the newly budded viruses and their reattachment to the cells (48).

An alternative budding model has been proposed based on the lately found new function of M2. Until recently, M2 was not considered to play a significant role in budding (57), however, novel budding models of influenza virus may prove the contrary (86). It was shown that M2 is able to stabilize the budding site, possibly by enabling the polymerization of the matrix protein and the formation of filamentous virions (97). Surprisingly, instead of the NA-scissor-theory, M2 was proposed to cause membrane scission and the release of the newly formed viruses, since M2 is able to alter membrane curvature at the neck of the budding virus (98). A new model of influenza virus budding (**Fig 1.1.12**) was proposed in (86), which is partly different from the model proposed in (57).

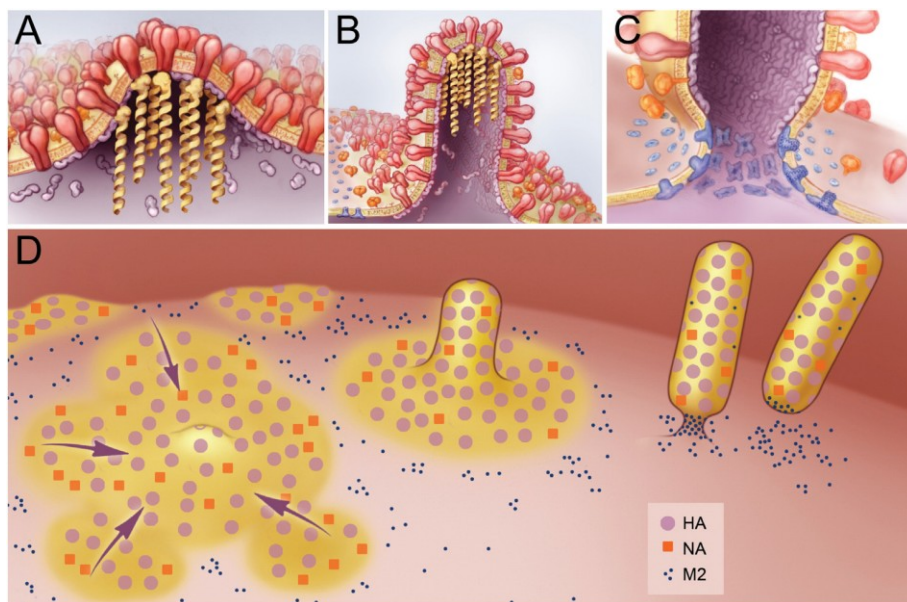


Fig 1.1.12 Most recent model of influenza virus budding. (A) Clustering of HA (red) and NA (orange) on the cell membrane initializes the virus budding. M1 (purple) serves as a docking site for the vRNPs (yellow), and also bind to the cytoplasmic tails of HA and NA. (B) The polymerization of M1 causes the elongation of the budding virion, resulting in a polarized localization of the vRNPs. M2 (blue) interacts with M1, and is recruited to the periphery of the budding virus. (C) M2 alters the membrane curvature at the neck of the budding virus, and scissors the virus off the host cell. (D) Overview of the budding

process, showing lipid rafts (yellow) containing HA and NA; the formation of a filamentous virion; and membrane scissored off by M2 clustered at the neck of the budding virus. The image is taken from (86).

Not only the protection provided by the influenza viral shell is interesting, more details of the viral activities in the infection process need to be revealed. As was mentioned above, the viral unpacking at fusion pH is well studied; however, the preparation steps for the viral M1 and lipid envelope unpacking in the premature acidic pH (pH~ 5.5-6) are still unclear. It was suggested that, in the vicinity of pH 6 (pH~6-6.5), the M2 ion channel protein of the virus started to open up (49), preparing for the acidification of the viral interior. At pH~6, the M1 capsids become weaker. As an adaptor between the vRNPs and the viral membrane as well as between the vRNP dissociation of M1 with vRNPs, the weakening of M1 will initialize the dissociation of these interactions, preparing the vRNPs to enter the cell nucleus (56). The early endosomes further mature into late endosomes, in which the environment is more acidic (~pH 5-6). The thickness of the M1 layer (~3 nm) makes the direct observation of the M1 matrix very difficult on EM. For example, it was suggested that M1 were intact and serve as a foundation for the HA fusion activities at pH 5.5 (99), however this is questioned by our observation. Even if M1 can be clearly resolved, the visual impression itself is not enough to show the difference of mutual interactions of the M1 dimers at different pH.

AFM provided us a way to fill this gap by measuring the elasticity of the complex. Any weakening of the M1 dimer-dimer interactions may be reflected by a decrease in stiffness. In this work, we used AFM to study the mechanics of influenza A/X-31 virus at different pHs, which mimics the continuous acidification during the endosomal pathway of the virus into the cell.

1.2. Small unilamellar vesicles

1.2.1. Lipid bilayers and liposomes

Definition

Lipid bilayers are found in many organisms from cells to viruses. They form remarkably thin envelopes (~5 nm), often referred to as the membrane. The lipid bilayer serves as a natural barrier, which isolates the interior from the outside environment, yet it is selectively permeable to certain substances. Such a structure provides the ideal protection to many organisms, such as cells, bacteria, viruses as well as cell organelles. Natural lipid bilayers are composed of 2 leaflets of phospholipids, which orientates itself in such a way that its hydrophobic tails point to the inside of the leaflets, and its hydrophilic heads are exposed to the outside (**Fig 1.2.1**). The lipid bilayer is a dynamic system, the phospholipids are constantly moving: they frequently switch positions with their neighbors and move laterally over the bilayer surfaces. Such dynamic behavior contributes to the elasticity and permeability to the biological membranes, and enables the membranes to heal themselves when small fractures appear.

Lipid bilayers are mostly formed into closed envelopes called a vesicle, which size ranges from 20 nm to 10 μm . If no vesicles are present in its interior, the vesicle is called unilamellar; otherwise multilamellar. The diameter of a small unilamellar vesicle (SUV) is below 100 nm, larger ones are called giant unilamellar vesicle (GUV). Vesicles have a wide range of applications. Natural ones are found as cargo transporters (e.g. endosomes, synaptic vesicles). They can fuse with other membranes and can dock various surface proteins. For my work SUVs of different composition formed a simplified model system that helped us to better understand the mechanics of the influenza virus.

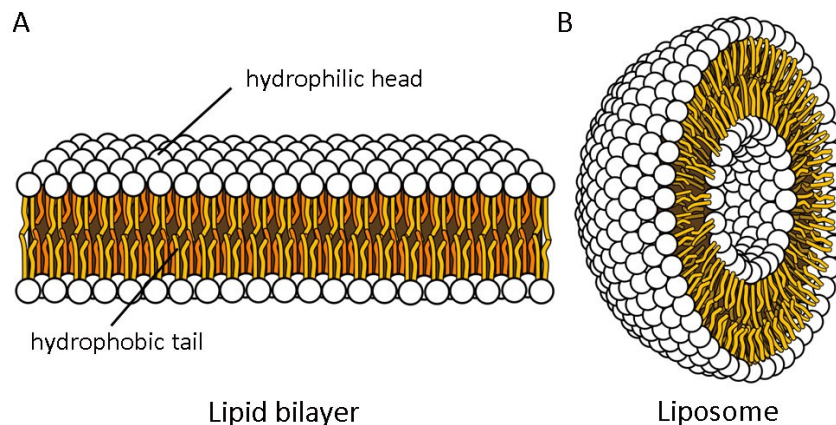


Fig 1.2.1 Structure of (A) lipid bilayer and (B) a liposome. The hydrophobic tail and hydrophilic head are marked. This image is reproduced from Wikipedia.

Liposomes, application of liposomes

If made artificially, the SUV is usually called liposome. Due to the aforementioned properties, applications of liposomes are widely found in pharmaceutical and cosmetic industry and science (100). Liposomes can be applied for drug delivery and targeting, aiming at enhancing the effective delivery rate of the drug. Our body protects itself with a complex defense system. It forms thrombus and coats larger invading objects with biomacromolecules; smaller invading objects such as microbes and bacteria can be “eaten up” by the cells of the immune system. Such defensive responses of the immune system have triggered large efforts in the development of biocompatible and non-recognizable surfaces. For example, when injecting drug-containing liposomes into the blood stream, a major problem is the consumption of the liposomes by the reticuloendothelial system (RES). One way to achieve longer circulation time is by coating the liposomes with a suitable polymer. The liposomes modified in this way are called stealth liposomes (101). In scientific research, the liposome is studied as a model of biological membranes. Research on liposomes focuses on the phase transition, permeability, fusion and protein docking. Our work focuses on the mechanics of single liposomes.

1.2.2. Mechanics of lipid bilayers

Definition of the mechanics of a lipid bilayer

Systematic studies of lipid bilayer mechanics were initiated in the 1970s by *W. Helfrich* (theoretical) and *E. Evans* (experimental), aiming at decomposing the bilayer deformation and extracting bilayer elastic parameters (102-104). In their early work, the deformation of a surface was defined with 3 independent elements: 1) area dilation or condensation, 2) in-plane extension at constant area, and 3) bending without change in rectangular shape as shown in **Fig 1.2.2**.

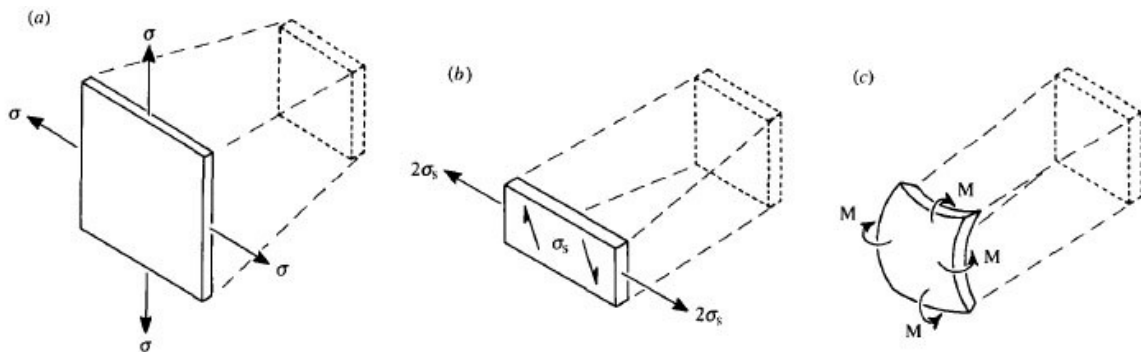


Fig 1.2.2 Illustration of surface deformation decomposed into 3 independent elements. (a) Area dilatation, when the number of molecules per unit surface area decreases as the surface area increases,

(b) In-plane extension without surface area change, (c) Bending without change in planar shape. The three independent shape changes compose of any deformation of the surface. The image is taken from (105).

At constant temperature, the first element can be quantified by a parameter called **area compressibility** K_a . It describes the ratio of the fractional change in surface area at constant temperature and tension. The second element can be quantified by a parameter called **surface shear rigidity** μ . The third element can be quantified by a parameter called **bending rigidity** K_b . According to (105), the surface shear rigidity for liquid membranes equals to 0, because the phospholipids can freely diffuse through the membrane. For a three-dimensional isotropic material, the bending rigidity K_b is:

$$K_b = \frac{Et^3}{\alpha(1 - \nu^2)} \quad (1.2.1)$$

where t is the thickness of the bilayer, E is Young's modulus in Pa and ν is the Poisson's ratio (103). For a material that consists of two leaflets that can slide without friction, the factor α is set to be 48, for limited friction 24 and for unlimited friction 12. We set α as 24.

For simple elastic models, when the stress is assumed to be distributed across the bilayer, K_b can be related to K_a by (105):

$$\frac{K_b}{K_a} = \frac{t^2}{\alpha}, \quad K_a = \frac{Et}{1 - \nu^2} \quad (1.2.2)$$

ν , the Poisson's ratio, is set to be 0.5 (106), therefore:

$$K_b = \frac{Et^3}{18}, \quad K_a = \frac{4Et}{3}, \quad \frac{K_b}{K_a} = \frac{t^2}{24} \quad (1.2.3)$$

The ratio K_b/K_a has been found to be almost constant with values between 3 and $5 \cdot 10^{-19} \text{ m}^2$ (105). Assuming $K_b/K_a = 4 \cdot 10^{-19} \text{ m}^2$, one has $t = 3.1 \cdot 10^{-9} \text{ m}$. Such a reduced thickness (with respect to the real thickness of lipid bilayers $\sim 5 \cdot 10^{-9} \text{ m}$) can be understood as the effective thickness of the lipid bilayer. The two leaflets are replaced by a thinner single sheet to maintain the same bending rigidity. This approximation is made in order to meet the criteria of **equation (1.2.1)**, which assumes the lipid bilayer as a three-dimensional isotropic material. This assumption allows us to model the lipid bilayer as an isotropic material with finite element methods.

Determination methods of the mechanics of lipid bilayers

The mechanical characterization of lipid bilayers and SUVs is important. For example, SUV are known for being less stable than GUVs and planar bilayers (107) as is reflected by their lower phase transition temperature and other physical parameters. However, ideal liposome-based containers should be stable and have long lifetime in the human body (108). If the mechanical properties of SUVs can be quantified, stabilization schemes can be applied to achieve these goals. Also for this reason the choice of a lipid bilayer as a component of the genome-protecting envelope of viruses such as influenza is striking: Influenza, a 100 nm diameter enveloped virus, was shown to be able to persist for days in rather harsh conditions (31), but unexpectedly (109) its lipid membrane is thought to be rather fluid and soft over a large range of temperatures (110). It therefore has to be determined whether the lipid envelope of the flu virus on its own can act as a barrier that is as effective as a protein capsid, or if it requires the participation of viral protein to fulfill its protective role. Studying the stability of SUV and related organelles/viruses is of great interest for both fundamental and applied purposes, as this may lead to a better understanding of biological problems such as the assembly and stability of enveloped viruses, as well as new solutions to stabilize liposomes as drug carriers. Unfortunately, almost no quantitative information on the mechanical properties of small liposomes exists so far, contrary to GUVs, which have been studied for 30 years (111).

Studies of vesicle mechanics focus on the quantification of the elasticity of the bilayer and correlating this to the biological role of the vesicle. Although the mechanics can be measured with multiple techniques, the principle is similar: to quantify the passive or active deformation of the object into the two key quantities, area compressibility K_a and bending rigidity K_b . The first active deformation technique applied micropipette aspiration to osmotically swollen red blood cells. Small reversible displacements of the cell projection in the pipette in response to the applied pressure was recorded and converted to area compressibility (102, 103). Other active deformation techniques used an electric field (112), magnetic field (113), or optical tweezers (114) to deform the object. The first passive deformation technique, observed by phase contrast microscopy, measured the thermal fluctuations of egg lecithin bilayers caused by Brownian motion, and calculated the elasticity from the fluctuations. Many further measurements were based on this technique (115-117). Because these techniques use conventional microscope methods, the smallest size of the samples was limited to $\sim 5 \mu\text{m}$.

SUV are by definition liposome with a size goes up to 100 nm. Those highly curved, closed lipid bilayers are too small to be measurable by optical microscopy or micropipettes. AFM, a nanometer resolution microscopic method, images the object by direct contacting it with a very sharp tip (diameter ~ 5 -100 nm) and is also capable of measuring the mechanical properties of the sample by deforming it. In the early measurements, the mechanical properties of liposomes made from Egg PC were directly measured by AFM and were compared to that obtained by other methods. It was also shown that the liposomes can be punctured by the tip, which is reflected by the kinks shown on the force curve (118). AFM is also applied to study the pore-spanning lipid bilayers (119), which is made from GUVs and can be used as a model to study the mechanical properties of cell membranes (120). In this thesis, we have set up a precise, AFM-based force spectroscopy method to quantitatively study the mechanical properties of

SUVs. The principle is shown by a simple schematic drawing in **Fig 1.2.3**. Details about the method are available in section 1.3.

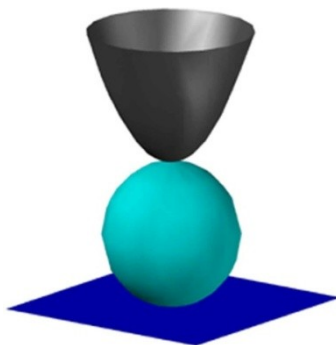


Fig 1.2.3 Schematic representation of indenting a liposome with an AFM tip.

1.2.3. Parameters that influence the mechanics of lipid bilayer

Cholesterol and proteins

Cholesterol stiffens the membrane. Cholesterol is present in large amounts in biological membranes. For example, the influenza viral lipid envelope contains 44% cholesterol (121), which was found to be essential for the fusion of influenza virus (122). Cholesterol increases the membrane strength and decreases permeability by inserting into the membrane and interacting with the phospholipid fatty acid chains (**Fig 1.2.4 A**). Membranes of myelin forming cells, another sample we have studied, are rich in cholesterol (~38%), which is implicated to increase the insulation for a more efficient conduction of electrical impulses. In this thesis, liposomes made from DMPC with or without cholesterol were tested. We found that, the bending rigidity of DMPC: cholesterol (1:1 mol/mol) liposomes is over three times higher as compared to that of the pure DMPC liposomes.

All biological membranes contain proteins that are embedded in the lipid bilayer, the quantity and composition varies with depending on the type of membrane. Besides contributing to the functions of the membrane, they also influence the mechanics. The membrane embedded proteins soften the membrane. Many proteins were found to form pores in the membrane that increase its permeability, the pore diameter vary from 1 to 200 nm (123). For example, Melittin is a simple peptide consisting of 26 amino acids. It was first found in bee venom, exhibiting functions as anti-bacterial and membrane pore formation (124), which increases the permeability for ions (**Fig 1.2.4 B**). The membrane lyses, if excessive amount of melittin is present (125). To verify the softening effect of melittin, we tested DMPC liposomes with 0.5% melittin with AFM. However, no liposomes were detectable. Given the fact that the DMPC liposome is the softest sample that we could observe by AFM, the DMPC+melittin liposomes may have been beyond our technical capabilities of the AFM method.

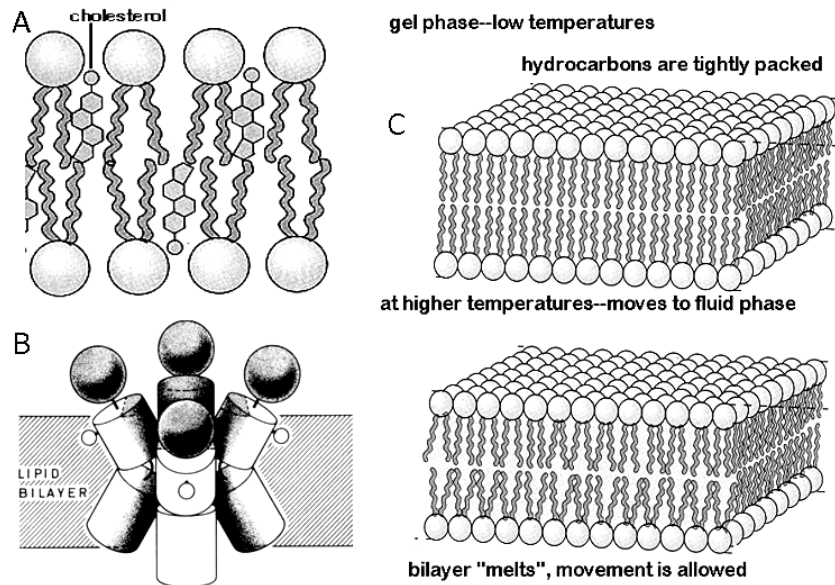


Fig 1.2.4 Schematic drawing showing the influencing factors to the mechanics of the membrane. (A) The cholesterol inserts itself in parallel with the phospholipids, strengthening the membrane by interaction with the phospholipid fatty acid chains. (B) Schematic of tetrameric melittin in membranes. The COOH-terminal segments of melittin are represented by spheres; the membrane-bound α -helical segments are represented by cylinders. Melittin forms a bilayer-spanning polar pore. (C) Temperature induced phase transition of membrane. In the gel phase (low temperature), the tails of the phospholipid are well organized. The membrane is tightly packed. In liquid phase (higher temperature), the bilayer seems to “melt”, the membrane shows more fluidity. (A) and (C) are taken from (126), (B) is taken from (127).

Temperature

The dynamic motion of phospholipids in the bilayer is affected by temperature. At higher temperature, the acyl chains of the phospholipid change from a *trans* to *gauche* conformation, which shorten the tail length, and enlarge the occupation volume of a single phospholipid (**Fig 1.2.4 C**). Lipid molecules in such a “melted” state will be less affected by the van der Waals interactions between adjacent lipid molecules and therefore have more degrees of freedom. In fact, similar to crystals, all lipids exhibit such temperature dependent phase transitions. The characteristic temperature which separates the lipid states into liquid and solid (or gel) phase is called phase transition temperature (T_p). T_p can be affected by the chain length and saturation of a phospholipid. Usually pure lipids with longer and saturated chains have higher T_p , so do the lipid mixtures with higher proportion of longer and saturated chain. In this thesis, the temperature effect on the mechanics of DOPC liposomes was measured. At 13 °C, no obvious stiffening of the DOPC ($T_p = -20^\circ\text{C}$) was observed.

Lipid composition

Natural lipid membranes are composed of multiple phospholipids. Such mixtures will alter the physical properties of the membrane, such as mechanics, phase transition temperature and permeability. Firstly, bilayers composed of longer-tail-lipids will be thicker and exhibit larger K_b , according to **equation (1.2.1)**. Secondly, with mixtures of different lipids, the organization of the lipids can be arranged so that they fit to the curvature. In this way, the lipids in both leaflets of the curved bilayers can be densely distributed. The mechanisms which explains how the lipid bilayer mechanics is affected by the lipid composition is shown in **Fig 1.2.5**.

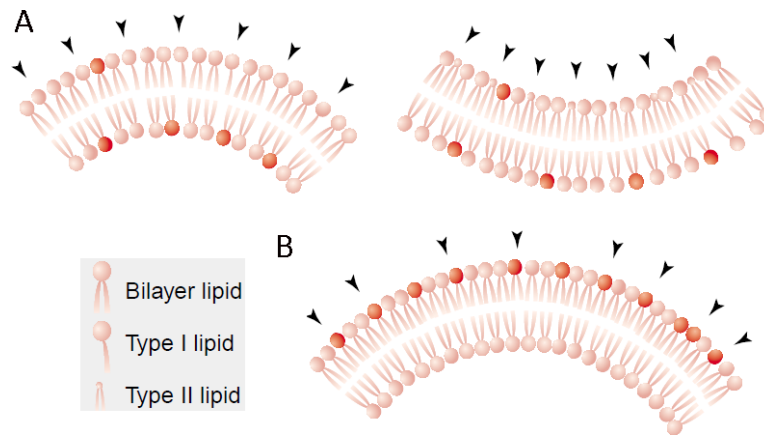


Fig 1.2.5 (A) Different lipid types affect lipid bilayer mechanics. The arrows point to the lipids which have closer tails (left) and smaller hydrophilic heads (right). (B) The differentiation of the population density of outer and inner leaflets of the bilayer can also cause bending. The arrows point to the extra lipids on the outer surface of the bilayer. Inset: type 1 lipid: closer tails; type 2 lipid: smaller heads. Some lipids are colored in red to mark the transferring of lipids between the bilayer leaflets. The image is reproduced from (128).

Curvature

Because the radius of the liposomes (~ 50 nm) we studied is close to the lipid bilayer thickness (~ 5 nm), the lipid bilayer is highly curved. At this curvature, the two leaflets of the bilayers will exhibit different spatial densities. The lipid heads on the outer leaflet will be spaced further apart than the ones on the inner leaflet; while the lipid tails on the outer leaflet will be spaced more densely than the ones on the inner leaflet (**Fig 1.2.5 B**). The loose organization of the phospholipid heads on the exterior surface will increase the risk of exposing the hydrophobic tails to water, and thus endanger the liposome structure. In fact, it is known that liposomes are less stable than GUVs and planar bilayers (107). It is expected that the bending rigidity is not constant but varies as a function of the curvature. I investigated this curvature dependency by performing measurements on liposomes with radii from 15-100 nm.

1.3. Atomic force microscopy

1.3.1. General introduction

Principle

Since invented in 1986 by *G. Binnig* et al. (129), AFM has been extensively developed further and applied to decode the nanoworld in biological, material, chemical sciences and many industrial fields. The principle of AFM, as is shown in **Fig 1.3.1 B**, is simple: it acquires information of an object by touching it with a sharp tip which is attached to a flexible cantilever. A laser beam projected on the back of the cantilever is reflected onto the detector, which records the bending of the cantilever. The laser signal is translated into electrical signal which can be used to trace a sample and to reconstruct a topographical image. This is just like one touches an object with his fingers to gain impressions about its shape or stiffness. Large amounts of knowledge about AFM techniques and applications are available, however, only the parts relevant to this thesis will be presented here.

AFM compared to EM

Both AFM and EM are important tools for structural biology studies. In general, AFM is used to obtain information of the surface structure and also the mechanical properties of the samples. EM provides better resolution and can be used to obtain information of the interior structure of the sample.

Compared to EM, AFM has many advantages. 1) AFM provides 3 dimensional images, while raw EM images only provide 2 dimensional or 2 dimensional projection information of the sample. 2) EM samples need to be specially treated before imaging (such as metal/carbon coatings or freezing), such treatments are usually time-consuming and may induce artifacts to the sample. Also the treatment will fix the samples, therefore prohibited observation of the sample dynamics. However, AFM samples require only little treatment, and their dynamics can be preserved. 3) Due to the high amount of noises in the EM images, usually a large numbers of images are required to obtain a high resolution image, which is not necessary for AFM images. 4) EM needs to be operated in an expensive vacuum environment, while most AFM work very well in air and liquid conditions, which allows the study of biological samples in their physiological conditions. And 5) by AFM, the mechanical measurements are possible.

In contrary to AFM, it usually takes a much longer time to process the raw EM images than to obtain them. A three-dimensional EM image, namely the tomogram, can be reconstructed by electron tomography, which takes a series of projection images at different tilted angles and combining them computationally. With this technique, three-dimensional images of HSV were obtained, revealing the structural arrangement of nucleocapsid and tegument, as well as providing information about the length and spacing of the glycoprotein spike proteins (130). Although the sample has to be fixed prior to imaging, the different stages of the dynamics process can still be captured by sample preparation. For example, by fixing ribosome samples 0, 1 min, 2 min, 5 min, and 20 min after adding the tRNA for cryo-

EM imaging, the ribosome ratcheting and tRNA movement were recorded as time-resolved sequences (131).

Noise minimization

AFM is highly sensitive to mechanical noise. The most important noise sources are acoustic noise, vibrational noise and temperature noise. Nearby loud speaking, walking, building vibration can all lead to severe artifacts in both images and mechanical data. If exposed to temperature changes of $>1^{\circ}\text{C}$, large thermal drift may also appear, which leads to image artifacts and errors in the mechanical measurements. Those errors may be minimized by 1) placing the AFM on an active noise cancellation table or by placing the AFM on a surface that is suspended to the ceiling by bungee cords to reduce the vibrations; 2) keeping the instrument in a soundproof hood to avoid acoustic noise; 3) installing the AFM in the basement to minimize building noise; and 4) use air-conditioning to minimize variations in temperature. The AFM used for this thesis is placed on an active vibration isolator (with a separated power supply to reduce heat generation); the setup is kept in an acoustic noise cancelling hood; an air-conditioning is installed in the hood to keep the temperature constant within 0.1°C ; the aforementioned setup is placed on a heavy metal rack to further avoid the vibration; all cables connected to the device are clamped between two heavy metal blocks to cancel possible vibrational noise that can be transmitted via the cables. A realistic photo of our setup is shown in **Fig 1.3.1 A**.

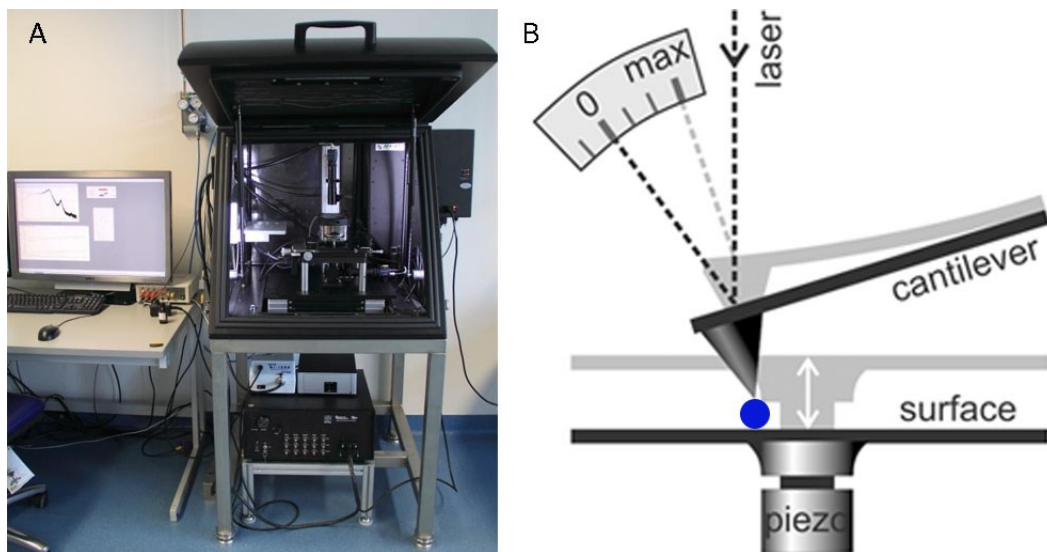


Fig 1.3.1 (A) The *Asylum Research* MFP-3D AFM is extensively used in our lab. The AFM is placed on a vibration control table in an acoustic hood, which is placed on a heavy metal rack. The AFM is controlled by the electronics that are placed under the hood and a computer. To avoid possible influence of temperature variance, an air temperature controller conditional is installed on the right side of the

hood. (B) Schematic showing the principle of AFM. A laser beam projected on the back of the cantilever is reflected to the detector. Any movement of the cantilever will be recorded by the change of laser signal in the detector. Piezos installed in the stage (or AFM head) enable sample movement in the (x,y,z) direction.

1.3.2. AFM cantilever calibration

The cantilever-associated tip is the “finger” of an AFM. Usually the tip sharpness and cantilever stiffness are reflected in the image quality of the sample. Optimizing both parameters does not necessarily mean choosing a sharper tip and a stiffer cantilever, they must be suitable to the corresponding samples. Meanwhile, the physical properties of the cantilever and the tip need to be well characterized so that the artifacts can be minimized.

In most cases, the physical properties of the AFM cantilever need to be accurately obtained. To obtain accurate results each cantilever should be individually calibrated before an experiment, rather than merely use the parameters given by the manufacturer. Of all the properties, the cantilever resonance frequency and spring constant are the most important for tapping mode imaging and mechanical measurements.

If imaging is performed in tapping mode, the cantilever needs to be vibrated at a constant frequency and amplitude. If vibrated at resonance frequency, the cantilever achieves maximum amplitude at minimal excitation. To obtain the resonance frequency, the cantilever is vibrated by a piezoelectric shaker with a continuously increasing frequency, meanwhile the vibration amplitude is obtained via the photodetector signal from the lock-in amplifier. This process is often referred to as the tuning of the cantilever. Plotting the amplitude against frequency, several peaks are visible (**Fig 1.3.2**), which consist of the real resonance frequencies of the cantilever but also those of other parts in the AFM head (132). The peak which is closest to the first peak of the thermal noise power spectral density (**Fig 1.3.5**), or the highest peak will usually be chosen. The value will be used by the AFM software, so that when imaging in tapping mode the cantilever will be vibrated at this frequency. It is worth mentioning that, if small temperature changes occur, the peaks are likely to shift, therefore it is recommended to retune the cantilever on an hourly basis and each time after changing the sample.

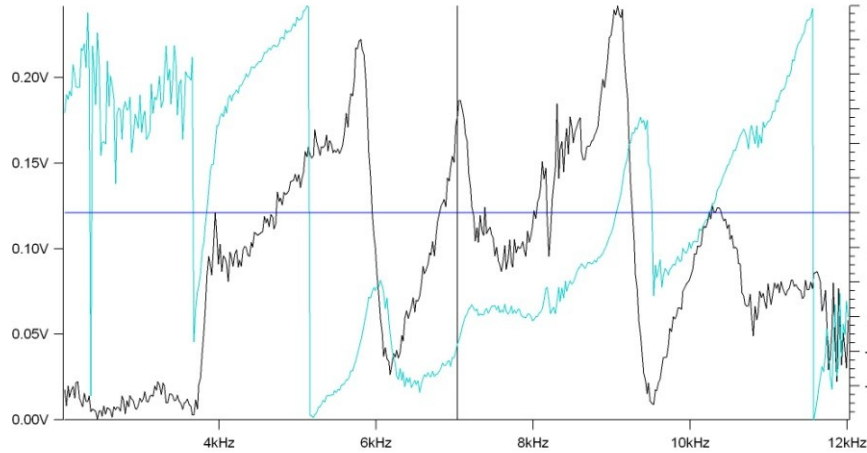


Fig 1.3.2 Tuning graph of a cantilever. A piezoelectric shaker which is associated to the cantilever vibrates it with frequencies increased from 2 to 12 kHz. The amplitude (recorded via the photodetector signal) is plotted against the frequency. (Black) Multiple major peaks are visible on the plot, known as *the forest of peaks*. (Green) The phase shift between the drive and detector signal is shown. (The image is obtained by a MFP-3D AFM with an Olympus bio-lever BL-RC150VB.)

The characterization of cantilever spring constant is essential for mechanical measurements. The cantilever and sample can be seen as two springs in series **Fig 1.3.3**:

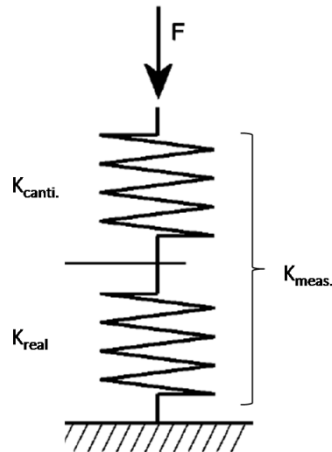


Fig 1.3.3 Schematic drawing shows the relation of cantilever, sample and measured spring constants.

The directly measured stiffness ($k_{meas.}$), the real stiffness of the sample (k_{real}) and the spring constant of the cantilever ($k_{canti.}$) follow the equation:

$$\frac{1}{k_{meas.}} = \frac{1}{k_{canti.}} + \frac{1}{k_{real}} \quad (1.3.1)$$

To obtain k_{real} , one needs to subtract $k_{canti.}$ from $k_{meas.}$. There are several methods to obtain $k_{canti.}$ (133), only the thermal noise fitting method will be introduced here, since it is well accepted and used by us.

Intuitively, the elasticity of a rectangular cantilever shall be dependent on its geometry and material. Indeed, the spring constant can be written as:

$$k = \frac{Ewt^3}{4L^3} \quad (1.3.2)$$

where E is the Young's modulus of the cantilever material; w, t and L are the width, thickness and length of the cantilever.

The equation (1.3.2) is called cantilever beam theory. Although this method is simple and straightforward, it is usually difficult to measure the geometric parameters precisely. The thickness of the cantilever is especially difficult to determine, since the cantilevers are coated with a reflective gold layer.

A more precise and time-saving way to determine $k_{canti.}$ is by fitting the thermal noise curve of the cantilever. When the cantilever is kept in equilibrium in the imaging media, the media particles (liquid or air molecules) bounce onto the cantilever because of the Brownian motion. The resulting bending fluctuations of the cantilever are recorded by the photodetector in Volts over time. The signal is then Fourier-transformed to obtain the power spectral density (PSD, unit V^2/Hz). The PSD recorded on the detector can be translated to the PSD of the cantilever (m^2/Hz) by:

$$P_{CL} = P_V * \frac{1}{S^2} * \frac{1}{\cos^2\alpha} * \chi^2 \quad (1.3.3)$$

where P_{CL} is the PSD of the cantilever; P_V is the PSD recorded via the detector; S is the sensitivity of the cantilever bending detection (nm/V), which can be measured by performing a force distance curve on empty hard surface (**Fig 1.3.4**); α is the angle between the cantilever and the surface (usually 10-15 degree); χ is a factor which is related to the size and position of the laser spot that is reflected on the back of the cantilever (usually taken as constant 1.09, according to (134)).

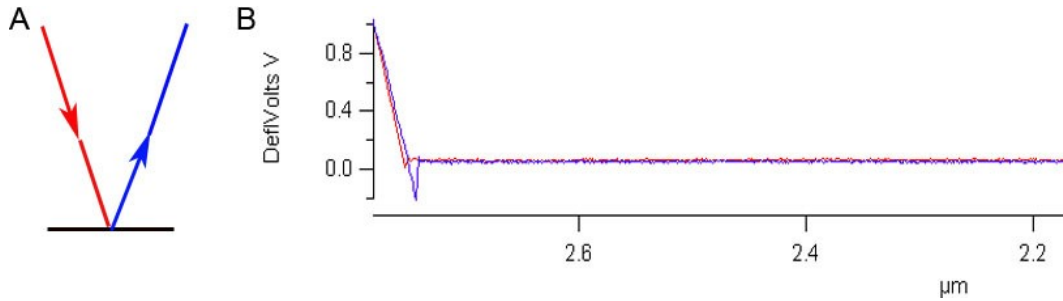


Fig 1.3.4 Typical force-distance curve obtained by performing a single indentation of the cantilever on the empty hard surface. (A) The red curve represents for the trace, which is obtained by pushing the cantilever towards the surface; the blue curve represents for the retrace, which is obtained by pulling the cantilever away from the surface. (B) Deflection of the cantilever (recorded in Volts) vs. relative distance of the cantilever tip to the surface. Similarly, before contacting the surface, the deflection remains zero. When the cantilever gets in contact with the surface, the deflection rapidly increases. The slope of the curve (V/m) gives the sensitivity of the detected system.

According to equipartition theorem, the energy of a thermally equilibrated object is equally distributed over all its possible forms. In the specific case of an AFM cantilever (which can be simplified as a spring) in thermal equilibrium, its potential energy equals to its kinetic energy. Together, both forms of the energy compose of the thermal energy:

$$H_{pot.} = \frac{k \cdot \langle x^2 \rangle}{2}, \quad H_{kin.} = \frac{mv^2}{2}, \quad H_{pot.} = H_{kin.} = \frac{k_B \cdot T}{2} \quad (1.3.4)$$

where k_B is the Boltzmann-constant, T is the temperature of the thermal equilibrium in Kelvin, k is the spring constant of the spring and x is the average fluctuation of the oscillator, m is the mass of the oscillator, and v is the speed of the oscillator.

To be able to obtain $\langle x^2 \rangle$, the cantilever is theoretically simulated as a simple harmonic oscillator (SHO). The spring constant of the cantilever can be written as a function of x (dependent on frequency) (133):

$$k = \frac{2}{\pi} * \frac{k_B T Q}{x^2(v_r)} * \frac{\Delta v}{v_r} \quad (1.3.5)$$

where v is the frequency, v_r is the resonance frequency and Q is the quality factor.

The resulting function to fit to equation (1.3.3) is:

$$\langle x^2(\nu) \rangle = \frac{A}{\nu} + B + \frac{\langle x^2(\nu_r) \rangle}{Q^2} * \frac{1}{(1 - (\frac{\nu}{\nu_r})^2)^2 + (\frac{\nu}{\nu_r * Q})^2}$$

(1.3.6)

where ν is the frequency; ν_r is the resonance frequency; $\langle x^2(\nu) \rangle$ is the frequency dependent coordinate of the oscillator, which is fitted to the power spectral of the cantilever P_{CL} ; Q is the quality factor; A and B describe the pink noise (frequency dependent) and white noise (frequency independent).

Fitting equation (1.3.6) to equation (1.3.3) by free parameters A , B , Q , ν_r and $\langle x^2(\nu_r) \rangle$, one is able to calculate the spring constant of the cantilever.

An example of SHO fitting to the PSD of the thermal noise is shown in **Fig 1.3.5**:

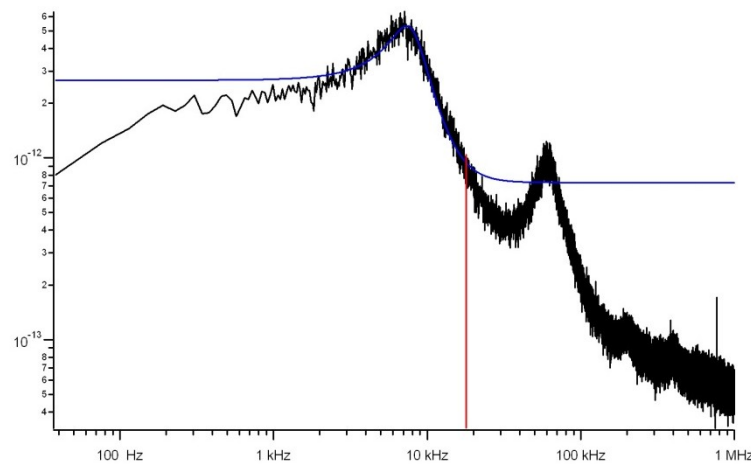


Fig 1.3.5 (Black) Thermal noise PSD of an Olympus bio-lever BL-RC150VB. (Blue) The PSD is fitted by equation (1.3.6). Both x and y axis have a logarithmic scale. The other peaks are the second, third...harmonic frequencies of the cantilever.

1.3.3. Application of the AFM: imaging

AFM is mostly applied for 2 purposes: imaging and mechanical measurements. The imaging resolution of AFM is mainly dependent on the tip sharpness, scanning mode and sample stiffness. If all ideal, details of down to a few nanometers can be resolved in liquids (135-137).

Substrate and sample preparation

One of the advantages of AFM is its convenient sample preparation, although this does not mean no pre-treatment at all. For large solid samples, e.g. metal or plastic, the process may be easier. They need to be shaped to be suitable to the sample stage, and properly cleaned to avoid artifacts. However, the preparation of biological samples takes more efforts. Firstly, the sample has to be well purified and diluted to proper concentration to avoid aggregation or exposing the tip to the risk of contamination as a result of crowded background. Secondly, the sample needs to be properly attached to a clean substrate.

Before the experiment, the sample needs to be fixed on a substrate to avoid displacement during scanning. The substrate itself needs to be flat and clean, otherwise any roughness or dirt may be mistakenly treated as the sample. Materials that exhibit extraordinary flatness are commonly used in AFM substrates, such as mica and highly ordered pyrolytic graphite (HOPG). Microscope cover slides are also a good option, since they are much less expensive and easier to handle than mica or HOPG, and are only a little rougher (~2-5 nm compared to 1 nm for mica or HOPG). Before adding the sample, they need to be cleaned and coated with sample-attractive molecules, usually positive charged. The amount and type of molecules need to be such that the charge is strong enough to fix the sample; however it should not be too strong that it deforms the sample or induces attraction to the tip. Detailed information on surface and sample preparation is available in the materials and methods section.

Imaging modes

Contact mode and tapping mode are the most common scanning modes of AFM. Contact mode is usually applied to hard and solid samples, such as metal and crystals, or even proteins (138). In contact mode, the tip is kept in touch with the sample, the cantilever deflection is kept constant. In this mode, the tip exerts inevitable lateral forces to the sample, as it scratches over the surface. Biological samples are usually easily deformable. If imaged in contact mode, the lateral force may displace, or even worse, damage the biological sample and leads to artifacts.

Tapping mode is most often applied for soft samples. In tapping mode, the cantilever is oscillated around its resonance frequency over the target area. When the tip gets in contact with an object, the oscillation is affected, reducing the oscillation amplitude and changing the phase (**Fig 1.3.6**). Such changes are used in a feedback loop to keep the oscillation amplitude and with that the tip-sample interaction constant. The tip-sample interaction is intermittent, thus causes less artifacts to the image and sample. In this thesis, tapping mode was applied to all samples studied by AFM.

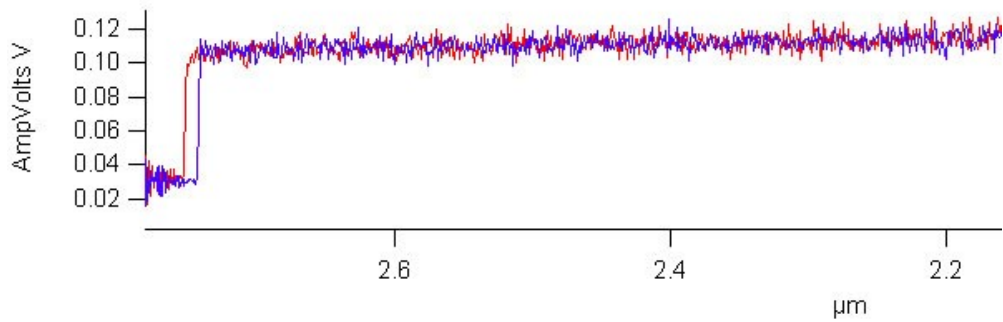


Fig 1.3.6 Amplitude (recorded as the signal variance on the photodetector in Volts) vs. relative distance of the cantilever tip to the surface. The cantilever is vibrated with a fixed frequency and approached to the surface. When the cantilever gets in contact with the surface, the amplitude rapidly decreases to almost zero.

1.3.4. Application of the AFM: Mechanics

Pulling or pushing, the mechanical measurements

As mentioned in section 1.1.1, AFM is not only capable of imaging, but can also be used to manipulate samples. Taking advantage of the physical contact between tip and sample, AFM is increasingly applied to obtain mechanical properties of samples at the nanometer scale. A good example was shown in (21), which cut, rotate and bent TMV virus on a graphite surface to manipulate and obtain the mechanical properties of the virus. The mechanical properties, often stiffness or Young's modulus, are correlated to the behavior of such organisms at the different stages of their life cycle, as well as to the way how they form and protect themselves. The principle is to deform the sample at a specified force with the AFM cantilever and record the magnitude of deformation. There are different ways of deformation, the most common one is the indentation of the sample with the AFM tip (26, 30). This method is straight forward and usually requires no tip modification. Novel methods were developed, in which the tip was modified by coating it with molecules. Such modifications enable the tip to be attractive to the objects. The stretching technique is popular in molecular studies: for example, titin proteins could be unfolded in steps when stretched by AFM tips (139); in another experiment, the AFM cantilever was used as a "crane" by attaching DNA oligomers to the tip. Such devices can be employed to transfer nanosized objects precisely to the target position (140). The aforementioned techniques focus on probing the sample vertically, either by pulling or indenting. Cantilevers can also be operated laterally. For example, focused ion beam was applied to etch cantilevers with hooks, which were capable of pulling fibroblast cells with forces of up to hundreds Newton (141).

Force curves

The most fundamental outputs of measurements are the force curves. When the tip interacts with the sample, the detector will record a change of the laser reflection (in Volts). After performing a force curve on a hard surface (**Fig 1.3.4**), the detector sensitivity can be determined (provided the z piezo is calibrated). Thus the cantilever signal can be converted to meter (m). After cantilever calibration, the signal (m) can be converted to force (N). Plotting the force against the distance that the z piezo has been replaced, one will obtain the force-distance (FZ) curve. However, the mechanical properties of the sample can only be obtained by converting the displacement of the piezo to the deformation of the sample. This is done by subtracting the bending from the cantilever from the z-piezo displacement (**equation (1.3.1)**), the resulting curve is called force-indentation curve.

For example, the stiffness of the liposomes was obtained from the slope of the force-indentation curves obtained on top of the liposomes. Because the contact area between the tip and the liposome increases during the indentation, the load becomes more distributed and the measured stiffness (slope of the curve) is not constant during indentation. To quantify the influence of these variable boundary conditions and to relate the measured stiffness to the area compressibility K_a and bending rigidity K_b of the membrane, we modeled the experiment using the finite element methods (FEM) (section 2.2). A spherical shell model resting on a flat surface was indented by a hyperbolic AFM tip (**Fig 1.3.7**). The thickness of the shell was set to 3.1 nm (as explained in section 1.2.2) and the Young's modulus adjusted to match the experimental values. The force-indentation curve obtained from AFM overlaps very well with that from the modeling. **Fig 1.3.8 C** shows how the calculated varies with different boundary conditions.

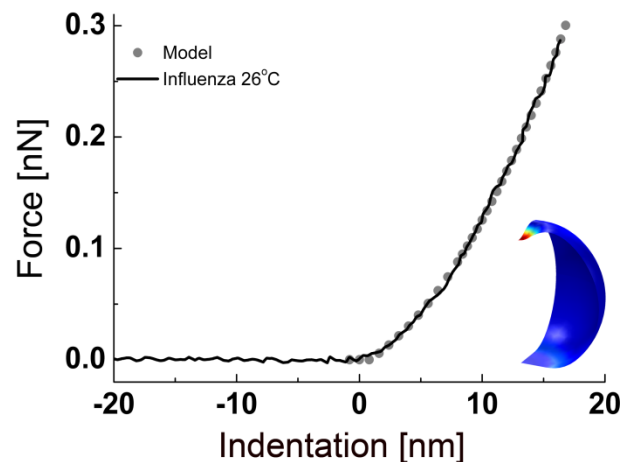


Fig 1.3.7 Average force vs. indentation curve of a 71 nm high influenza liposome, obtained by averaging 4 curves obtained within 20 nm from the center. The grey dots show the response calculated with FEM

($d = 70$ nm, $E = 30$ MPa), it overlaps well with the experimental curve. Inset: Deformation of the thin-shell model by a hyperbolic tip and a flat surface.

1.3.5. Tip shape characterization and tip-induced image artifacts

Most biological samples are soft and easily damageable. The probing of such samples is mostly performed in liquid. For this reason, bio-cantilevers are specifically developed. They have a low spring constant (0.03 N/m) and a small cantilever surface area to reduce their thermal noise. The short lever (30×60 μm) of the bio-lever BL-RC150VB from Olympus (Tokyo, Japan) is applied for all experiments in this thesis. The tip is V-shaped, of which the open angle is $\sim 30^\circ$, tip radius ~ 20 nm (**Fig 1.3.8 A**). Such tip geometry will cause 2 main artifacts when applied to samples with a comparable dimension (~ 100 nm). Firstly, when scanning the tip over the sample, the image is dilated. Secondly, when indenting on the sample, the increasing tip-sample contact area causes nonlinearity of the indentation curve. To quantify these artifacts, the tip was assumed to be radial symmetric, of which cross-section was modeled by a hyperbola with open angle θ (with respect to the symmetry axis) and radius R . The function of the tip cross-section can be written as:

$$y = \frac{1}{\tan\theta} \left(\sqrt{x^2 + \frac{R^2}{\tan^2\theta}} - \frac{R}{\tan\theta} \right) \quad (1.3.7)$$

where θ is the open angle and R is the radius of curvature of the tip.

Based on the manufacturer description, the tip cross-section is defined as $\theta=30^\circ$, $R=20$ nm. When it scans over a circle ($r=35$ nm), the trace of the tip apex resembles an inverse hyperbola, which radius is more than twice of the circle radius (**Fig 1.3.8 B**). **Fig 1.3.8 D** shows the relation between circle radius and image radius, which is also a hyperbola, but can be assumed to be linear when the circle radius is larger than 10 nm. In practice, the width of a spherical sample ($r\sim 50$ nm) imaged by this tip will be enlarged 2.5 times. This is important for the mechanics study of liposomes, which are easily deformable and damageable. Only images of liposome of which the width is within 2.5 ± 0.75 times of its height will be selected for data analysis, otherwise we suspected them to be strongly deformed or damaged. **Fig 1.3.8 C** shows the FEM modeling of a thin spherical shell indented by tips with different geometries towards different surfaces. When replacing point forces with planar surface and hyperbolic tip, the FZ curve shows a strong nonlinearity. Derivations to **equation (1.3.7)** and dilated image shape are available in section 4.2.

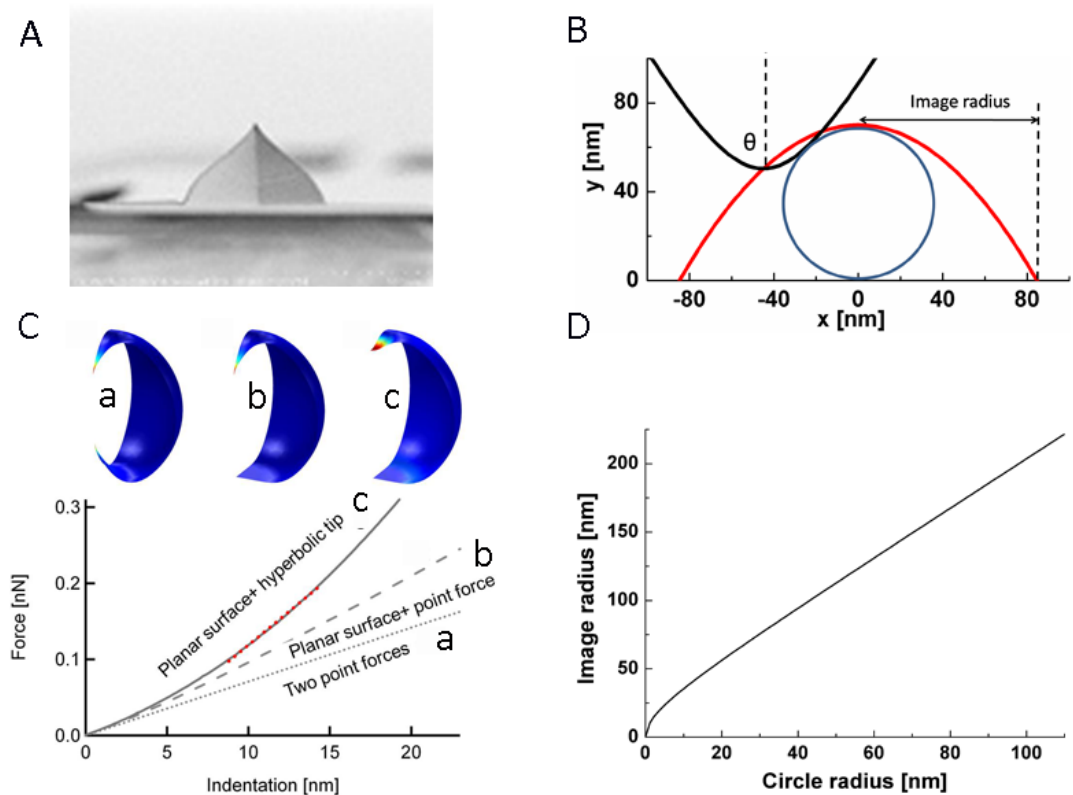


Fig 1.3.8 AFM tip induced artifacts in imaging and mechanics. (A) Scanning electron microscopy (SEM) image of an Olympus bio-lever BL-RC150VB tip. The tip is a hollow pyramid sliced in half vertically. (B) The tip is modeled by a hyperbola (black) with an open angle $\theta = 30^\circ$ (with respect to the symmetry axis) and a radius $R = 20$ nm. When a circular object (blue, $r = 35$ nm) is scanned by the tip, the trace of the tip apex gives the sample image (red). The image width is around twice of that of the original object width. (C) The modeled indentation depends on the applied boundary conditions. a) The liposome (100 nm, 40 MPa, 3.1 nm shell thickness) is symmetrically indented by two point forces. The force vs. indentation curve is linear and the slope follows: $E \cdot t^2 / d$. b) The liposome is supported by a planar surface and indented by a point force. During indentation the liposome get flattened onto the planar surface. This increasing contact area is visible in the curve as an increase in slope during the indentation. c) The liposome is supported by a planar surface and indented by a hyperbolic tip. The red dotted line between 0.1 and 0.2 nN, is the linear fit we used to define the stiffness of the liposomes. (D) Image radius versus object radius also shows a hyperbolic behavior, however, the relation is almost linear when the circle radius is larger than 10 nm. Image A is from *Olympus*.

1.3.6. Outlook of novel AFM methods

Although successfully applied to many fields for 25 years, traditional AFM is still limited by some of its drawbacks. Novel methods were developed to specialize AFM to carry out measurements which traditional ones cannot do. The first drawback is the slow scanning speed of AFM. In most cases, it takes minutes for a traditional AFM to capture an acceptable image, while it only takes seconds for EM. This has limited the AFM in visualizing the dynamics of samples which occur within the same time interval. The slow response speed of several AFM components limits the speed of the system, however, it is mainly limited by the slowest ones, which are the piezo elements and cantilever. To overcome these limitations, *Ando et al.* have developed high-speed AFM, which is able to obtain a 100×100 pixel image in only 80 ms (142). At such scan rate, dynamics of samples may be captured by AFM in almost real-time. The technique has been successfully applied to study the movement of myosin V molecules along actin tracks (143), kinesin along a microtubule (144), bacteriorhodopsin in purple membrane (145) and the kinetics of individual bacterial cell death (146). High-speed AFM can also be advantageous for mechanical measurements. The mechanical response at high speed can be measured which allows us to investigate the elastic and viscous response over a large bandwidth of frequencies.

The second drawback is the tip-induced artifacts. As shown in section 1.3.2, the size of an AFM tip is on the same scale as the sample, this leads to image shape dilation. Super sharp tips (radius~2 nm) have been developed to minimize the dilation (MSNL series, *Bruker*). The other artifact comes from the sample deformation when probed by the tip. Biological samples are usually very soft and required to be studied in liquid. This limits the imaging resolution because the sample is deformed during imaging. Cryo-AFM was developed to stiffen the sample and free it from liquid environment (147). This increased resolution but prohibits the possibility to observe sample dynamics or mechanics. High resolution images of red blood cells, DNA (148) and smooth muscle myosin (149) have been successfully obtained by this technique.

The third limitation is the minimal force that can be exerted on the sample. This is limited by the thermal noise of the cantilever in liquid to about 20 pN (150, 151). An alternative technique is optical trapping in which the probe is held by a focused laser beam instead of a cantilever. This results in noise levels of less than a pN, such that the response of very soft or fragile samples can be investigated at single pN forces (152). Details about such low force measurements are available in section 4.3.

Furthermore, AFM is compatible with other microscopy techniques. With an integrated AFM, the object of interest can be located conveniently first by light microscopy and then probed by AFM. This is especially useful in processing micrometer samples, such as cells. A good example of integrated AFM is the newly developed stimulated emission depletion microscopy-atomic force microscopy (STED-AFM) (153).

2. MECHANICS OF LIPOSOMES

2.1. Introduction to the experiments

Lysosomes, enveloped viruses, synaptic and secretory vesicles are all examples of natural nanocontainers (diameter ~ 100 nm) which specifically rely on their lipid bilayer to protect and exchange their contents with the cell. Most of the previously cited species act as physiological or pathological containers which are able to exchange molecules within a single cell or with the extracellular space by exchanging lipids with other vesicles or with the plasma membrane. Before any exchange occurs, lipid bilayers must act as a barrier against the external environment. Therefore liposomes can be used as a model to study such natural systems. Meanwhile, an increasing number of applications based on liposomes have been developed for the purpose of drug delivery and cosmetics. We are interested in studying the mechanics of liposomes, aiming at understanding the physics of lipid bilayers forming a stable curved structure.

First, we applied AFM to investigate the mechanical properties of liposomes made from single type of lipids. Our measurements on DMPC liposome in fluid phase were in very good agreement with the mechanical properties obtained from the same lipid in GUV (108), and the expected stiffness increase upon cholesterol addition could be clearly resolved. The DOPC liposomes were tested at different temperatures above its transition temperature, no obvious phase transition was observed.

Second, to compare the effect of lipid compositions on the mechanics of liposomes, we also applied the same measurement on liposomes made from myelin membrane lipid. The bending rigidity of myelin membrane lipid is slightly less (30%) than that of the liposome made from influenza lipid, probably because it contains less cholesterol and longer-chain-lipids.

Third, we applied AFM to investigate how the influenza A virus uses its lipid envelope to protect itself. Lipids were purified from influenza A/PR8 and A/Japan and extruded into liposomes with comparable dimensions. They were found to be rather stiff compared to DMPC:cholesterol liposome and myelin lipid liposome but remained flexible and reversibly deformed at rather high indentations. Most viruses, enveloped or non-enveloped, rely on stiff protein shells to keep the genome from being damaged by external environment. However, the strategy employed by the influenza virus is an exception. We found that the lipid envelope dominates its mechanical properties, which indicates that the influenza virus may rely mainly on the lipid envelope to protect itself. This is of particular interest, as lipid bilayers at such curvature were previously considered to be less stable than GUVs and planar bilayers (107). Not to mention that bilayers present in the latter forms are much less rigid as compared to protein shells.

Influenza viruses can be transmitted between animals, human, and between animals and human. During the transmission, the virus will be exposed to various environments both outside and inside a host organism. To successfully enter the host body, influenza virus has to be able to survive certain environmental changes. Here we showed that the stiffness of viral liposomes (and thus the structure) is

hardly affected by different temperatures (13, 26, and 37°C), no major transition in stiffness or elastic behavior was observed upon temperature decrease: This suggests that, the influenza virus envelope is rather fluid and, instead of going through a major phase transition, progressively orders between 10 and 40 degrees, as was previously shown (110). Next, liposomes made from A/Japan influenza viruses were tested at pH 5, pH 7.4 and pH 5 neutralized to pH 7. No obvious difference in stiffness was observed.

We also tested the mechanical properties of the liposomes in extreme conditions. Both liposomes and viruses were punctured with force up to several nN and were found to recover immediately afterward. The average break force of influenza liposomes was lower than that generally observed for supported fluid planar bilayers but was in a similar range to that of protein capsids (25, 154). We thus extended the tests on virus in extreme conditions. Dehydration was also performed on the virus, almost 50% of the viruses showed a comparable stiffness after rehydration. These findings are supporting the facts that, influenza virus can survive for one to two days on dry, hard, non-porous surfaces; 8-12 hours in on cloth, paper, and tissues (155); and up to 17 days in dried mucus on banknotes (31). We therefore show that a relatively stiff, yet fluid lipid bilayer as a protective envelope is as good a strategy as utilizing protein shells with high stiffness.

The myelin lipids were provided by M. Simons from MPI for experimental medicine, Goettingen. The influenza lipids were provided by C. Sieben at HU-Berlin. The puncturing and Zeta potential measurements of influenza liposomes were performed by Dr. F. Eghiaian at the University of Goettingen. Part of this chapter has been published in (30).

2.2. Materials and methods

Lipids

1,2-dimyristoyl-sn-glycero-3-phosphocholine (DMPC), 1,2-di-(9Z-octadecenoyl)-sn-glycero-3-phosphocholine (DOPC) and cholesterol used in this work were purchased from Avanti Polar Lipids (Alabama, USA).

Myelin lipid was purified by homogenizing of brain tissue from 1 year old mouse (2 mice) in PBS containing protease inhibitors by sonication. The brain homogenate was put on top of two-step sucrose gradients (0.32 and 0.85 M sucrose in preparation buffer containing 5 mM EDTA and 10 mM Hepes, pH 7.4). After the gradients were centrifuged at 75,000 g for 30 min, the interfaces were collected, diluted at least 10 times with H₂O, and centrifuged at 75,000 g for 20 min. The pellet was washed twice with H₂O and recovered by 10-min centrifugations at 12,000 g (crude myelin), and the protocol was repeated to obtain purified myelin (156, 157). The lipid was then dried for use. Myelin contains about 30% proteins and 70% lipids. The protein part contains myelin basic protein (MBP), myelin oligodendrocyte glycoprotein (MOG) and proteolipid protein (PLP). The lipid part contains cholesterol, phospholipids, and glycolipids in molar ratios ranging from 4:3:2 to 4:4:2 (158).

The lipid extraction of myelin was based on (159). 350 μ l of sample was added to 1050 μ l of 2:1 mixture of CHCl₃/MeOH (Chloroform/Methanol). After vortexing, it was centrifuged for 5 minutes at 6000 rpm at room temperature. The organic phase (lower phase) was recovered and 70 μ l of Methanol, as well as 475 μ l 50 mM NaCl were added. After vortexing again, the centrifugation step was repeated. Once more, the organic phase (lower phase) was recovered and then placed in a 1.5 ml eppendorf tube in a speed vacuum until it was dry.

Influenza lipids were extracted from A/PR8 and A/Japan influenza virions that were purified from hen eggs following the procedure described by *Korte et al.* (160). A PBS suspension of influenza viruses was treated with chloroform/methanol: Lipids were extracted following *Bligh & Dyer* (161). The proteins were separated from the lipids with methanol/chloroform (2:1) phase-separation. The total amount of phospholipids recovered after extraction was determined following *Böttcher et al.* (162). The lipid composition for egg-purified PR8 influenza viruses was determined via Thin-layer Chromatography (in molar %): Sphingomyelin (22.1), phosphatidylserine (22.2), phosphatidylethanolamine (33.3), phosphatidylcholine (15.1). The ratio of cholesterol over total lipids was 0.43 as determined by an enzymatic assay (163).

Liposome preparations

DMPC, DOPC and myelin lipids were resuspended in deionized H₂O for extrusion; influenza A/PR8 viral lipid was resuspended in 5 mM Hepes, 150 mM Sodium Chloride at pH 7.4 and influenza A/Japan lipid was resuspended in PBS at pH 7.4 at a 1 mM final concentration. All SUVs were prepared by a classic extrusion method (164). To make unilamellar liposomes, dried influenza A/PR8 powder were

resuspended in 5 mM Hepes, 150 mM Sodium Chloride at pH 7.4 and A/Japan lipid powder were resuspended in PBS at pH 7.4 at a 1 mM final concentration. After vortexing and sonicating the suspension (1 min each), the lipids were frozen in liquid nitrogen and thawed in a hot water bath. After 5 freeze-thaw cycles, lipids were extruded 31 times through 2 layers of 100 nm filters (Whatman, Kent, UK). This procedure is known to yield > 90 % unilamellar vesicles (165). Influenza lipids were kept under nitrogen at all times.

Surface chemistry

All glass substrates were first thoroughly cleaned by KOH etching, and subsequently coated with a positively-charged 3-[2-(2-Aminoethylamino)ethylamino] propyltrimethoxysilane (DETA). About 10 g of KOH were first dissolved in 20 ml water and supplemented with 200 ml ethanol. Microscope coverslips placed in a Teflon holder were immersed in the KOH-filled container. The container was sonicated in a bath sonicator for 5 minutes; subsequently both the container and rack were rinsed and sonicated 3 times in filtered and deionized water, each time 5 minutes. For the silanization step the coverslips were sonicated again for 5 minutes in a container filled with fresh water, to which 200 μ l of DETA (Sigma Aldrich) and 30 μ l of acetic acid were added. Next, the coverslips were sonicated for 5 minutes in clean water, three times. Finally the Teflon rack was placed in an oven until the coverslips were completely dry (20 minutes at 100 °C). The cover glass for single virus tracking was cleaned with the same procedure but without the silanization step and the last 3 washing steps.

Differential scanning calorimetry

The Differential Scanning Calorimetry (DSC) measurement was carried out on a VP-DSC Differential Scanning Calorimeter (GE Healthcare Europe GmbH, Freiburg, Germany). 250 μ l liposomes (1 mM) were filled into the sample chamber; 250 μ l deionized water was filled into the reference chamber. The sample was measured 3 times at 10°C/hour rate to collect the data.

Zeta potential measurement

The Zeta potential of influenza liposomes was measured on a Malvern ZetaSizer Nano (Worcestershire, UK). A stock of liposomes at roughly 1 mM in PBS was diluted to 1/100 in an aqueous solution that was buffered to the desired pH value. Hepes 5 mM pH7.5, Mops 5 mM pH7.0, MES 5 mM pH 6.0, Citrate 2 mM pH 5.0, and acetate 2 mM pH 3.7 were utilized.

AFM and cantilevers

A MFP-3D (Asylum Research, Santa Barbara, Ca, USA) and cantilevers (Olympus BL-RC150VB, spring constant $k_{cl} = 0.02869 \pm 0.005$ N/m avg. \pm sd, $n=264$, tip radius ≈ 20 nm, statistics shown in **Fig 2.2.1**) were used for all AFM experiments. Viruses were diluted 200-400 times in PBS the appropriate buffer and 100 μ l of the dilution was deposited on a DETA surface.

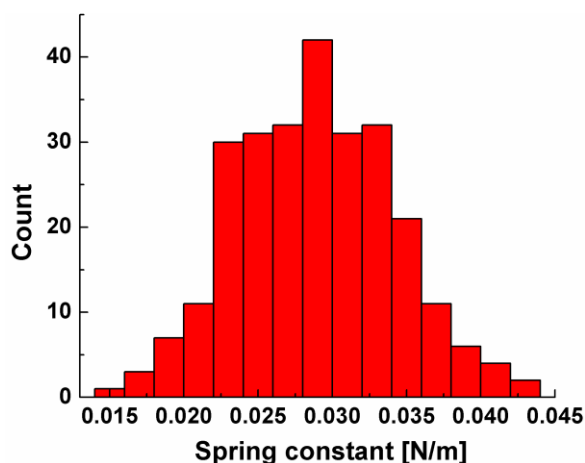


Fig 2.2.1 Statistics of the spring constant of the Olympus BL-RC150VB biolever. 264 cantilevers were analyzed. The average spring constant $k_{cl} = 0.02869 \pm 0.005$ N/m (average \pm standard deviation).

Except for A/PR8 liposomes, all AFM experiments were carried out in PBS. The pH of the sample was adjusted by adding sodium citrate to PBS until the pH reached the desired value, and the virus stock (1mg/ml) in PBS was 500x diluted in this buffer and kept at least 30 minutes at room temperature before the AFM analysis. To test the reversibility of the incubation of viruses at low pH, viruses were first incubated in acidic buffers at 37°C for 20 minutes and brought back to pH 7 by diluting them in large amounts of PBS.

Force mapping

There are a couple of ways to carry out indentation experiments on the sample to extract its stiffness: the simplest of which is to perform one or more single indentations at one point of the object (usually in the center). This is straight forward and time saving, however, contains many possible errors. Firstly, biological samples are mostly complex systems, which can exhibit inhomogeneous properties over different parts. This means the different areas may exhibit a different stiffness. Secondly, the always-existing thermal drift will dislocate the sample, sometimes up to 1 nm/second. After imaging (which

takes 2-5 minutes), the object has laterally drifted away already. As a consequence, the actual indentation point will be different from the intended location.

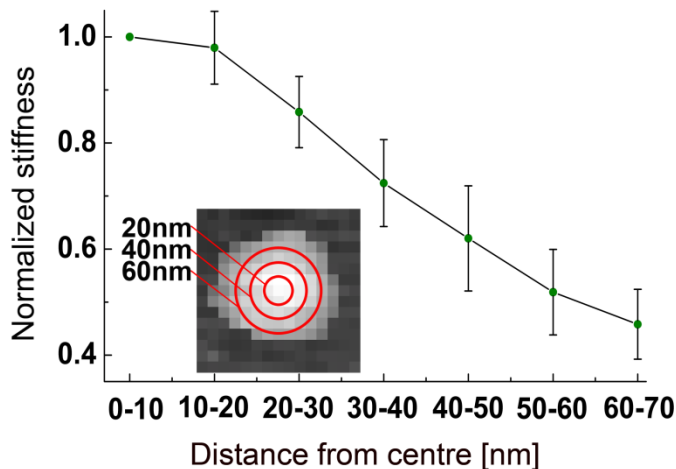


Fig 2.2.2 Dependency of the influenza liposome stiffness on the probed region. The liposome was divided in concentric areas for which the average stiffness was measured (eg. the pixels enclosed by the circles of 30 and 40 nm radius). The plot shows the normalized stiffness for 15 liposomes, the stiffness decreases when the liposome is probed further away from its center.

Fig 2.2.2 shows the dependency of probed region on the obtained stiffness of liposomes. If probed 40 nm away from the center, the stiffness can be only 65% of the real value. A more collective and precise method can be applied to minimized the errors mentioned, which collects the mechanical information of a region instead of a single point (shown in **Fig 2.2.3**). Force mapping (or also called force volume) was first applied to study the mechanics of synaptic vesicles (166). The stiffness of the particles were collected by first imaging a $3 \times 3 \mu\text{m}$ area in tapping mode to locate the particles and then zooming in to a $400 \times 400 \text{ nm}$ area around each particle to do force distance (FZ) curves on an array of 24×24 points, at a curve rate of 2.4 Hz. To avoid damaging the viruses and liposomes, all force maps were acquired by applying forces less than 0.25 nN. The measurements were repeated on approximately 50-100 particles in each condition for each particle species. All mechanical measurements present in this thesis were performed by force mapping.

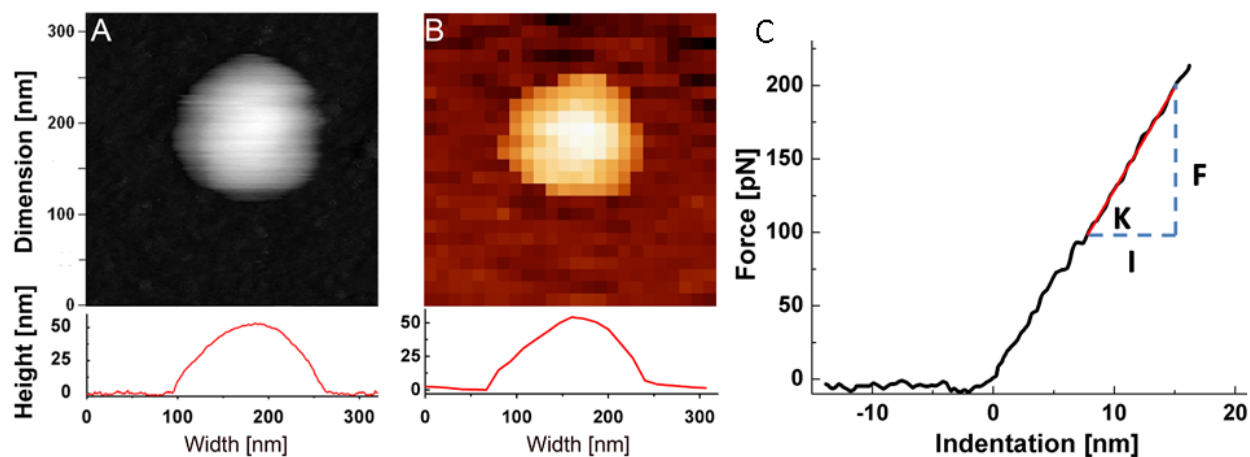


Fig 2.2.3 Force mapping procedure. (A) Objects are imaged in the center of a $\sim 300 \times 300$ nm area. (B) The AFM is then switched to force mapping mode, in which the tip performs indentation curves on an array of 24×24 points. The FZ curves collected contain the mechanical information of this area. The object is less likely to be damaged or deformed, because the force is always applied in the vertical direction. The cross-section profiles underneath the images in A and B show no difference in both shape and height. (C) The force mapping data is further processed by a program written in *LabVIEW* (Austin, TX), which converts the FZ curves to force-indentation curves. To minimize errors, 2-6 FZ curves from the central area of the object in the force map (radius=20 nm) are averaged, and then corrected using the particle stiffness analysis routine (explained below). Linear fitting between 100-200 pN is then performed on the averaged indentation curve to quantify the spring constant of the object.

Particle stiffness analysis

As liposomes are expected to be spherical particles, only approximately spherical liposomes were considered for further analysis. For each imaged liposome the height was used to calculate the expected dilation effect of imaging with a hyperbolic tip. If the width of the imaged liposome deviated by less than 30 % from this expected width, it was considered acceptable. However, this routine was not applied to viruses, as the viruses can be pleomorphic.

Routines written in LabVIEW (National Instruments, Austin, Tx, USA) were devised to perform the following operations on force maps:

- Create a height image by defining for each pixel the Z-piezo position at which the liposome gets touched (i.e. when the cantilever starts to bend).
- Fit a plane to the background height points and subtract this from the height image.
- Average the FZ curves obtained on the background glass surface and perform a linear fit to obtain the slope, which allowed for an in situ calibration.

- Find the centre of the particle by the averaging the X-Y position of the 8 highest pixels
- Align and average the FZ-curves obtained on the liposomes. The particle image was divided into concentric circular regions and average FZ curves were calculated for each region. (After comparing the different regions, only curves obtained within 20 nm from the center were used). On average, 4 curves were selected and averaged per particle.
- Obtain the stiffness for each region on the liposome (k_{ms}) by performing a linear fit between 0.1 and 0.2 nN on the average FZ curves, this stiffness is the combined stiffness of the cantilever (k_{cl}) and the sample placed in series.
- Extract the liposome stiffness (k_l) following:

$$k_l = (k_{ms}^{-1} - k_{cl}^{-1})^{-1} \quad (2.2.1)$$

Influenza membrane puncturing

Force maps recorded at nN forces most often resulted in displaced or irreversibly damaged liposomes and could therefore not be used to analyze the response of liposomes at such a high force range. Hence DETA-bound influenza liposomes were subjected to single point pushes on top of them, performed at forces going up to 2 nN and at a loading rate of 1 $\mu\text{m/s}$: After tapping mode imaging liposomes were generally subjected to 4 consecutive pushes at 2 nN, then imaged again to verify that the pushes were performed in the center of the liposome. If the particle was not removed after the pushing cycles, another cycle was performed. 9 FZ curves were performed on average per particle, corresponding to 2-3 cycles of imaging/pushing. Puncturing was defined as a negative change in the FZ slope which amplitude exceeded twice the standard deviation of the 'non-contact' part of the FZ curve.

Finite element modeling

To compute the relation between the diameter of a liposome, its spring constant and the membrane elasticity we modeled the indentation of a spherical shell with the AFM tip by finite element methods (COMSOL Multiphysics 3.5, Comsol, Stockholm, Sweden). The sphere was set to be resting on a rigid flat surface. The radial-symmetric AFM tip with a hyperbolic cross-section profile $f(x)$ was used to indent the vesicle, which is given in **equation (1.3.7)**.

The tip radius t_r was set to 20 nm, and the open angle θ (with respect to the symmetry axis) to 30°. The contacts between the shell and the tip and the supporting surface during indentation were implemented with a contact-penalty stiffness method according to the manufacturer's manual. The model was simplified to a quarter sphere by making use of the symmetry planes, and meshed with over 2000 thin

shell elements. A parametric, non-linear solver was used to simulate the stepwise lowering of the tip onto the sphere.

The elastic properties of the thin shell elements used in the model are described by its Young's modulus E and the shell thickness t , which is set as 3.1×10^{-9} m according to section 1.2.2. Such a reduced thickness (with respect to the real thickness of lipid bilayers) can be understood as the effective thickness of the lipid bilayers. The two leaflets are replaced by a thinner single sheet to maintain the same bending rigidity. Indentation curves for models with diameters from 30 nm to 120 nm were calculated, varying the Young's modulus between 8 and 75 MPa in steps of 1 MPa. The stiffness of the theoretical FZ curves was obtained by a linear fit between 0.1 and 0.2 nN. The bending rigidity K_b and area compressibility modulus K_a can be converted from E by **equation (1.2.2)**.

Water compression in the vesicles is inexistent on the time- and length-scale of the experiment, due to the relative high rate of water transport across the membrane. A 100 nm diameter liposome has a surface area of 31×10^3 nm² and the permeability of its lipid bilayer is on the order of 1×10^4 nm/s, assuming a fluid state (167): Hence 3×10^8 nm³ water diffuses through the lipid bilayer in a second, which exceeds the volume of the liposome (5×10^5 nm³) by almost three orders of magnitude. In the case of influenza liposomes that were prepared in 150 mM salt buffer, the effect of the osmotic pressure building up with indentation is also negligible. For a 100 nm diameter liposome the osmotic pressure calculated from our model is 3 kPa at a 15 nm indentation, at 0.2 nN. The local pressure applied by the AFM tip, is much higher, approximately 3 MPa under similar conditions.

Inspired by the fact that, for a given shell model (with fixed d , t , and boundary conditions) E is the only varying parameter for the fitting of stiffness vs. diameter plot, an empirical equation was established to relate the liposome stiffness, its height and the Young's modulus with only 4% deviation:

$$k_l \approx \frac{47 \times 10^5 \times E^{0.53} \times t^2}{d^{0.66}} \quad (2.2.2)$$

Equation (2.2.2) is a simple and precise way of predicting the Young's modulus of a liposome based on the stiffness vs. diameter data without FEM calculation. It is also used by us to calculate the average stiffness of a liposome species. To compare the stiffness of liposomes with different lipid compositions or temperatures, a stiffness vs. height graph was plotted for each species. The Young's modulus for each liposome species was determined by minimizing the residual error for vesicles between 50 and 120 nm, when fitted to the experimental data. Then **equation (2.2.2)** was fitted to the experimental data by minimizing the residual error for all vesicles. The average stiffness k_{100} , the stiffness of a 100 nm high liposome, was determined using the fitting constant E . To estimate a 'standard error' for the determination of k_{100} we used the square root of the sum of squared residual from the fitted data, divided by the number of measurements (n).

2.3. Results

2.3.1. Mechanics of liposomes made from pure lipids

Cholesterol effect on the stiffness of DMPC liposomes

To verify our method, pure lipids, of which the mechanical properties are well-studied, were tested. The phase transition temperature of DMPC lipid was determined from DSC measurements. A differential power band of 0.15 mCal/min was applied to a sample of DMPC liposomes, rising the temperature from 15°C to 35°C. The result (23.64°C Fig 2.3.1 A) agrees well with the manufacturers description (23°C, Avanti Polar Lipids, Alabama, USA). We first tried measuring the stiffness of DMPC liposomes at 13°C, 26°C and 31°C, however, no clear difference in stiffness was observed between the species. Next, the stiffness of DMPC and DMPC:cholesterol 1:1 (mol:mol) liposomes was measured by AFM at 26°C. The stiffness and the best fitting FEM model are shown in Fig 2.3.1 B.

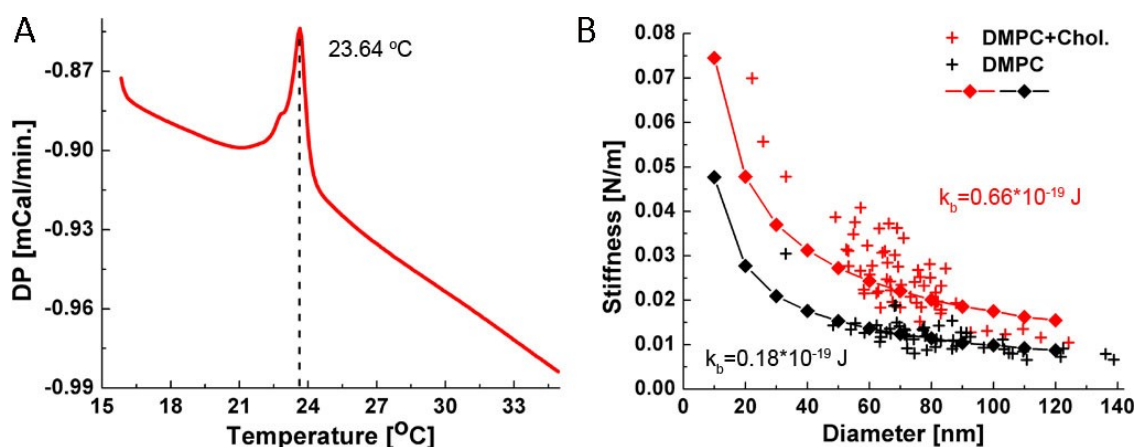


Fig 2.3.1 (A) Phase transition temperature of DMPC lipid determined from the DSC method. The heat flow over temperature plot was averaged from 3 independent measurements, a peak at 23.64°C indicates the phase transition temperature of DMPC liposomes. (B) Stiffness vs. diameter plot of DMPC and DMPC:cholesterol 1:1 (mol:mol) liposomes: Black crosses: DMPC liposomes, Red crosses: DMPC:cholesterol (1:1, mol:mol) liposomes. Each scatter plot was overlaid with a finite element model of the liposome indentation by AFM. The k_b values of both species are given according to their colors.

Phase transition of DOPC liposomes

DOPC contains two unsaturated chains in the structure, therefore exhibits much lower phase transition temperature (-20°C) as compared to DMPC. We applied the same method on DOPC liposomes at 13°C and 31°C , only a small difference in stiffness was observed. This is consistent with the absence of a phase transition in this temperature range.

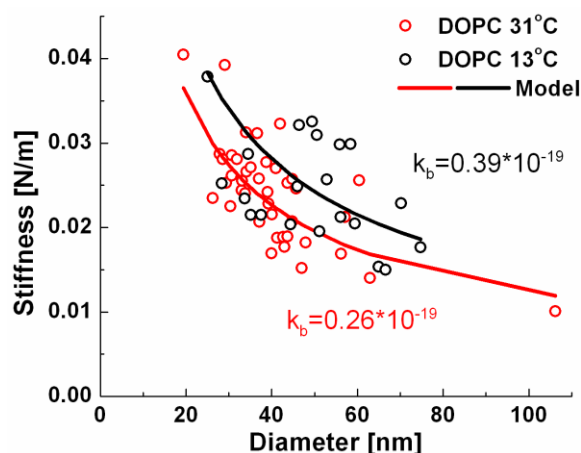


Fig 2.3.2 Stiffness vs. diameter plot of DOPC liposome at 13°C (black circles) and 31°C (red circles). The data is fitted by **equation (2.2.2)** by minimizing the residual error. The k_b values of both species are given according to their colors.

2.3.2. Mechanics of liposomes made from myelin lipids

As presented by (128) in Section 1.2.3, a mixture of lipids may result in membrane deformation due to the difference in length, structure, and interaction of lipids. Liposomes composed of different lipid mixtures may therefore show different stiffness. Myelin is a multilayered stack of uniformly thick membrane that forms a layer around the axon of a neuron. It is electrically insulating so that the signal transmitted via the neurons can be protected. The cholesterol and phospholipid contents in myelin is very similar to that of influenza A/PR8 lipid (both $\sim 40\%$); however, the other lipid composition is quite different: myelin lipid contains $\sim 20\%$ glycolipid called galactocerebroside; while influenza A/PR8 lipid contains 13% sphingolipid called monohexosylceramide (shown in **Table 1**). This makes the myelin lipid an ideal control to see the lipid composition effect on its mechanics. To do so, myelin was purified from brains of 1 year old mice (2 mice); the lipid is further purified from the myelin and extruded into liposomes by the method described. The stiffness of the myelin liposome (black) was measured and compared to that of DMPC (red) and influenza (blue) liposomes **Fig 2.3.3**.

Table 1: Properties of the head groups of influenza and myelin lipids (in molar % of the total lipids). These numbers were obtained from our measurements (influenza lipid, materials and methods), and from literature (myelin lipid) (158, 168-170).

	Influenza lipid (egg-purified PR8)	Myelin lipid (mouse)
Cholesterol	43%	38.8%
Phospholipid	44%	38%
Phosphatidylserine	9.8%	5.1%
Phosphatidylethanolamine	14.7%	15.3%
Phosphatidylcholine	6.6%	12.7%
Sphingomyelin	9.7%	4.9%
Sphingolipid	13%	
Monohexosylceramide	13%	
Glycolipid		20.2%
Cerebrosid		13.8%
Cerebroside sulfate		4.7%
Ceramide		1.7%
Uncharacterized		3%

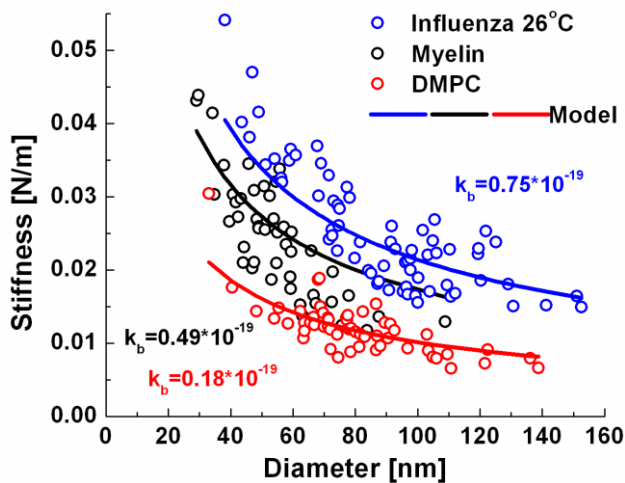


Fig 2.3.3 Stiffness of influenza (blue circles), myelin (black circles) and DMPC (red circles) liposomes. The stiffness was fitted by **equation (2.2.2)** (lines). Myelin liposomes are on average 70% stiffer than DMPC liposomes, yet 20% softer than influenza PR8 liposomes. The mechanical parameters are given in **Table 2**. The k_b values of the species are given according to their colors.

Table 2: Mechanical parameters of different liposomes. (The temperature is 26 °C, if it is not mentioned)

	k_{100} (nN/nm)	E (MPa)	K_b (J)
DMPC (n=55)	0.010±0.0003	11	0.18*10 ⁻¹⁹
DMPC+chol. 1:1 (mol) (n=60)	0.020±0.0008	40	0.66*10 ⁻¹⁹
DOPC, 13 °C (n=21)	0.015±0.0003	24	0.39*10 ⁻¹⁹
DOPC, 31 °C (n=41)	0.012±0.0003	16	0.26*10 ⁻¹⁹
DPPC, gel phase (171)	n.d.	115	~1*10 ⁻¹⁸
Influenza A/PR8, 13 °C (n=53)	0.027±0.0011	68	1.13*10 ⁻¹⁹
Influenza A/PR8, 26 °C (n=68)	0.021±0.0007	45	0.75*10 ⁻¹⁹
Influenza A/PR8, 37 °C (n=60)	0.019±0.0006	37	0.61*10 ⁻¹⁹
Influenza A/Japan, pH 7.4 (n=94)	0.020±0.0004	52	0.87*10 ⁻¹⁹
Influenza A/Japan, pH 5 (n=65)	0.019±0.0006	50	0.83*10 ⁻¹⁹
Influenza A/Japan, pH 5→7 (n=82)	0.017±0.0005	42	0.70*10 ⁻¹⁹
Myelin liposome (n=48)	0.017±0.0007	30	0.49*10 ⁻¹⁹

2.3.3. Mechanics of liposomes made from influenza viral lipid

Comparison of liposomes made from influenza viral lipid and DMPC lipid

We have tested the method on liposomes made from one type of lipid and having validated the quantitative results with values from literature. Next, we investigated the mechanics of liposomes made from natural lipid mixtures. In the present study we investigated the mechanical properties of the influenza lipid envelope being devoid of viral proteins. For this purpose we prepared mimics of the influenza lipid envelope that consisted of SUV made from lipids purified from influenza virus (A/PR8 strain). SUV obtained by extrusion are comparable in size with influenza virions, and therefore allow performing a direct characterization of the virus lipid properties in a physiologically and geometrically relevant context.

After extrusion the diameter of influenza liposomes was distributed between 40 and 150 nm. The stiffness of liposomes is expected to vary as function of their size. **Fig 2.3.4 A**, in which the stiffness vs. height was plotted for 68 individual influenza liposomes, shows a clear negative correlation, and an average stiffness for a 100 nm diameter particle k_{100} of 0.02 ± 0.003 nN/nm. For a hollow, thin walled spherical vesicle made out of a homogenous material and subjected to two opposing point loads, the

diameter d scales with the reciprocal of the stiffness k ($d \propto 1/k$) (12). In our experiments however there are two reasons why this scaling may be violated:

1) The vesicles are indented with an AFM tip and supported by a planar surface, giving rise to non-linear boundary conditions.

2) The vesicles are composed of a lipid bilayer, in which the leaflets can slide on each other, and in which the lipids can diffuse in the plane of the layer. Nevertheless plotting the reciprocal values of the stiffness vs. height (**Fig 2.3.4 B** green crosses) shows that the diameter of the particles scales almost exactly with $1/k$, suggesting that SUV do not have an unexpected mechanical behavior.

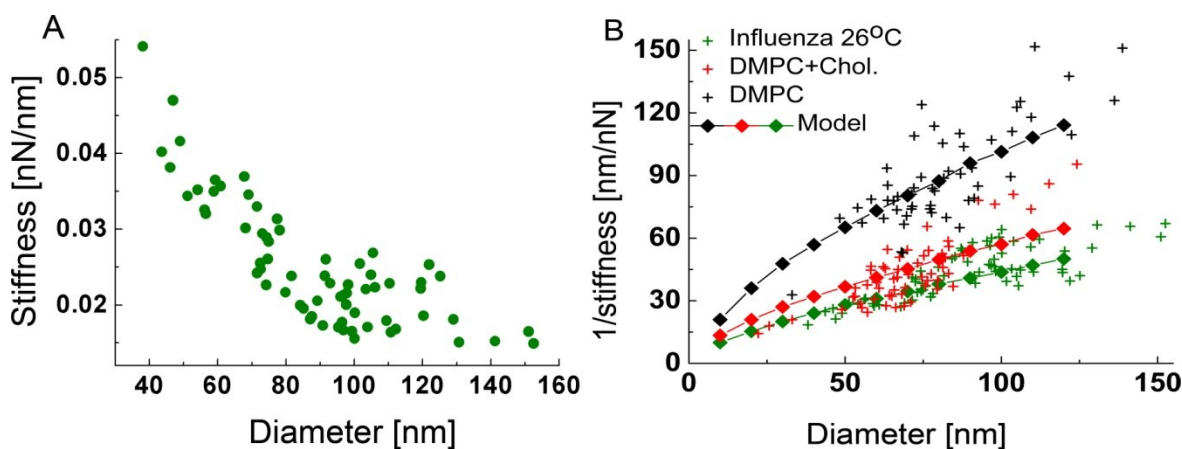


Fig 2.3.4 Stiffness of influenza and DMPC liposomes. (A) Stiffness vs. diameter plot of influenza liposomes. The stiffness of liposomes increased with decreasing liposome diameter. (B) $1/\text{stiffness}$ vs. diameter plot of influenza liposomes compared with DMPC and DMPC:cholesterol 1:1 (mol:mol) liposomes: Green crosses represent the reciprocal of the data presented in Fig. 2A. Black crosses: DMPC liposomes, Red crosses: DMPC:cholesterol (1:1, mol:mol) liposomes. Each scatter plot was overlaid with a finite element model of the liposome indentation by AFM. After fitting the stiffness distributions with **equation (2.2.2)**, the average stiffness for a 100 nm diameter vesicle was calculated. From the ratio of the average stiffness values, we found that the DMPC:cholesterol liposomes were on average 100 % stiffer, and influenza liposomes 110 % stiffer than DMPC liposomes.

The FEM calculation was repeated for liposome diameters from 10 to 120 nm, and the stiffness was matched to the experimental data (**equation (2.2.2)** in Materials and methods). The green diamonds in **Fig 2.3.4 B** show that the model describes well the height dependency of the liposome stiffness, but the relation between $1/k$ and d is not exactly linear. For small liposomes the AFM tip is relatively large compared to the vesicle such that it effectively is squeezed between two plates, rather than being

indented with a sharp tip, as is the case for larger vesicles. This effect of the relative tip size compared to the liposome size shows in the simulation as a shallow kink in the curve around 40 nm (**Fig 2.3.4 B**).

The actual data in **Fig 2.3.4 B** shows a rather opposing trend, the model underestimates $1/k$ for the larger particles, which may relate to an increased effect of the fluidity for larger liposomes, reducing their stiffness. Our model assumes continuum mechanics, and therefore does not account for the fluidity of the lipids in the leaflets (which in principle can be implemented in custom written packages (172)). The mobility of lipids is particularly important when the membrane is to undergo large changes in shape and curvature. In our experiments such changes are most pronounced for larger liposomes. The radius of the AFM tip is relatively small for these liposomes, such that the induced change in curvature will be large.

Influenza lipids were much stiffer than DMPC liposomes and even stiffer than DMPC:cholesterol (1:1) liposomes, although the latter species have a comparable fraction of cholesterol. This relates to the composition of the influenza lipids, which has longer and saturated acyl chains. In spite of their higher stiffness influenza lipids were found to have a K_a and K_b reflecting a rather fluid phase at 26 °C.

The lipid envelope dominates the mechanics of the influenza virus

The genome of the influenza virus is enveloped by a lipid bilayer which inner leaflet is covered by a layer of M1 matrix protein (**Fig 2.3.6 B**). To verify which of the two layers dominates the mechanics, we measured the stiffness of influenza viruses and of liposomes made from influenza viral lipids. AFM force mapping was performed on individual particles adsorbed on a silanized glass substrate. To achieve better statistics, we repeated the measurements on approximately 50-100 particles in each condition for each species. Using the method described in section 2.2, we obtained the stiffness of each particle. The stiffness of the particles usually shows a large variety, it is therefore necessary to estimate the average stiffness. For particles with an approximately fixed dimension, such as non-enveloped protein viruses, it is usually enough to plot the stiffness in a histogram and perform Gaussian fitting, as did by (12, 20). However, for particles which exhibit a large variety in dimensions and a dimension-dependent stiffness, the averaging is more complicated. We plotted stiffness of the particles versus their height to take the heterogeneity of virions into account, and the data was fitted with **equation (2.3.1)**, as for hollow spheres such a scaling is expected (12).

$$k = \frac{a}{d} \tag{2.3.1}$$

where k is the stiffness, d is the diameter and a is the fitting parameter.

We did not use **equation (2.2.2)** because this is not expected to describe the deformation of a lipid bilayer and a protein layer.

The stiffness at 100 nm diameter is taken as the average stiffness of the species, since the 100 nm is similar to the average diameter of influenza virus. The averaging method is shown in **Fig 2.3.5**.

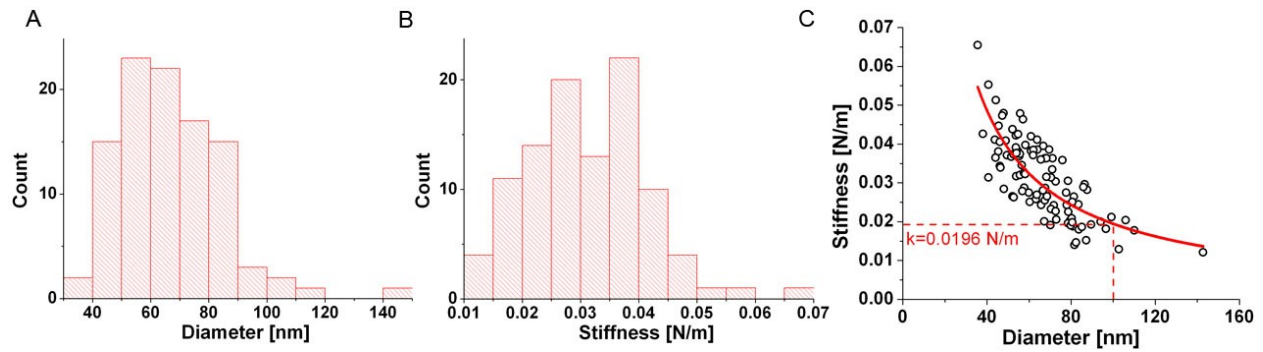


Fig 2.3.5 An example showing the stiffness of liposomes made from influenza A/Japan virus at pH 7.4. To average the stiffness, 94 particles were measured (according to section 2.2) at the same conditions. (A) Their diameters and (B) stiffness are plotted as histogram. (C) Their stiffnesses are plotted against their heights (black circles). A reciprocal function is fitted to the plot (red curve), the stiffness at diameter=100 nm represents the average stiffness of this sample (0.0196 N/m).

The stiffness of the liposomes made from A/Japan influenza viral lipid envelope was compared that of the intact A/X-31 virus (**Fig 2.3.6, Table 2** and **Table 5**). For both species, we determined the average stiffness K_{100} , which is used for quantitative comparison. The viral envelope alone has 70.4% (0.019 ± 0.0004 N/m compared to 0.027 ± 0.0006 N/m) of the stiffness of the intact virus.

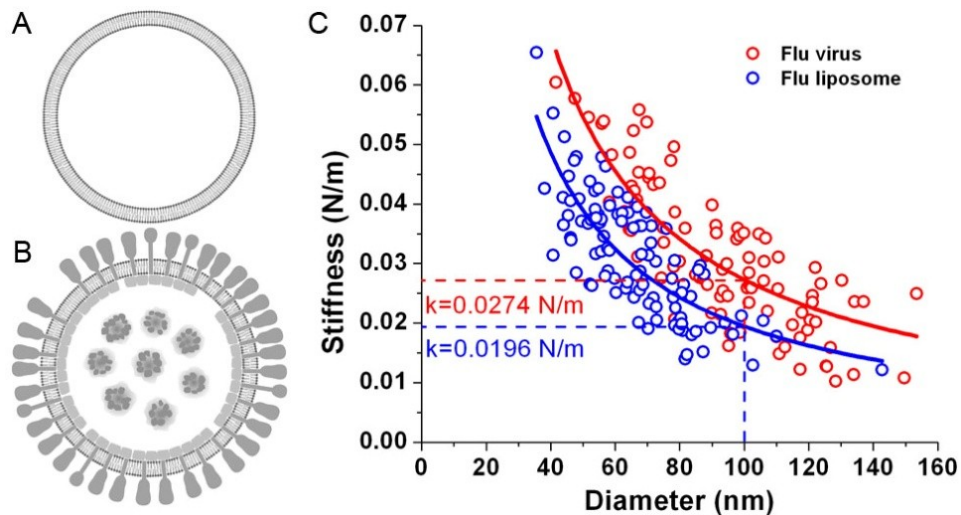


Fig 2.3.6 Schematic drawing of (A) liposomes and (B) influenza A virus. (C) Stiffness vs. diameter plot of influenza A/X-31 viruses (red) and liposomes (blue) made from influenza A/PR 8 viral lipid. Both fitted with reciprocal function. The average stiffness of the viral liposome is 70.4% of that of the intact virus.

The lipid envelope of influenza virus is mechanically stable at various environmental parameters

-Temperature

Influenza virions are subjected to a range of temperatures that can alter the organization of their envelope and potentially their survival rate during their lifecycle. To study the physical properties of the influenza lipid at different temperatures, we performed both DSC and AFM measurements.

According to (110), the influenza lipid membrane remains in fluid phase from 0°C to 50°C. To verify this, we tested the phase behavior of influenza PR8 liposomes with DSC. A differential power band of 0.15 mCal/min was applied to the liposomes, rising the temperature from 5°C to 40°C **Fig 2.3.7 A**. However, no peak was observed, indicating that no phase transition occurs in this temperature range, which confirms the findings of (110). We further performed stiffness measurement on influenza liposomes made from the same lipid at 13 ± 2 °C, 26 ± 2 °C and 37 ± 1 °C (**Fig 2.3.7 B** and **Table 2**). The average stiffness values decreased with increasing temperature. Influenza liposomes were always flexible (reversibly deformed, **Fig 2.3.8**) when pushed with < 0.3 nN forces and the change of stiffness was less than two-fold between 13 and 37 °C, suggesting that influenza liposomes do not undergo a large transition to a rigid gel or solid phase at lower temperature. Such behavior agrees with the findings of *Polozov et al.* (110) who had determined that the ordered fraction in influenza lipids gradually decreases as function of temperature, for the X-31 strain. The authors also suggested that influenza lipids are not in a gel or solid state between 25 and 37 °C. The bending rigidity of gel phase lipids is in the 100-1000 kT range (i.e $K_b \approx 10^{-18}$ J) (171, 173), which is much higher than the values we found. This argues in favor of the absence of a major phase transition for those lipids, in the case of the PR8 strain, and goes against previous assumption that influenza virions select solid phase lipids (109).

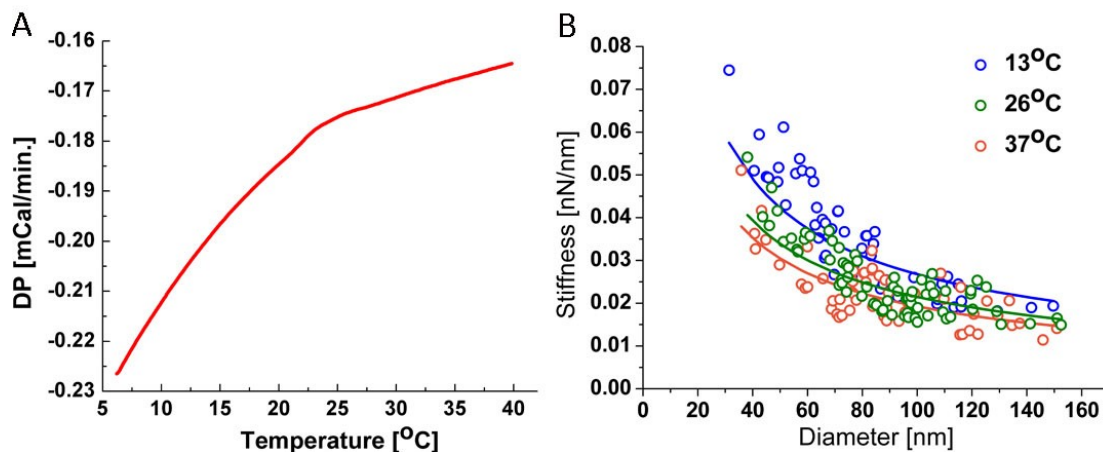


Fig 2.3.7 (A) Determination of phase transition temperature of influenza PR8 lipid from DSC method. The heat flow over temperature plot was averaged from 3 independent measurements, no obvious peak was observed on influenza PR8 lipid. (B) Temperature influence on the stiffness of influenza liposomes. Influenza liposomes at 13 ± 2 °C (blue), 26 ± 2 °C (green) and 37 ± 1 °C (orange). After fitting the stiffness

distributions for each case by **equation (2.3.1)** (solid line), the average stiffness for a 100 nm diameter vesicle was calculated. Influenza liposomes at 13 °C and 26 °C were on average respectively 47 % and 18 % stiffer than at 37 °C.

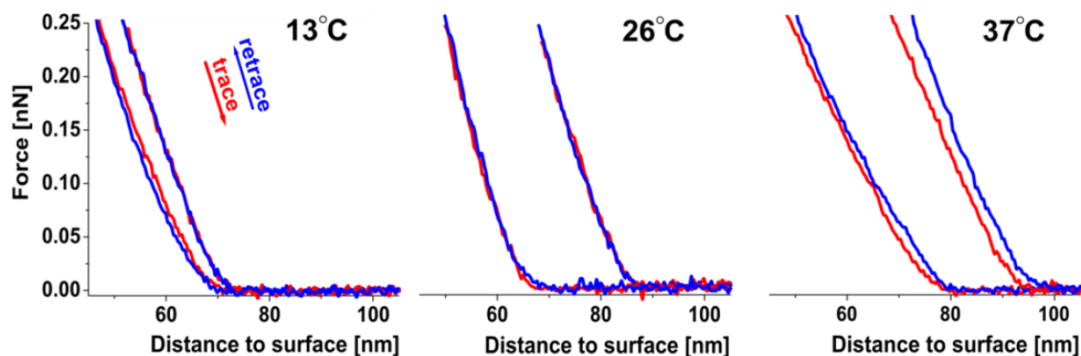


Fig 2.3.8 We compared the indentation curves obtained for Influenza liposomes at 13, 26 and 37 °C after pushing (trace) and retraction (retrace) of the cantilever. Shown are 6 example curves of trace and retrace from single particles between 40 and 100 nm that present no discontinuities: The deformation was fully reversible without hysteresis in the 0-0.25 nN range, thus elastic, as expected for a fluid phase bilayer. Each curve is the average of up to 4 curves that were obtained on top of a single particle (see also Materials and methods).

We defined our standard stiffness as the slope of a linear fit of the force vs. indentation curves between 0.1 and 0.2 nN. One may argue that the resulting deformation of $\approx 20\%$ at 0.2 nN is large for such small, highly curved liposome, since protein-based shells of similar dimensions show non-elastic responses from 15% deformations on (25, 174). In order to see whether SUV show consistent elastic behavior in the 0-0.2 nN range, we repeated our analysis in the 0.025-0.075 nN range and compared this to the results obtained between 0.1-0.2 nN: As a result we obtained an identical qualitative response when comparing the influenza liposomes at different temperatures (**Fig 2.3.9**), and after applying the FEM model, the Young's moduli agreed within 15% (**Table 3**).

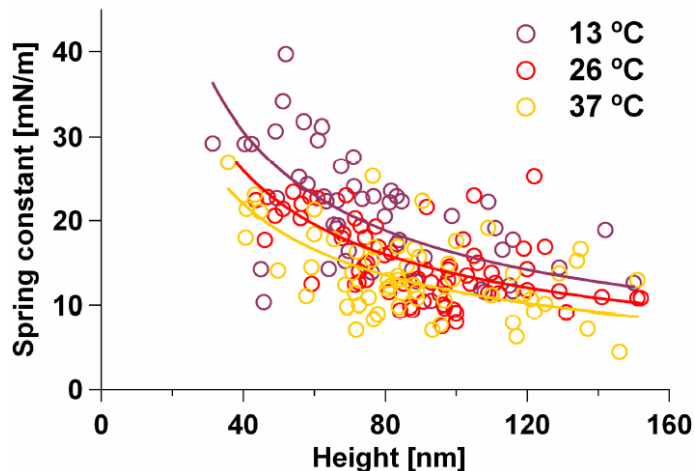


Fig 2.3.9 Another way to verify the elasticity of SUV is to compare the response of liposomes in two different force ranges. Therefore we determined the stiffness of the same influenza SUV data set by fitting the force curves between 0.025-0.075 nN with a linear function, and compared the response at this low force to that obtained in the 0.1-0.2 nN range. Although the spread in the data is larger than when analyzed with the high force fit (0.1-0.2 nN, **Fig 2.3.7**), the difference between the three temperatures is still clear. The solid line shows the fit by **equation (2.2.2)**.

To study how much deformation will be exhibited by the liposomes indented by force, we have plotted the magnitude of deformation of influenza liposomes in histogram for maximum force of 0.075 and 0.2 nN (**Fig 2.3.10, Table 4**). Clearly, the average deformation was less than 20 % of the liposome diameter.

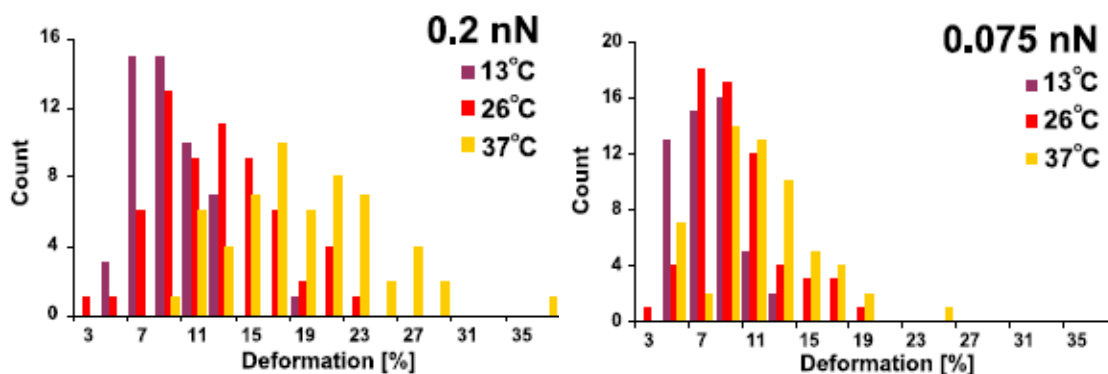


Fig 2.3.10 Deformation of influenza liposome (as % of the vesicle height) at 0.2 nN (left) and 0.075 nN (right). The 0.2 nN limit was used for the “high” force analysis of the data as described in the report, the lower limit of 0.075 nN was used for the alternative “low” force analysis.

Table 3: To test whether the response is also quantitatively identical at low and high force analysis, we calculated the Young's moduli obtained from the fits at low force (from **Fig 2.3.9**) and compared these values with those presented in the main report. The differences between the three temperatures remain clear, the absolute values agree within 15 %.

	0.025-0.075 nN fit	0.1-0.2 nN fit
13 °C	59 MPa	68 MPa
26 °C	45 MPa	45 MPa
37 °C	35 MPa	37 MPa

Table 4: The indentation of influenza particles at the maximum forces used for the low- and high force analysis. At 0.2 nN force the average deformations were up to 19 % of the liposome diameter. At 0.075 nN the average deformations were up to 11 % of the liposome diameter and the average indentation depths were 6-10 nm. At the same force the indentation depth was 5.9 nm on average and always less than 9.7 nm for particles < 50 nm.

Indentation/SUV	indentation at 0.75nN (av.±s.e nm)	indentation at 0.20nN (av.±s.e nm)
Influenza 13°C	5.9±0.2 nm (7.8±0.3)	10.3±0.4nm (13.4±0.4)
Influenza 26°C	7.9±0.3nm (9.5±0.4)	13.9±0.4nm (16.4±0.5)
Influenza 37°C	9.8±0.6nm (11.3±0.5)	16.3±0.8nm (19±0.7)

-pH

As the inactivation of influenza virus by acid requires treatment at pH<2 (175), we tested the stiffness of liposomes made from A/Japan influenza viral lipid at neutral and acidic pH. First the liposomes were tested at neutral pH (pH 7.4), and then at pH 5, at which the influenza virus is known to fuse with the endosome and releases the genome. The stiffness (Table 6) remains the same for both conditions. To verify if the stability of the stiffness is sustainable, the liposomes were first incubated at pH 5, and then neutralized to pH 7. The stiffness only reduces only by 5% (**Fig 2.3.11 A** and **Table 2**).

The Zeta potential describes the electrokinetic potential difference between the stationary layer of fluid which is attached to the dispersed particles and the dispersion medium. It is known as an important parameter which characterizes the mechanical stability of the liposomes (176). To further verify the stability of A/Japan liposome, we have measured its zeta potential from pH 3.6 to pH 7.6 at interval of 1.

All the values are in the range of -55 to -70 mV (**Fig 2.3.11 B**). Both the stiffness and zeta potential tests showed that the influenza viral lipid exhibits great stability when subjected to at acidic pH.

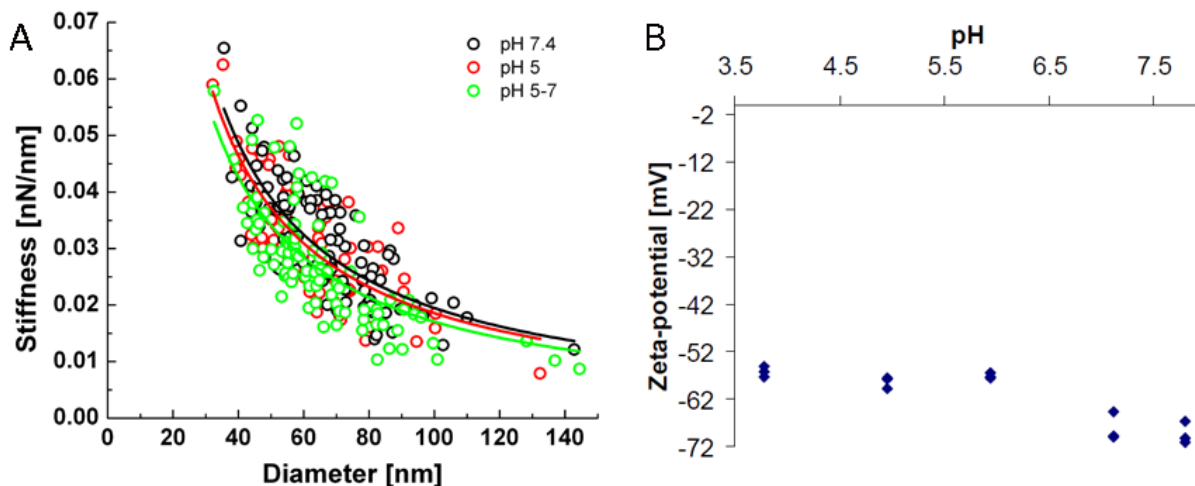


Fig 2.3.11 Stability of influenza lipid envelope tested at acidic pH. (A) Stiffness vs. diameter plot of liposomes made from influenza A/Japan viral lipid at neutral (Black), acidic pH (red) and neutralization condition (green). The plot is fitted with **equation (2.3.1)**, the stiffness at 100 nm gives the average stiffness of each species. No obvious difference was observed. (B) Zetasizer measurements showed that liposomes had a significant negative potential, consistent with the presence of phosphatidylserine in the influenza bilayer. No drastic effect of pH on the value or sign of the potential could be observed in the investigated pH range, consistent with an observed $pK_a < 3$ or > 8 for highly concentrated phosphatidylserine layers (177) (The composition of egg-purified PR8 influenza liposomes is described in section 2.2, one expects phosphatidylserine to be concentrated on the cytosolic side of the plasma- and viral membrane (178)). This is consistent with the absence of any charge change of lipids in the pH range we investigated.

-Puncture

Although liposomes made out of viral lipids are stiffer than DMPC ones (**Fig 2.3.4**) and approach the stiffness of the influenza virus itself (≈ 0.03 nN/nm at 27°C), they are still an order of magnitude softer than viruses protected by a protein shell (≈ 0.3 nN/nm) (179). To investigate how well the lipid envelope itself is capable of protecting its contents, we determined the force required for the tip to puncture the lipid bilayer. For that specific purpose single indentation experiments were performed by applying ≈ 2 nN pushes on top of influenza liposomes. Sudden slope changes (often negative ones) were frequently (but not systematically) observed in the vertical part of the force-indentation curves (**Fig 2.3.12 A**): We

attributed those slope changes to puncture the bilayer. 53 % of those puncturing events occurred when the tip was < 10 nm away from the surface, which approximately corresponds to the height of two lipid bilayers (**Fig 2.3.12 A inset**). In addition, the added length of all puncture events was on average 9.3 nm (not shown), which again matches very well the expected height of two superimposed lipid membranes. In almost every case, the slope of FZ curves after the last puncture was equal to that of an FZ curve performed on glass. Therefore puncture mostly occurred only after the tip forced the upper wall of the liposome in contact with the lower wall. The remaining 47 % of the puncturing events that occurred >10 nm away from the surface could be explained by: 1) A membrane expansion exceeding the stretching limit of lipid bilayers (about 2 % (108)) upon indentation. Our FEM model showed that at 50 % indentation the lipid bilayer of a 70 nm liposome stretches by 2 %. 2) Encapsulated vesicles, which would be fully collapsed at a 20 nm distance from the surface, and 3) Small lateral displacements of the particle during the push, leading to 'false' events. Puncturing events only occurred at forces higher than 0.4 nN (**Fig 2.3.12 B**) and the average force at which they were observed did not vary with increasing number of pushes. The average force required to generate jumps in FZ curves was 0.88 nN, taking all events into account: As mentioned above, some of those events may not be directly related to the tip penetration through the influenza envelope. When only the last puncture before contact of the tip with the substrate was considered, the average force leading to membrane puncture increased to 1.1 nN. This value is very similar to the rupture limit of some protein capsids (179).

Surprisingly, imaging and sizing of liposomes after multiple pushings and punctures showed that the liposome morphology did not change (shown in **Fig 2.3.12 C and D**). Such a self-healing behavior has been also observed to occur on a minute timescale for microtubules (174). Healing of a lipid bilayer may occur as fast as the indenter is raised, due to the liquid nature of the lipid leaflets. Inspection of the retrace showed other events with a sign opposite to the rupture event (not shown), which could be interpreted as the healing of the pierced bilayer upon retraction of the tip. Due to its softness and fluidity the influenza virus envelope could be elastically deformed wall-to-wall and healed from any puncturing in a subsecond timescale. Similar properties have only been reported for the CCMV capsid so far (180). In addition, we have shown here that the influenza lipid bilayer on its own constitutes a protective shell that resists rupture equally as well as a more rigid protein capsid.

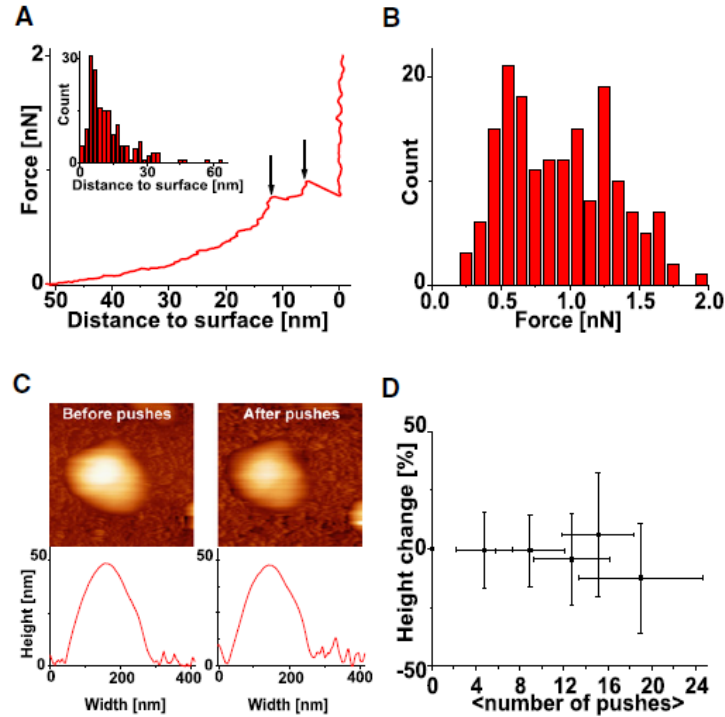


Fig 2.3.12 Influenza liposome rupture at high forces. (A) Jumps in the indentation curves occur at high forces: those are indicated by the black arrows (and identified by a change of sign of the slope). Inset: histogram of the distance to the surface for each puncture event (172 events on 19 particles). Most of the events occur at high indentation, e.g. when the tip is only separated from surface by the two apposed bilayers of the liposome. (B) The average puncturing force is 0.88 nN (172 events, 19 particles). > 95% puncture events occurred above 0.4 nN. (C) Pushing at high forces led to only minor morphology and height changes. Images and height profile show a liposome before (left) and after (right) 4 pushes at 2 nN force. (D) Multiple successive pushes at forces between 0.4 and 2 nN did not lead to a change in height (shown is the average of 12 experiments). On the abscissa the average number of pushes between each height measurement is indicated. The puncture experiments were performed at 28 ± 2 °C.

In addition, we show that > 95 % of puncturing of the influenza lipid bilayers occurred above 0.4 nN of applied force, further supporting our conclusion that the deformation of influenza SUV is reversible when the applied force does not exceed 0.2 nN. 4 % of the vesicles showed puncture events between 10 and 20 nm indentations (**Fig 2.3.13**): These 4% were vesicles of less than 55nm diameter and the punctures always occurred was at forces superior to 0.2 nN. This again argues in favor of the reversibility of FZ curves in the 0-0.2 nN range used for stiffness measurements.

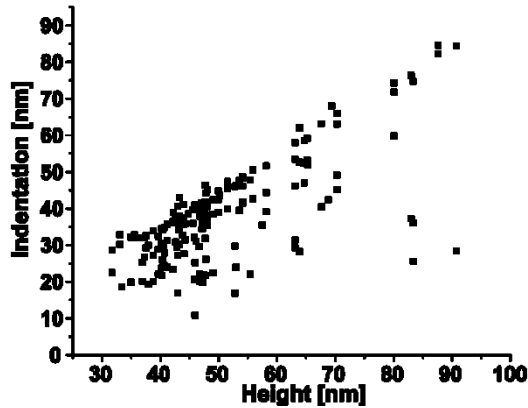


Fig 2.3.13 The indentation at which puncture occurred vs. the particle height. Most punctures occurred at a very high indentation and low distance to the surface. All punctures recorded at a 10-20 nm indentation occurred at forces above 0.2 nN.

-X-31 viruses in extreme conditions: Puncture and dehydration

Since the influenza liposomes were proved to be stable over various conditions as shown above, we were curious if the virus can survive from extreme conditions such as puncture and dehydration. Similar experiment was carried out directly on X-31 virus. 27 viral particles at neutral and acidic pH were first imaged and indented 5-10 times by high force (2-8 nN). 80% of the viral particles were punctured, which was reflected on the FZ curves. Immediately after puncture, the viral particles were imaged again. The height of the image was compared to the height before puncturing. The ratio of height (after)/ height (before), which is shown in **Fig 2.3.14**, indicates that the viral morphology did not change.

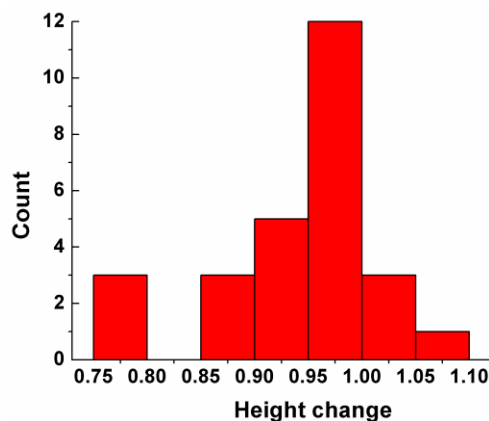


Fig 2.3.14 Influenza X-31 viral particles did not change in height after being indented with high force. 27 viral particles were tested (5-10 times, 2-8 nN), 80% of the viral particles were punctured. The height after indentation over height before indentation was plotted in the histogram.

Next, we tested the stiffness of X-31 after dehydration. X-31 viruses diluted in PBS at neutral pH were dropped on a cleaned glass substrate and placed in vacuum for 2 hours, during which time the liquid has evaporated completely and the buffer crystallized on the substrate surface. The dehydrated sample was then rehydrated by water to the previous buffer concentration. The stiffness vs. diameter plot was obtained by AFM and compared to that of the intact X-31 virus (Fig 2.3.15 B). Of the 17 viral particles measured, about 50% of them showed a similar stiffness to the intact ones. The morphology of some of the viruses remained unaffected by the dehydration (Fig 2.3.15 A). To verify if the imaged particles are no remains of the buffer crystals, PBS containing none viruses were dehydrated by the same procedure and tested by AFM. None particles were detectable.

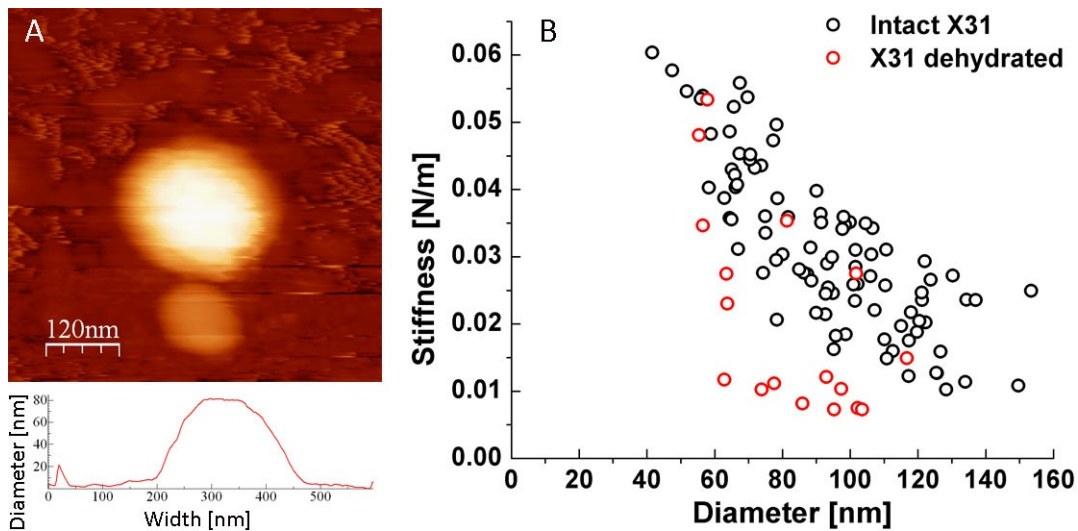


Fig 2.3.15 Part of the influenza viruses remain undamaged after dehydration. (A) A height image obtained in tapping mode showed an undamaged influenza X-31 viral particle. (B) The stiffness vs. diameter plot of X-31 dehydrated (red) was compared to that of the intact X-31 virus (black). About 50% of the particles showed a similar stiffness.

2.4. Discussion

One important prerequisite to unraveling the mechanical properties of the influenza lipid envelope was to assess AFM as a tool for quantitative studies of lipid bilayers, and to derive the obtained stiffness values so as to gain physically and biologically relevant information. AFM indentation experiments have been used to measure the stiffness of lipid-based bio-containers such as synaptic and endocytosis vesicles (166, 181). More recent studies were performed at higher imaging and indentation forces which led to severely deformed and non-spherical liposomes (118, 182).

In those studies, moreover, the Hertz model was applied, which led to a severe underestimation of the Young's modulus as the liposomes were assumed to be massive rather than hollow spheres. In our hands, obtaining consistent stiffness vs. diameter plots required measuring forces below 0.3 nN and discarding SUV that showed an aberrant aspect ratio. Occasionally liposomes were found to be non-spherical, elongated, disk-shaped or flattened. Non-spherical liposomes can originate from the liposome extrusion process (183), excessive interaction with the surface, or forces applied during imaging. The height measured from force maps acquired with forces between 0.1 and 0.3 nN or from tapping mode images of the same particles showed no systematic differences. Also the studied vesicles were close to spherical and easily displaced by scanning, one can infer that they were only weakly adsorbed on the DETA surfaces. The stiffness of the investigated liposomes was determined by linear fitting of force vs. indentation curves between 0.1 and 0.2 nN. In this force range, the deformation is expected to be elastic as force curves are fully reversible (**Fig 2.3.8**). In addition steps in FZ curves were only observed at an average force of 1.1 nN, indicating that no damage was done on the bilayer below that force.

As introduced in Chapter 1.2.3, the stiffness of liposome is largely determined by 1) existence of cholesterol and membrane proteins, 2) phase which is affected by temperature, 3) its lipid composition: Whereas long, saturated lipids as well as cholesterol enhance the organization of the bilayer structure. Before studying the liposomes made from influenza viral lipid mixtures, validation of AFM and our model as tools for the study of the lipid bilayers was gained from the quantitative determination of the effect of cholesterol on the stiffness of DMPC membranes. DMPC was chosen due to the abundance of data described in the literature on the mechanical properties of this lipid (108). The known properties of DMPC in fluid phase were accurately reproduced with our model. When the cholesterol was incorporated into DMPC liposomes (1:1 mol/mol), the observed stiffness increased by 100%.

To convert the measured stiffness values into parameters that are commonly used to describe membrane mechanics, K_a and K_b , we have created a FEM model that included the increasing contact areas between the planar surface, the liposome and the indenting AFM tip (**Fig 1.3.8 C**). The calculated values for K_a and K_b are in very good agreement with those previously obtained by micropipette suction (K_b around 10 kT, $\approx 0.4 \cdot 10^{-19}$ J for DMPC in fluid phase and 30 kT for DMPC:cholesterol 2:1) (184). In particular the bending rigidity K_b was around 20 kT, which is far lower than the value that was previously determined for DMPC GUV in gel state (173). We also showed that, no obvious difference in stiffness was observed on DOPC liposomes (phase transition temperature -20°C) at 13°C and 31°C . However, in case of phase transition, the mechanical properties would show a much larger difference (171).

By assessing the mechanical properties of liposomes made of virus lipids, we found that they are ~100% stiffer than the DMPC liposomes, and are almost as stiff as the DMPC+chol. 1:1 (mol) liposomes. The difference in stiffness is largely contributed by the proportion of cholesterol in the liposomes, as the proportion of cholesterol in the influenza liposomes (~43%) is comparable to that of the DMPC+chol. 1:1 (mol) liposomes (50%). The reason for studying a high cholesterol/lipid ratio comes from the fact that, due to its budding site the virus itself has a comparable amount of sterols in its envelope (see Materials and methods). In addition these methods could become a relatively simple tool to characterize the K_b of lipid bilayers of unknown or complex lipid composition. The lipids have to be extruded into liposomes, meaning that the natural in/out asymmetry encountered in cellular systems will not be recovered. However, as we expect the mechanical properties of lipids to be dominated by their hydrocarbon chains, this pitfall should be a minor one. In addition mechanical properties of natural small lipid assemblies, including other enveloped viruses, can be studied. Because the measurements are performed in liquid, conditions (pH) can be changed during the experiment, which would for example allow studying the relation between stiffness and rupture limits of a vesicle, and fusion with its target membrane.

The average stiffness $k_{100} = 0.021 \pm 0.0007$ nN/nm is only moderately less than what we found for the shell of X-31 influenza virions (including the M1 protein matrix) (≈ 0.03 nN/nm). This confirms the hypothesis that the M1 matrix protein plays a limited role in the stability of the influenza virus (29). Other enveloped viruses (HIV, MLV, Herpes) that have been tested with AFM show stiffnesses around 0.3 nN/nm, all dominated by their internal protein capsids (22, 26, 185). To show whether the envelope provides sufficient stability to protect the viral genome, we tested its mechanical properties at different environmental conditions.

The stiffness of influenza liposomes was somewhat higher than that of the DMPC: cholesterol vesicles implicating that the lipid phase of the virus envelope is of high stability. This raises the question of the phase state of virus bilayer. Indeed, the phase state of influenza lipids was controversial as the lipid composition of the envelope was thought to be forming a solid phase (109), although more recent reports suggests a mostly liquid phase over a wide range of temperatures (110, 186). For the temperatures tested here (13 to 37 °C) the envelope stiffness was only mildly affected by temperature, showing no drastic transition. Instead our measurements clearly indicate a fluid state, in spite of a rich composition in saturated lipids: Would the influenza virus bilayer be in gel state, its stiffness might have been very high ($K_b \approx 10^{-18}$ J), and reversible deformation might have proven impossible (173): Previous AFM measurements on gel phase SUV confirm that in the context of highly curved liposomes, E and K_b remain in the range measured with larger vesicles (171). So in spite of their saturated lipid composition, influenza lipid bilayers are rather soft and flexible, which may be a consequence of the high cholesterol concentration preventing the formation of a gel phase. The maintenance of a liquid state over a wide range of temperatures may be of particular interest as it may facilitate the virus with self-repairing properties, as we have shown for the isolated lipid envelope. To test if the mechanical properties of the lipid bilayer can be affected by low pH, we repeated the experiments on liposomes that were formed from viral lipids at acidic pH. Their stiffness remained almost identical at the all tested pH values (**Table 2, Fig 2.3.11**), from which we conclude that the mechanical properties of the lipid bilayer is independent of the low pH.

When the SUV envelope does rupture it does so at a force around 1 nN, which brings it in the same range as that obtained for protein capsids (25, 154). The efficiency of a biological shell in protecting its contents against chemical attacks may be best described by its fracture limits rather than its stiffness alone. Moreover the rapid healing properties of lipid bilayers, conferred by the instability of water-exposed bilayer pores (187), may make the protection against the external environment particularly efficient. However the relative softness of lipid bilayers might on the other hand represent a weak protective strategy against mechanical attacks. That said, the considerable void volume of influenza virions may allow the viral genome to remain unaffected while virions are deformed within the elastic limits known for protein shells. Meanwhile, we have also measured the stiffness of X-31 after dehydration. Of the 17 viral particles measured, about 50% of them showed a similar stiffness to the intact ones. The morphology of some of the viruses remained unaffected by the dehydration.

Those remarkable observations suggest that the bilayer by itself is sufficient to ensure the stability of the virus and to protect the viral genome under various environmental conditions. In addition one wonders if the M1 matrix protein, whose role is not yet clearly established (58, 188), is required to increase the stiffness of influenza virions with the purpose of making them more resistant to mechanical stress. From our results we could infer that the major function of M1 is different from providing a stable shell to the influenza virus. Indeed, M1 is more likely the key organizer of virus assembly that recruits locally the different viral components, excludes components of the host cell and drives the bending of the membrane leading eventually to influenza virus budding.

3. MECHANICS OF THE INFLUENZA A VIRUS

3.1. Introduction to the experiments

In the previous chapter it was shown that 70% of the influenza viral stiffness could be attributed to its lipid envelope. In this chapter, we focused on the other components of the viral structure. As was mentioned, the viral unpacking at fusion pH ($\text{pH} \sim 5$) is well studied; however, the preparation steps for the viral M1 and lipid envelope unpacking of the premature acidic pH ($\text{pH} \sim 5.5-6$) are still unclear. Around pH 6 ($\text{pH} \sim 6-6.5$), the M2 ion channel protein of the virus opens up (49), which leads to acidification of the viral interior. We showed that at $\text{pH} \sim 6$, the M1 capsids become weaker. As a matrix between the vRNPs and the viral membrane, the weakening of M1 will initialize the dissociation of these interactions, preparing the vRNPs to enter the cell nucleus (56). When the early endosomes mature into late endosomes, in which the environment is more acidic ($\sim \text{pH} 5-6$), the fusion between the viral and endosomal membrane will be triggered. The thickness of the M1 layer (~ 3 nm) makes the direct observation of the M1 matrix very difficult in EM. For example, it was suggested that M1 is still intact and serves as a foundation for the HA fusion activities at pH 5.5 (99), however this is questioned by our observation. Even if M1 could be clearly resolved, the visual impression itself may not be enough to show the gradual weakening of the M1 layer at different pH.

AFM provided us a way to fill this gap by measuring the elasticity of the complex. Any weakening of the M1 dimer-dimer interactions may be reflected by a decrease in stiffness. In this chapter, we explored the unpacking of influenza virus at acidic pH, focusing on the intermediate process in sub-acidic pH. The stiffness of intact and bald (without spike proteins) influenza X-31 virus was obtained at pH 5, 5.5, 6 and 7.4, and at neutralization after pre-incubation at pH 5, 5.5 and 6. Those conditions mimic the acidic milieu of early and late endosomes, which are essential pathways for influenza virus infection as described in section 1.1.2. At pH 6, the stiffness of the bald X-31 viral particles reduces by 15%, however, the softening is reversible after neutralization. At pH 5.5 and 5, the stiffness reduces by 30% and is irreversible after neutralization. However, the softening is not observed on liposomes made from viral lipid. The mechanical measurements are correlated to the unpacking of influenza A virus in early and late endosomes, and show that the gradual acidification that the virus undergoes in the endosomal pathway is essential for the complete unpacking of the virus.

This work was performed in collaboration with the group of Prof. A. Herrmann from the Humboldt University in Berlin. The AFM measurements were performed by me. The virus purification, biochemical and EM experiments were performed in Berlin. The content of this chapter is in preparation for publication.

3.2. Materials and methods

Sample preparation

Influenza A X-31 (H3N2) virus was propagated for 48 h in 11-day-old chicken eggs. The allantoic fluid was collected and cleared from cell debris by low speed centrifugation at 3000 g for 30 min. Then the virus was pelleted by ultracentrifugation 100.000 g for 90 min. The virus pellet was resuspended in PBS and homogenized with a Teflon-coated homogenizer. At last the total protein content was determined by BCS assay and the virus was stored in aliquots at -80 °C. Influenza A/Panama/99 was prepared in the madin-darby canine kidney (MDCK) cells. Cells were infected at an MOI of 1-3 in DMEM supplemented with 0.2 % BSA and 4 µg/ml TPCK trypsin. After 48h the virus was harvested as described above.

All AFM experiments were carried out in PBS. The pH of the sample was adjusted by adding sodium citrate to PBS until the pH reached the desired value, and the virus stock (1mg/ml) in PBS was 500x diluted in this buffer and kept at least 30 minutes at room temperature before the AFM analysis. To test the reversibility of the incubation of viruses at low pH, viruses were first incubated in acidic buffers at 37°C for 20 minutes and brought back to pH 7 by diluting them in large amounts of PBS.

Information about **Surface chemistry, AFM and cantilevers, imaging and force mapping** are available in Section 2.2.

HA conformational change and fusion assay

HA conformational change was monitored at 37°C using the environment-sensitive fluorophore bis-ANS (Invitrogen), its quantum yield decreases upon water exposure (189). Fusion was measured by monitoring the fluorescence dequenching (FDQ) of the lipid-like fluorophore R18 (Invitrogen) upon fusion of R18-labeled viruses with ghost membranes. For this labeled virus suspension (10 µl) was mixed with ghost suspension (40 µl) and incubated for 20 min at RT. Unbound virus was removed by centrifugation (5 min, 1200 g). The virus-ghost suspension was transferred to a glass cuvette containing prewarmed sodium acetate buffer, and the fluorescence was detected ($\lambda_{\text{ex}} = 560 \text{ nm}$; $\lambda_{\text{em}} = 590 \text{ nm}$) by using a Horiba Yobin Yvon FluoroMax spectrofluorometer. Fusion was triggered by the addition of citric acid. The suspension was stirred continuously with a 2 by 8 mm Teflon-coated magnetic stir bar. After 600 s the fusion was stopped by adding Triton X-100 (50 µl, final 0.5%) to obtain the maximum R18 fluorescence.

Bromelain digestion of intact X-31 viruses

Removal of the HA ectodomain was performed by Bromelain digestion (190). To this end 10 mg virus were incubated with 12.5 mg Bromelain (Sigma) in TE buffer for 16 h at 37 °C. The virus cores were pelleted by ultracentrifugation (100.000g, 2h), washed in PBS and stored at 4 °C.

Cryo-electron microscopy

Influenza A/X-31 stock was diluted in PBS with pre-adjusted pH, and incubated for 30 min. Sample droplets were applied to perforated (1 µm hole diameter) carbon film-covered 200 mesh grids (R1/4 batch of Quantifoil, MicroTools GmbH, Jena, Germany), which had been hydrophilized before use by 60 s plasma treatment at 8 W in a BALTEC MED 020 device. The supernatant fluid was removed with a filter paper until an ultrathin layer of the sample solution was obtained spanning the holes of the carbon film. The samples were immediately vitrified by propelling the grids into liquid ethane at its freezing point (90 K) and operating a guillotine-like plunging device. The vitrified samples were subsequently transferred under liquid nitrogen into a Philips CM12 transmission electron microscope (FEI, Oregon) using a Gatan (Gatan, Inc., California) cryo-holder and stage (model 626). Microscopy was carried out at a 94 K sample temperature using the low-dose protocol of the microscope at a primary magnification of 58,300 and an accelerating voltage of 100 kV (LaB6-illumination). The defocus was set to 1.2 µm.

Acid by-pass and immunostaining

MDCK cells were seeded in 12-well plates on 15 mm glass cover slips one day prior to the experiment. Influenza A/99/Panama (H3N2) was diluted in the phosphate buffered saline (PBS) to concentration of 50 µg/ml. The virus was pre-incubated in PBS at the indicated pH with or without 10 µM amantadine. The cells were washed in PBS and the virus was added and incubated for 10 min on ice. Afterwards the cells were washed and virus fusion with the plasma membrane was triggered by adding fusion buffer (10 mM HEPES, 10 mM MES in PBS, pH 5) at 37 °C for 5 min. The cells were washed again and incubated in DMEM for another 30 min at 37 °C. Subsequently the cells were washed 3x in PBS and fixed (2%PFA, 0.02 % GA in PBS) for 30 min at RT. The cells were washed twice in PBS and permeabilized for 20 - 25 min with PBS containing 0.5% Triton X-100 and 0.2% BSA. Primary antibodies against viral M1 (Virostat) and NP-FITC (Millipore) were diluted 1:1000 in PBS supplemented with 0.2% BSA and the cells were labeled for 1 h. The cells were washed in PBS 3 x10 min and incubated with the secondary antibody (anti-goat Cy3, Sigma) for 1 h. The cells were counterstained with DAPI at a final concentration of 0.2 µg/ml and finally washed 3 x 10 min. Glass cover slips were mounted on microscopy using Mowiol and stored in the dark after drying at 4 °C.

3.3. Results

3.3.1. Morphology of influenza viruses

Before studying the activities of the influenza viruses, we imaged them using two different microscopy methods to obtain information of their basic morphology. First, we used cryo-EM to image X-31 viruses at neutral pH with different magnification. They exhibit both spherical and elongated morphologies, as is shown in **Fig 3.3.1 (A)** and **(B)**. Similar images were observed by AFM, exhibiting both spherical and elongated morphologies, as is shown in **Fig 3.3.1 (E)**, **(F)** and **(G)**. To be able to exclude the effect of morphology to the mechanical properties, we only used spherical shape viruses for mechanical measurement, which will be discussed in the next sections.

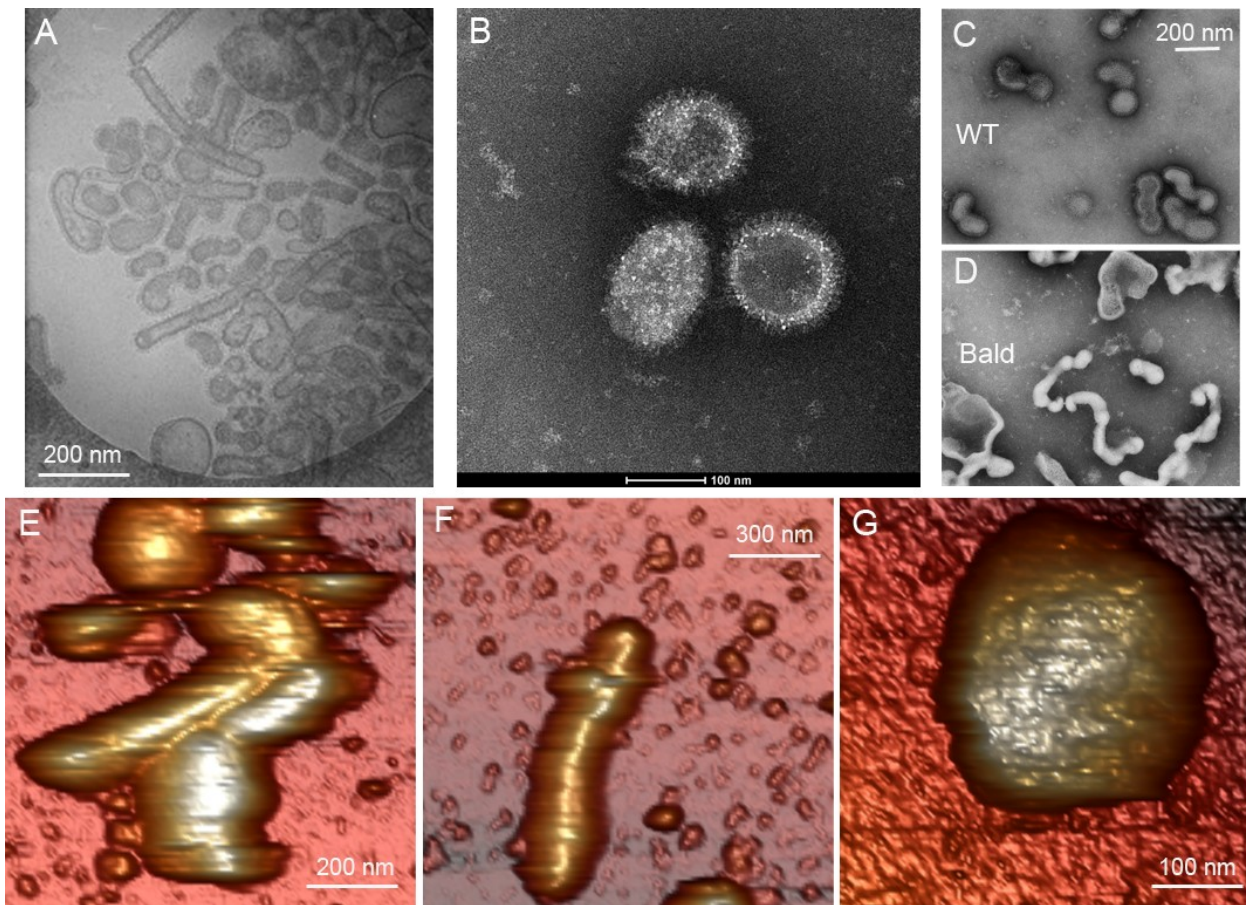


Fig 3.3.1 Morphology of the influenza A/X-31 viruses imaged by cryo-EM (A-D) and AFM (E-G). (A) The X-31 viruses were imaged at neutral pH with a magnification of 60,000 times. (B) The X-31 viruses were imaged at neutral pH with a magnification of 80,000 times. (C) Wild-type (WT) X-31 viruses and (D) bromelain-treated X-31 viruses were imaged for comparison. (E) A cluster of X-31 viruses and (F) a single

elongated X-31 virus incubated at pH 5 were imaged by AFM. (G) A single spherical X-31 virus incubated at neutral pH was imaged by AFM.

As will be shown in the next sections, we used bromelain-treated X-31 viruses as control experiments to exclude the possible contribution of spike proteins to the stiffness of the untreated viruses. We also imaged both the untreated and bromelain-treated X-31 viruses for comparison, as is shown in **Fig 3.3.1 (C) and (D)**. Samples of untreated or bromelain-treated influenza A virus were negatively stained with 1 % (w/v) phosphotungstic acid (PTA), pH 7.4. Bromelain treated yielded particles with a smooth surface, and devoid of the spikes observed at the surface of untreated virions.

3.3.2. pH-controlled unpacking of Influenza virus

Softening of influenza viruses at low pH

To be able to understand the structural changes of influenza viruses during its unpacking at low pH, we have measured the stiffness of influenza viruses at four pH values (7.4, 6, 5.5 and 5), which correspond to the pH values encountered at the cell periphery, early endosome and late endosome. Prior to the AFM experiments, the viral stock was diluted in a buffer adjusted to the desired pH. At pH 6 the stiffness of X-31 virions decreased by 26% with respect to pH 7.4, whereas at pH 5.5 and 5, the stiffness was 36% lower than at pH 7.4 (shown in **Fig 3.3.2 A and B, Table 5**).

To rule out the possibility that, the softening is contributed by the conformation of spike proteins at acidic pH, we performed the same experiment on spike protein-free X-31 viral particles. Removal of spike glycoproteins by bromelain digestion slightly attenuated the observed effect of pH on untreated viruses, but did not change the trend of stiffness decrease with pH. The stiffness of 'bald' (bromelain-treated) viruses decreased by 12% from pH 7.4 to pH 6, and by 25% from pH to 5.5 or 5 (shown in **Fig 3.3.2 C, D and Table 5**). This means that, the stiffness decrease of influenza virus at low pH is probably not caused by a conformational or ionization change of spike glycoproteins.

To verify that this effect is not due to the lipid bilayer itself, we performed the same experiment on liposomes made from the lipid of influenza A/Japan virus: viral lipids were purified from influenza virus A/Japan and extruded into liposomes. After incubation at pH 5 at room temperature for 20 minutes, the stiffness of the liposome was recorded (shown in **Fig 2.3.11 A**). No changes were observed in the stiffness of influenza liposomes between pH 7.5 and pH 5. Though the influenza liposomes are expected to bear an important density of negative charges, we did not identify any change in the electrostatic potential of those liposomes in the same pH range either (shown in **Fig 2.3.11 B**). Thus we conclude that the lipid bilayer does not contribute to the pH effect on viral stiffness.

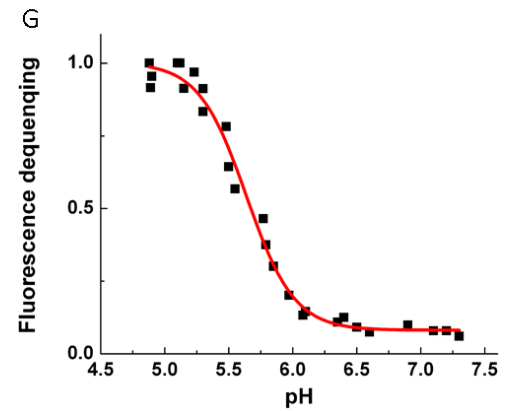
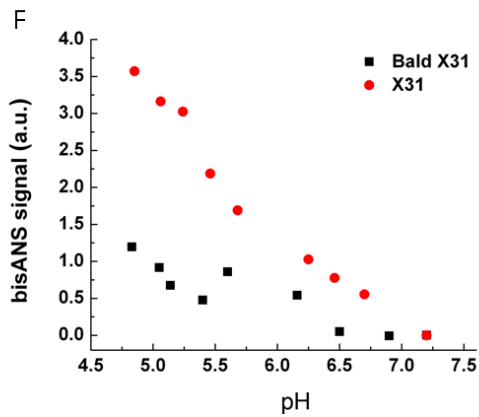
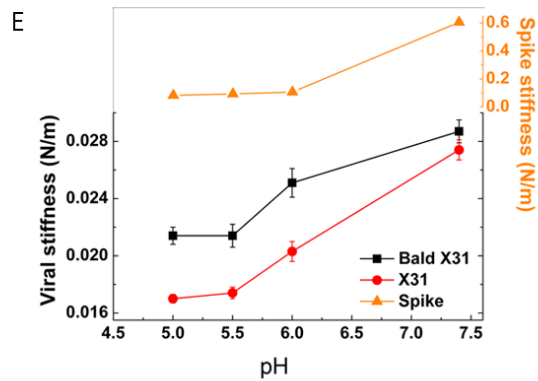
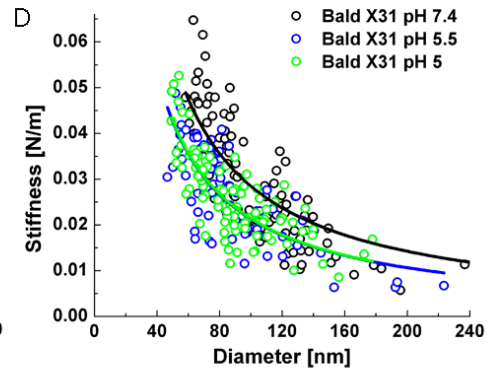
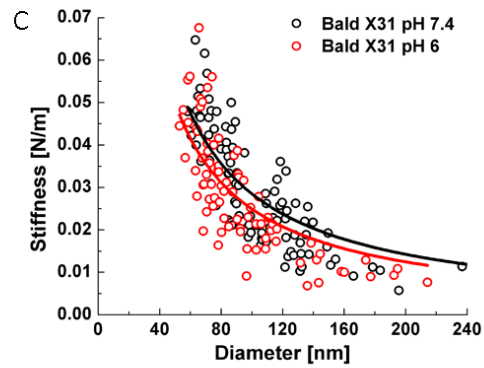
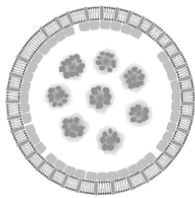
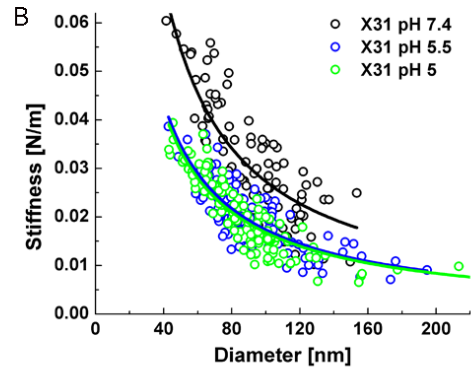
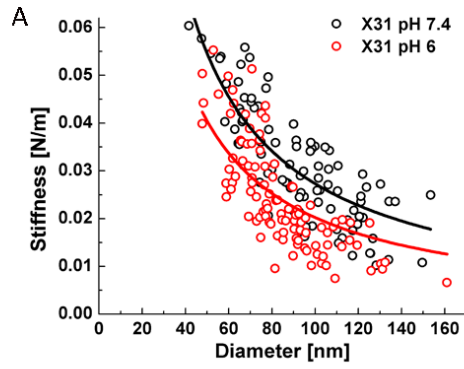
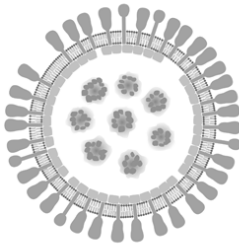


Fig 3.3.2 The two-step softening of the X-31 and bald X-31 viral particles at low pH values. (A) and (B): stiffness of X-31 viruses at pH 7.4 (black), 6 (red), 5.5 (blue) and 5 (green). (C) and (D): stiffness of bald X-31 viruses at pH 7.4 (black), 6 (red), 5.5 (blue) and 5 (green). The data were fitted by **equation (2.3.1)** (solid line). Two insets indicate the structural difference between the X-31 and bald X-31 viral particles. (E) The average stiffness of bald viruses (black) and untreated viruses (red) at different pH values. Each point represents the average stiffness at 100 nm of 67-106 single viruses. The untreated viruses are always softer than the bald ones, but the difference is not constant. This difference, caused by the contribution of the spikes, was quantified with **equation (3.3.1)** (orange). The spikes appear to soften between pH 7.4 and 6.0 and remain constantly soft at lower pH values. (F) The conformational change of HA monitored with the environment-sensitive fluorophore bis-ANS. The response of the bald virus is included as negative control. At pH values of above 6 the signal is small and the major conformational change occurs between pH 6 and 5. (G) The fusion of influenza A X-31 with ghost membranes as function of pH. Virus-cell fusion was measured by R18 de-quenching 10 minutes after the pH was lowered. Fusion only occurs at a pH of below 6. Figure B and C were obtained by C. Sieben at the HU Berlin.

The viral spike proteins have an effect on the measured stiffness (29). The spikes, consisting of HA and NA, form an additional layer between the AFM tip and viral shell (and of course also between the shell and the supporting surface). Therefore the spikes can be considered as a spring (k_{spike}) that is placed in series with the stiffness of the viral shell (k_{shell}). The total spring constant (k_{total}) is therefore expected to reduce when the spikes are present, following the standard behaviour of two springs that are connected in series:

$$\frac{1}{K_{total}} = \frac{1}{K_{spike}} + \frac{1}{K_{shell}} \quad (3.3.1)$$

To be able to separate the contribution from M1 and the viral spikes, we compared the stiffness of untreated viruses with viruses that had their spikes removed. **Fig 3.3.2 E** shows the average stiffness for 100 nm particles at the different conditions. At all pH values the bald viruses show a stiffness that is higher than that of the intact viruses. This is in agreement with that what is expected from **equation (3.3.1)** and shows that the presence of the spikes lowers the total spring constant of the intact virus. The effective spring constant of the spikes is given by the difference between the curves in **Fig 3.3.2 E** and can be estimated from **equation (3.3.1)** by using the intact virus values for k_{total} and the bald virus values for k_{shell} . Interestingly, this difference, shown in orange in **Fig 3.3.2 E**, is not constant but increases at lower pH values. This indicates that the spikes appear to soften between pH 7.4 and 6.0, and remain soft when the pH is further lowered down to 5.0.

It is tempting to attribute the observed softening to the pH induced conformational change of HA. HA forms ~85 % of all spikes (191). Upon pH lowering HA undergoes a large conformational change that leads to a disruption of non-covalent contacts between HA1 and HA2 subunits as well as to fusion

peptide exposure (78). To determine the pH range of the HA activity in our virus isolate, we monitored its conformational change by using the polarity-sensitive fluorophore bis-ANS: bis-ANS fluorescence significantly rose below pH 6, indicating that only then a major conformational change takes place **Fig 3.3.2 F**. It shows that, although there is some increase in fluorescence between pH 7 and 6, it rises only strongly between pH 6 and 5, indicating that only then the major conformational change takes place. In addition, we tested the functional activity of HA in a fusion assay between the viruses and red blood ghost cells. Fluorescence dequenching was used to follow fusion. **Fig 3.3.2 G** shows that fusion is absent above pH 6.0. Below pH 6.0, the fusion activity rose sharply following a sigmoidal trend, to reach a maximum at pH 5.0. Both the conformational change of HA and the HA induced fusion occurs mainly between pH 6.0 and 5.0, which is in full agreement with other studies of the HA pH dependent response (78, 192, 193). The apparent softening of the spikes we observe between pH 7.4 and 6.0 can therefore not be attributed to the conformational change of HA. Still, the phenomenon must be somehow related to the spikes, as we clearly observe a difference in pH response between the untreated and the bald viruses. The observed softening could be either an increased flexibility of the spikes or an increase in their mobility over the virus surface. Such an increased mobility would appear as an apparent softening as the spikes can then they can be more easily pushed aside by the AFM tip.

It is worth noting that besides the change of the stiffness contribution of the spikes between pH 7.4 and 6.0, also the bald viruses show a small but significant reduction in stiffness in this pH range ($p=0.005$). This change must originate from a pH induced change in the viral shell itself.

M1 disassembles between pH 6.0-5.5

The strongest stiffness decrease of the virus took place between pH 6.0 and 5.5 (**Fig 3.3.2**). The contribution of the spikes in that range is constant; hence it is most likely that this stiffness decrease signals the disassembly of the M1 layer. To verify this we collected electron microscopy images from the viruses at the different pH values. Though the M1 layer was present at pH 7.4 and 6.0 we could not resolve it anymore at pH 5.4 and 5.0 (**Fig 3.3.3**). Combined with our mechanical measurements this shows that the disassembly of the M1 layer takes place between pH 6.0 and 5.5. This observation is not fully consistent with other reports showing an intact M1 layer after 5 min incubation at pH 5.5 (99) and its sometimes incomplete dissociation after 5 min incubation at pH 4.9 (58). This discrepancy is likely explained by the longer exposure times to acidic pH (> 20 min.) in our conditions.

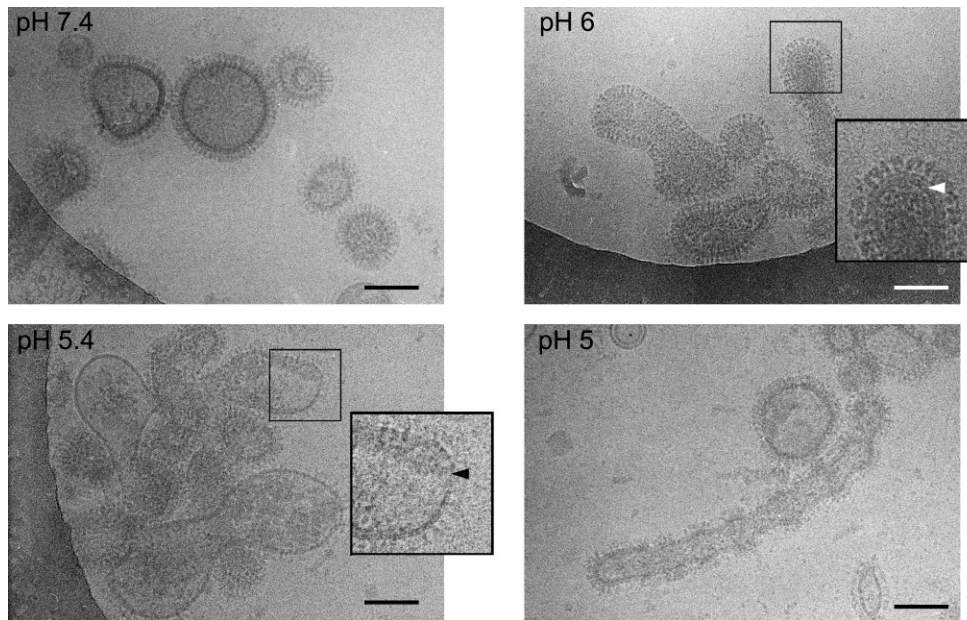


Fig 3.3.3 M1 layer disappears at low pH. Cryo-electron micrographs of influenza A/X-31 viruses imaged after being pre-incubated 30 minutes in pH 7.4, 6.0, 5.4 and 5.0. The viruses pre-incubated at pH 7.4 and 6.0 showed M1 layers underneath the lipid bilayer (marked with a white arrow in the enlarged detail); while the viruses pre-incubated at pH 5.4 and 5.0 showed no M1 layers. Scale bars correspond to 100 nm. The image was obtained by K. Ludwig at the FU Berlin.

Reversibility of the pH-dependent mechanical response

To test whether the changes within the virus are reversible we analyzed the stiffness of viruses incubated at low pH and brought back to pH 7. After preincubation at pH 5.5 and neutralization, both intact and bald viruses did not recover to the original stiffness. However, when preincubated at pH 6 and brought back to neutral pH, the measured stiffness was higher than that obtained at pH 6 without neutralization, and very close to the stiffness of the same bald viruses at pH 7.4 (shown in **Fig 3.3.4**, and **Table 5**).

Fig 3.3.4 E shows the results of our measurements on bald viruses. The relatively small amount of softening that is observed when the pH was lowered to 6.0 was largely reversed when the pH was brought back to 7.4. This reversible softening signals a change in the viral core, since the external parts of the spikes were removed for these experiments: However electron microscopy failed to show any M1 dissociation at this pH, and other viral components must therefore be incriminated in this reversible process. When the pH was lowered to 5.5 or less and then brought back to 7.4, the viral stiffness remained as low as before neutralization. Since we observed M1 dissociation at pH 5.5 and 5.0, our measurements indicate that the disassembly of the M1 layer is an irreversible process.

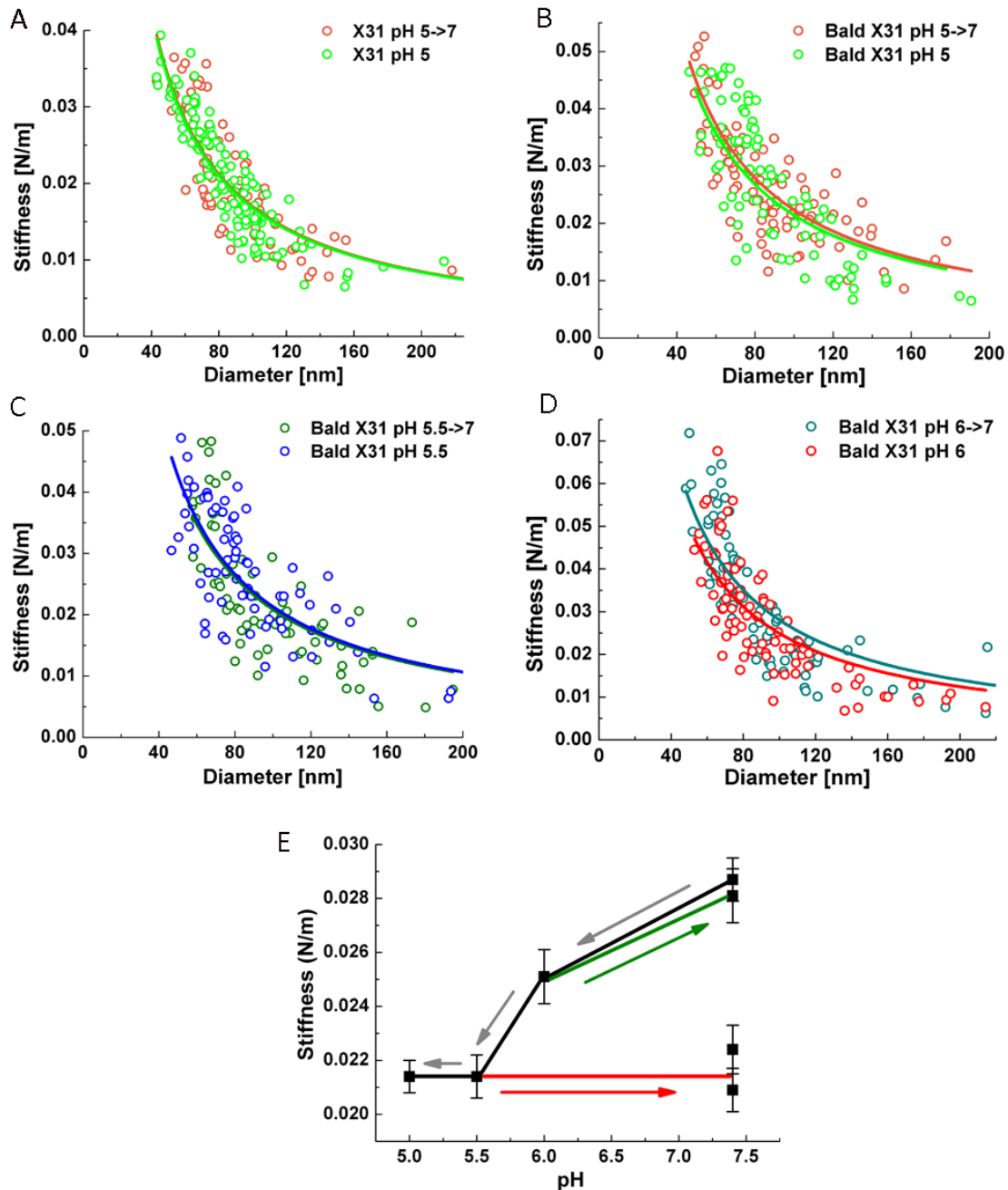


Fig 3.3.4 Stiffness comparison between X-31 and bald X-31 viral particles after pH neutralization. (A): stiffness of X-31 at pH 5 (green) and neutralized from pH 5 (orange). (B), (C) and (D): stiffness of bald X-31 viruses at pH 5 (green), 5.5 (blue), 6 (red) and after neutralization from pH 5 (orange), 5.5 (olive), 6 (cyan). The data were fitted by **equation (2.3.1)** (solid line). (E) The reversibility of the stiffness reduction of bald viruses at low pH. In general, the stiffness of bald influenza viruses decreases with pH (black line & grey arrows). After neutralizing the buffer from pH 6.0 to pH 7.4, the stiffness recovers (green line & arrow). However, after neutralizing the buffer from pH 5.0 or pH 5.5 to pH 7.4, the stiffness does not recover (red line & arrow). The M1 disassembly is an irreversible process.

Summarizing the above observations, our results showed a gradual softening of the influenza virus at low pH: Since the second step softening involved neither spike glycoproteins nor the influenza lipid bilayer, we investigated in the next section the consequences of the acidification of the viral lumen on the unpacking in the host cell of the influenza virus.

3.3.3. Both softening steps are required for complete virus disassembly

So far, we have found two distinctive pH-induced phases from the mechanical measurements:

1) pH 7.4→6.0, the stiffness of the spikes reduces, and we measured a small, reversible reduction in the stiffness of the viral core itself.

2) pH 6.0→5.5, the M1 layer disassembles irreversibly.

Since the two above-mentioned pH regions correspond to that encountered in early and late endosomes, it seemed important to assess how relevant those conditions are to viral infection. We did so by performing acid by-pass experiment (194): In this assay, fusion between the virus and the plasma membrane is triggered directly after adsorption of the virus, by flushing the sample with a low pH (5.0) buffer. Thus a prolonged exposure of the virus to intermediate pH (6.0-7.4) is avoided. Fusion with the plasma membrane simulates of the incubation the virus in the late endosomal compartments with no prior transit through the early endosomes.

Fig 3.3.5 A and B show via immuno-staining the cellular uptake of the M1 (red) and the NPs (green). The cell nuclei were stained by 4',6-diamidino-2-phenylindole (DAPI, blue). When fusion was triggered immediately without preincubation or preincubated at pH 7 for 30 min., M1 and NP co-localized, only low amount of NPs enter the nucleus. Next, we pre-incubated the sample at pH 6.0 for 30 min. prior to fusion, to simulate the transit of flu viruses in early endosomes. Under these conditions the M1 and NP form significant less clusters, and were now homogenously distributed through the cytosol, and NP also in the nucleus (**Fig 3.3.5 C**). The signal of M1 in the cytosol was quantified in **Fig 3.3.6**, which showed a clear increase when the virus is preincubated at pH 6.

A preincubation step at pH 6.0 is therefore important to avoid an aggregation of the viral M1 and NPs which will affects the release of the viral genome. Control experiments were performed in which the amantadine-sensitive A/Panama strain was incubated at pH 6.0, with or without amantadine: This was done to block the viral M2 channel, thus to prevent the acidification of the viral interior (**Fig 3.3.7**). This also resulted in the clustering of M1 and vRNPs. This indicates that pre-incubating influenza virus at pH 6.0 acts on the viral lumen. Clustering of M1 and NP was also observed when flu viruses were pre-incubated at pH 7.0, showing that the proper release of M1 and NP in the cell requires the incubation of viruses at mild acidic pH (**Fig 3.3.5 D**).

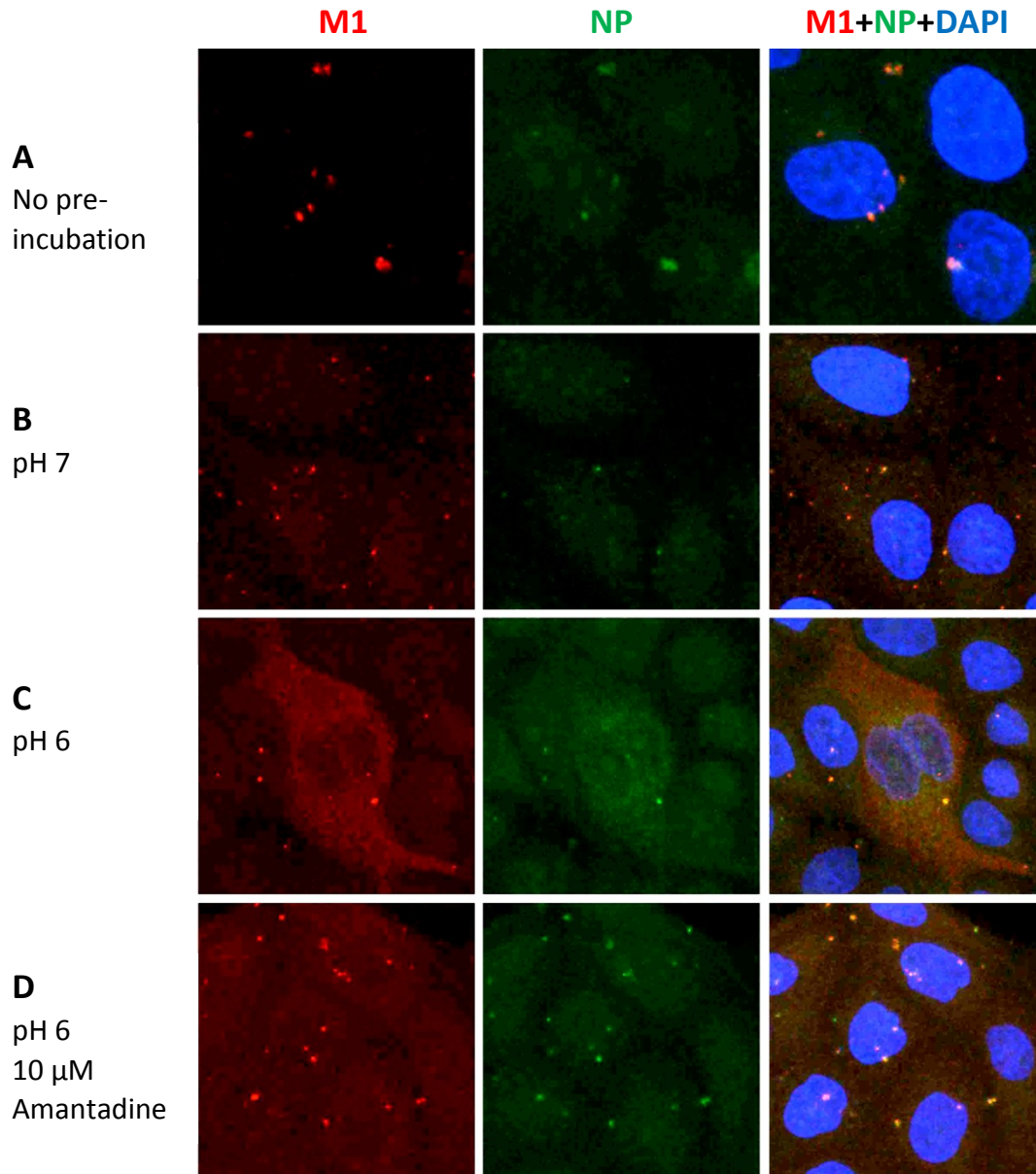


Fig 3.3.5 Acid induced fusion by-pass of influenza A/Panama with the plasma membrane of MDCK cells. Cells were incubated at the indicated conditions for 30 min. Fusion was induced by addition of fusion buffer at 37 °C for 5 min. The cells were then incubated for 30 min at 37 °C, fixed and immunostained for M1 and NP. The images show summed z-stacks though the whole cell. (A) No pre-incubation and (B) pre-incubation at neutral pH led to NP and M1 aggregation. (C) Free M1 and NP were observed after pre-incubation at pH 6. (D) 10 μM amantadine present during the pre-incubation and fusion steps was shown not affecting the entry of X-31 M1 and NP into the nuclei. The image was obtained by C. Sieben at the HU Berlin.

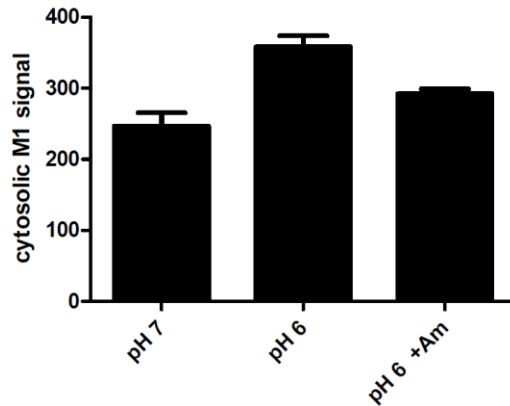


Fig 3.3.6 Quantification of cytosolic M1 after acid-induced fusion by-pass with the plasma membrane. M1 signal in the cytoplasm was measured with ImageJ from summed z-stacks (see Fig 3.3.5). Mean and SEM (n=5) of a Gaussian fitting from the pixel intensity distribution. The image was obtained by C. Sieben at the HU Berlin.

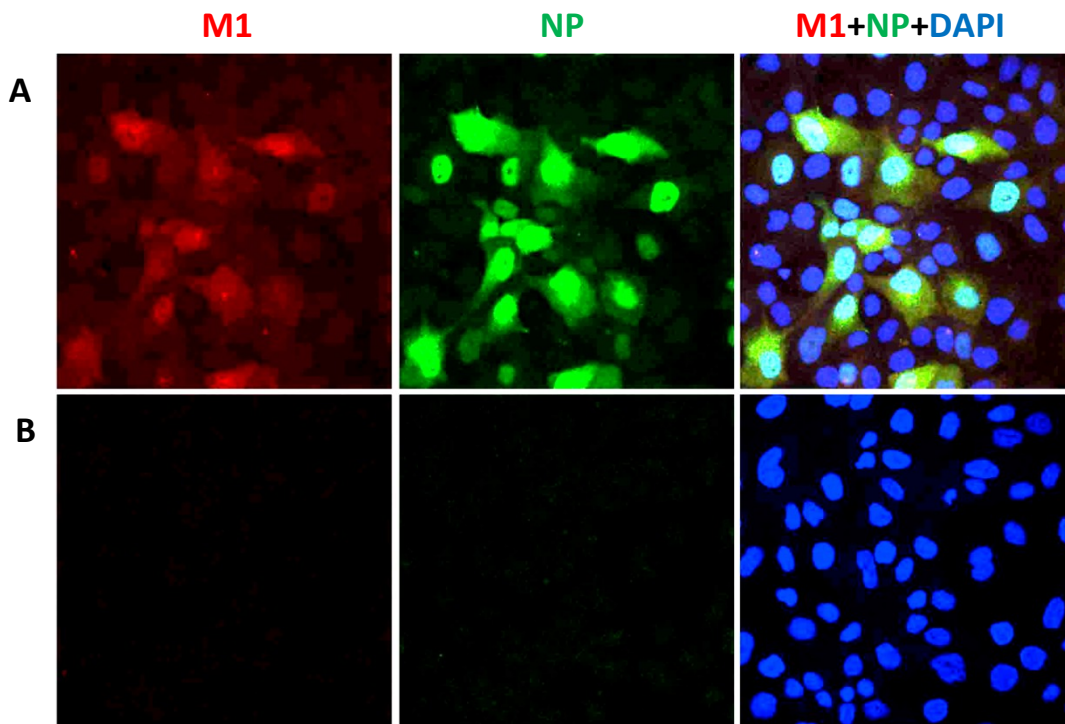


Fig 3.3.7 Amantadine inhibits influenza A/Panama/99 infection of MDCK cells. MDCK cells were infected with influenza A/Panama in the presence (B) and absence (A) of 10 μ M amantadine and incubated for 5h at 37 °C. Positive infection was visualized by immunostaining against viral NP. The image was obtained by C. Sieben at the HU Berlin.

Table 5: The average stiffness of influenza X-31 viruses at different conditions. The average stiffness is obtained by first fitting the stiffness by **equation (2.3.1)** and taking the value at $D=100$ nm. Below each stiffness value, the standard errors together with the number of independent particles tested were present. The standard errors were calculated by dividing the standard deviation by the number of particles. The standard deviation was calculated from the residuals of the fit.

K_{100} (N/m) and number of samples							
pH	7.4	6.0	5.5	5.0	6.0 → 7	5.5 → 7	5.0 → 7
A/X-31 virus	0.0274 ± 0.0009 (n=90)	0.0203 ± 0.0007 (n=102)	0.0174 ± 0.0004 (n=101)	0.0170 ± 0.0004 (n=106)	-	-	0.0171 ± 0.0005 (n=79)
Bald A/X-31 virus	0.0287 ± 0.0010 (n=89)	0.0251 ± 0.0012 (n=72)	0.0214 ± 0.0008 (n=68)	0.0214 ± 0.0006 (n=90)	0.0281 ± 0.0012 (n=74)	0.0209 ± 0.0009 (n=67)	0.0224 ± 0.0011 (n=78)

3.4. Discussion

With our results we showed that the unpacking of influenza virus at low pH occurs in at least two distinct steps that both resulted in a significant softening of the virions, indicating in each case structural changes in the virus. In addition a 'by-pass' cell-virus fusion assay showed that the genome release inside cells requires both the acidification of the lumen at pH 6.0 and membrane fusion at pH 5.0. We therefore shed light on a two-step mechanism for the unpacking of the flu virus genome.

At pH 6.0 the stiffness of flu virions decreased by 26 % (**Fig 3.3.4 E**). The stiffness of bald viruses decreased as well, though to a lower extent. The effect of incubating bald viruses at pH 6.0 was reversed after bringing the virus back to pH 7. Two contributions to the measured changes could therefore be identified: The most prominent effect came from spike glycoproteins and another smaller yet significant effect was attributed to a modification of the viral lumen. It is apparently difficult to reconcile our observation of a spike-dependent softening of the virus at pH 6.0 with the knowledge that influenza HA only undergoes its fusogenic conformational change at lower pH values (**Fig 3.3.2 G**). However two hypotheses explain our measurements:

- i) Although HA preserves its prefusion conformation in subacidic conditions, it was shown that its stability to thermal denaturation is considerably lowered (the difference of T_m at pH 7 and 6 was 7 degrees), indicating that its structure at pH 6 is far less compact than at neutral pH (192). Conformational states with low compactness such as the molten globule are expected to be more compliant (195).
- ii) A gain of mobility of HA may also account for this change. A wealth of experimental data supports the idea that an interaction exists between HA and M1 (188). Upon opening of M2 at pH 6 and partial protonation of M1, the HA-M1 interaction could be disrupted, leaving however the M1 layer and the HA conformation apparently intact.

In the second step, which occurred between pH 6.0 and 5.5 the stiffness decreased by 36 % compared to pH 7.4. A further lowering of the pH to 5.0 did not significantly soften viruses any more (**Fig 3.3.2 E**). This softening was not reversed by re-neutralization of the virus preparation. This, along with EM observations (**Fig 3.3.3**), showed us that the second step corresponded to an irreversible dissociation of M1 from the lipid envelope.

Although the origin of the second step seems thus clear, neither mechanical measurements, nor electron microscopy could help us identify the cause of the first, reversible step that occurred above pH 6.0: Electron microscopy of pH 6-incubated viruses did not show any significant M1 dissociation from the envelope. Therefore we must conclude that the acidification of the viral lumen at pH 6.0, triggered by the opening of the M2 proton channel, affects the organization of the interior of the virus in a way that could not be identified by AFM or cryo-electron microscopy. Along with a possible, yet unseen fragilization of the M1-M1 or M1-HA interaction, the dissociation of vRNP from the M1 could also contribute to the first step of viral unpacking: Biochemical characterizations showed that the C-terminal domain of M1 is able to bind the vRNP at neutral pH (196). M1-vRNP complexes may be isolated at

neutral pH but the complex dissociates at acidic pH (197). Moreover, whereas the association of M1 with vRNP in the cytoplasm inhibits their nuclear import, the latter process could be restored by acidifying the cytoplasm to pH 6, indicating that the pH of early endosome may be sufficient to disrupt the M1-vRNP interaction (52). Contacts are made by some of the eight vRNP rods with the M1 layer (90, 91). vRNP also contact the envelope at the budding front, though M1 is absent there: Such contacts may confine the flexibility of the shell, in a comparable way as DNA was found to reinforce viral protein capsids (20). The apparent absence of a preferential site on the M1 layer where vRNPs may bind could help to explain why the first observed phase was reversible (90, 196).

Whichever scenario may account for our observation of an influenza virus rearrangement at pH 6.0, bypass experiments provide evidence that this very step is essential to the viral infectivity. It seems that influenza virus needs to be somewhat 'primed' in the early endosome for it to properly release of the viral genome out of the late endosomes. Our data adds up to other evidence that influenza virus avoids exposing dissociated M1 proteins to its genome before the latter is released in the cytoplasm. Would the virus not pass early endosomes, M1 and vRNP would aggregate inside the virus, thus preventing the proper genome release. It is interesting that, contrary to influenza, other enveloped viruses such as the Semliki Forest Virus (SFV) or Vesicular Stomatitis Virus (VSV) are able to fuse with early endosome, and the pH of the fusogenic conformational changes of the E1 or G (pH 6.2-5.5) is adjusted to meet that requirement. In spite of this, it has been observed that VSV does not release its genome directly after membrane fusion, rather stores its nucleocapsid in the inner membrane of multivesicular bodies, until the latter fuses with the outer membrane of more acidic compartments, later during endosomal transport (198). This suggests that, for efficient targeting of the nucleus, such viruses as influenza or VSV must release their vRNPs assemblies at the stage of the pH 5 late endosomes, and not earlier.

Influenza may have evolved its components to make this targeting possible: The optimum pH of HA fusion activity seems to be adapted to permit fusion only after the viruses went through early endosomes (199). The pH at which the M1 layer dissociates lies within the pH range at which fusion occurs. Notably, electron microscopy shows that if viruses are subjected only to the acidic pH of late endosomes for a short time, a significant amount of M1 remains associated (58, 200) with the viral envelope while large amounts of HAs have undergone transconformation (193), therefore allowing membrane fusion. The kinetics of HA conformational change, M1 dissociation and genome release at low pH are therefore such that (i) sufficient patches of membrane are freed from the M1 layer, permitting HA to complete membrane fusion; (ii) *in vivo* viable influenza strains will efficiently release their genome before it can re-bind to M1 proteins. One can draw a simple kinetic scheme where the viral genome would transit from an inactive (i.e M1 trapped) to an "activated state" (i.e genome is detached from M1), which in turn would either be released from the virus (fusion) or inactivated (through aggregation with M1). To achieve efficient genome release the rates of genome "activation" and fusion must be faster than that of aggregation. If, on the contrary, fusion would occur before the genome was released as proposed earlier (52), then M1 dissociation could immediately lead to genome inactivation (**Fig 3.4.1**). We propose that the influenza virus tunes these rates by pH, in a fashion that is optimally adapted to the virus journey through the different endosomal stages. This scheme facilitates a sequential unpacking of the virus, of which we have identified two steps.

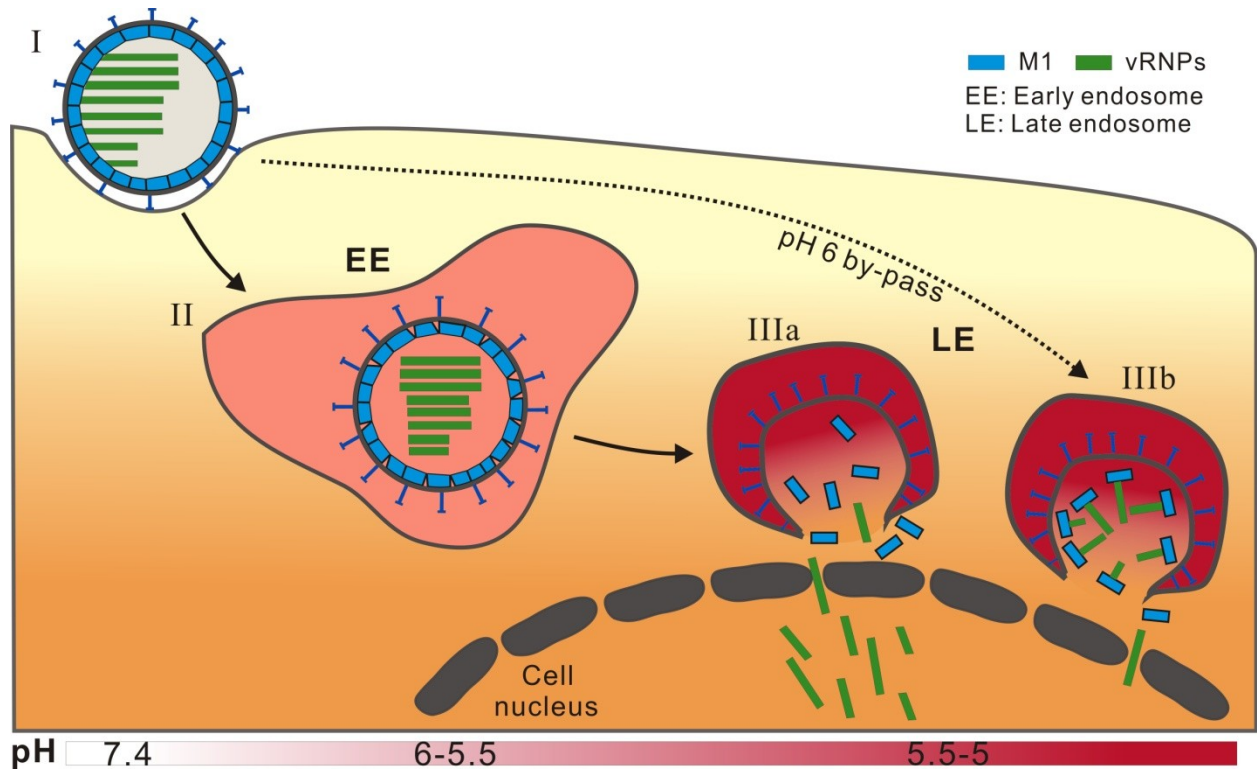


Fig 3.4.1 Model of influenza virus entry and uncoating events. (Solid line) (I) The influenza virus binds to the sialic acid receptors on the cell surface with its HA, and is then endocytosed mediated mainly by CCP. (II) After endocytosis viruses reach early endosomal compartments. At pH 6.5-6 M2 starts to conduct protons, which acidifies the viral interior and leads to weakening of the M1-M1 interaction. At pH~6 HA starts to change its conformation to initiate fusion. (IIIa) At pH 5.5-5 HA mediated fusion reaches its maximum, M1 disassembles and is released into the nucleus together with the viral RNPs. (Dashed line) (IIIb) Acid by-pass at the plasma membrane simulates late endosomal localization without passing mildly acidic compartments and leads to aggregation of M1 with vRNPs.

4. APPENDICES

4.1. Nano-particle size determination

4.1.1. Dynamic light scattering

When particle sizes are in the nanometer range, traditional optical microscopy methods are incapable in measuring their dimensions directly. One can always use higher resolution microscopy methods, e.g. electron microscope or atomic force microscope, to do the job. However, those methods usually require time-consuming sample preparation work, and are not capable of measuring sizes of large number of particles quickly, and may also introduce artifacts to the image (samples recorded by AFM may be deformed). Dynamic light scattering (DLS) fills this gap. Nanoparticles show Brownian motion when they are suspended in liquid, because the liquid molecules will continuously hit the particles, which results in a random motion of the particles. For particles of the same density, larger ones are heavier and moves more slowly, since their motions are less affected by the momentum transferred from the collided water molecules. DLS takes advantage of this phenomenon. A laser beam is projected into the particle-liquid mixture, when the particles move through the pathway of the laser, the laser light will be scattered, which is received by a detector. The time dependent fluctuation of the signal intensity is dependent on the speed of the particle movement, which is proportional to the size of the particles. **Fig 4.1.1** shows the concepts of DLS.

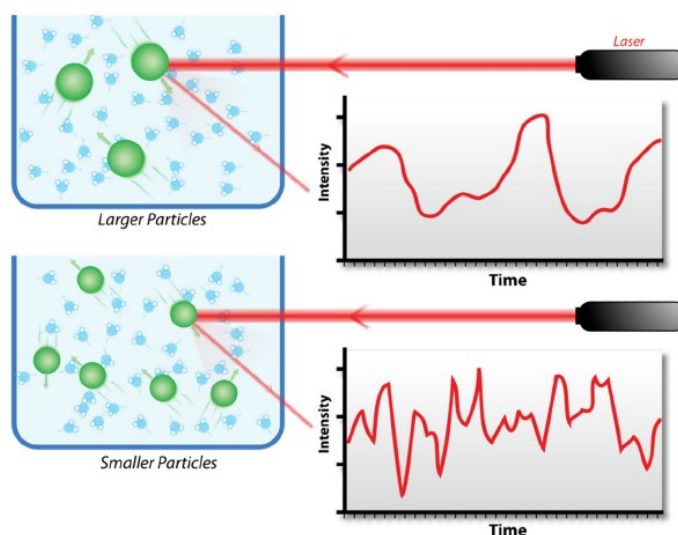


Fig 4.1.1 Cartoon showing the concept of dynamic light scattering by comparing the measurements of two samples: Larger particles on the top and smaller particle on the bottom. The larger particles moves

with less speed compared to the smaller ones, resulting in signals with lower frequency. The image is from Wikipedia.

DLS is an accurate tool in determining the size distribution of particles of narrow size distributions, it has the advantage of 1) Convenient sample preparation. One just needs to purify the sample by filtering dust or clusters away before measurement. 2) Fast measurement. One measurement takes only seconds. 3) Size distribution available. The output of the results shows the size distribution of the particles. However, when it deals with multi-modal size distribution systems, the precision of DLS can be largely affected. In our case, the viruses are pleomorphic, ranging from spherical to cylindrical shape, which dimensions are 30-300 nm. Such variety would result in an unfaithful representation of the size distribution if it was carried out by DLS. Another method that can be applied for the same purpose, which is single virus tracking.

4.1.2. Viral particle size determination by single virus tracking

Introduction

Most influenza virus strains are not perfectly spherical. They exhibit elongated morphology, which diameter is approximately 100 nm. When incubated at low pH, they become pleomorphic and round up into particles as large as 300 nm, as observed by (58, 200). We hypothesized that this phenomenon is related to the behavior of M1 protein matrix at low pH, and are interested in studying the swelling statistically. Many methods are available to measure the size of nanoparticles, but only few of them are capable of dealing with the measurement of thousands of particle in a short time. Single particle tracking of 2D Brownian motion was proven to be an accurate method in determining the size distribution of particles, and has provided us an opportunity to conduct the measurement (201). Although commercial equipment is available for this purpose, most of which use a laser source as illumination method and a dark field microscope as observation tool, we decided to perform the experiments on a lab designed microscope. The equipment uses an ordinary LED as illuminator for a simple upright microscope, which was equipped with a dark field condenser. A low noise camera was used to record the Brownian motion video, which was processed by an open source tracking software. We have also programmed a track processor which is capable of calculating the particle diameter from their tracks.

Theoretical background

-Brownian motion

The Brownian motion is one type of the Wiener processes, which describe the continuous-time stochastic processes. A typical stochastic differential equation (SDE) has the form:

$$dX_t = \mu(X_t, t)dt + \sigma(X_t, t)dW_t \tag{4.1.1}$$

where W_t is a Wiener process; the function μ is the drift coefficient; σ is the diffusion coefficient. The stochastic process X_t is called a diffusion process.

The stochastic differential equation can be interpreted that in a small time interval of length δ , the stochastic process X_t changes its value by an amount that is normally distributed with expectation $\mu(X_t, t)\delta$ and variance $\sigma(X_t, t)^2\delta$ and is independent of the behavior of the process in the past. A standard Wiener process on the interval $[0, T]$ is a random variable $W(t)$ that depends continuously on $t \rightarrow [0, T]$ and satisfies:

$W(0) = 0$, for $0 \leq s < t \leq T$,

$$W(t) - W(s) \sim \sqrt{t - s}N(0,1) \tag{4.1.2}$$

where $N(0,1)$ is a normal distribution with zero mean and unit variance.

This process is often referred to as Gaussian. For $0 \leq s < t < u < v \leq T$, $W(t)-W(s)$ and $W(v)-W(u)$ are independent. For use on a computer, we discretize the Wiener process with a timestep dt as:

$$dW_t = \sqrt{dt}N(0,1) \tag{4.1.3}$$

-Stokes-Einstein equation

In 1905, Einstein published a relation describing the Brownian motion, which is named after him: the "Einstein relation" (202).

$$D = \mu k_B T \tag{4.1.4}$$

where D is the diffusion constant; μ is the "mobility"; k_b is Boltzmann's constant; T is the absolute temperature.

For diffusion of non-interacting spherical particles in the liquid, the Stokes-Einstein equation builds up relations correlating the diffusion constant and the radius of the particles:

$$D = \frac{k_B T}{6\pi\eta r} \tag{4.1.5}$$

where r is the radius of the particle; η is the viscosity.

This relation has become an important method to obtain information about the dimension of nanometer size particles.

-Fokker-Planck equation

The Fokker-Planck equation describes the time evolution of the probability density function of the position of a particle. In one spatial dimension x , the Fokker-Planck equation for a process with drift $D_1(x,t)$ and diffusion $D_2(x,t)$ is:

$$\frac{\partial}{\partial t} f(x, t) = - \frac{\partial}{\partial x} [D_1(x, t) f(x, t)] + \frac{\partial^2}{\partial x^2} [D_2(x, t) f(x, t)] \quad (4.1.6)$$

where D_1 is the drift vector and D_2 is the diffusion tensor.

The Fokker-Planck equation can be used for computing the probability densities in mathematical systems described by stochastic differential equations. Consider the stochastic differential equation of Brownian motion **equation (4.1.1)**, If the initial distribution is $X_0 \sim f(x,0)$, then the probability density $f(x,t)$ of the state X_t is given by the Fokker-Planck equation with the drift and diffusion terms:

$$D_i^1(x, t) = \mu_i(x, t)$$

$$D_{ij}^2(x, t) = \frac{1}{2} \sum_k \sigma_{ik}(x, t) \sigma_{jk}(x, t) \quad (4.1.7)$$

In our case, we consider an ideal 2 dimensional diffusion of the viral particles in the buffer, and ignored the drift part D_1 . The diffusion constant can be written as:

$$D = \frac{kT}{6\pi\eta r} = \frac{1}{2} \sigma * \sigma^T = \frac{\overline{(x, y)^2}}{4t} \quad (4.1.8)$$

where $\overline{(x,y)^2}$ is the mean square displacement (MSD), which is a measure of the average distance a particle travels. The MSD can be written as:

$$MSD = \overline{(x, y)^2} = \frac{1}{i_{max}} \{ [x_n(i\Delta t) - x_n(i\Delta t - \Delta t)]^2 + [y_n(i\Delta t) - y_n(i\Delta t - \Delta t)]^2 \} \quad (4.1.9)$$

where i_{max} is the number of valid time steps in the given track; Δt is the duration of each time step.

The MSD can be measured by single virus tracking experiment, if the location of each virus is recorded after each time interval. If the MSD has been measured by experiments, one can obtain the diameter of the particle as:

$$d = \frac{4k_B T \Delta t}{3\pi\eta(x, y)^2} \quad (4.1.10)$$

where Δt is the duration of the time interval.

In reality, the Brownian motion is a 3 dimensional process, however, our microscope is only capable of recording the motion 2 dimensionally. Therefore the MSD in **equation (4.1.10)** is the projection of the real MSD in the x-y plane. If the observation is 3 dimensional:

$$d = \frac{2k_B T \Delta t}{\pi\mu(x, y, z)^2} \quad (4.1.11)$$

Monte Carlo simulation of the Brownian motion

Our measurement requires resolving diameters with an accuracy of 10 nm, which means the standard error of the mean (s.e.m) of the Gaussian diameter distribution should be less than 5 nm. To achieve this accuracy, one needs to optimize the tracking measurement by knowing which time interval is optimal, how long the particle movement has to be recorded, and at least how many particles need to be measured. An simulation based on the Monte Carlo method was performed to achieve this goal.

Mathematica (Wolfram Research, Illinois) was used to program and to simulate the 2D Brownian motion of N particles (input diameter d) in a duration of t and n steps of Δt , and then average their square displacements SD over N. Plotting the MSD over time allows us to calculate the diameter D, as was shown in Equ.(4.1.10). By comparing the values of calculated diameter and predicted diameter, we are able to know how to optimize the parameters t, n, N and d. **Fig 4.1.2** shows an example of simulation, and the outputs of the simulation.

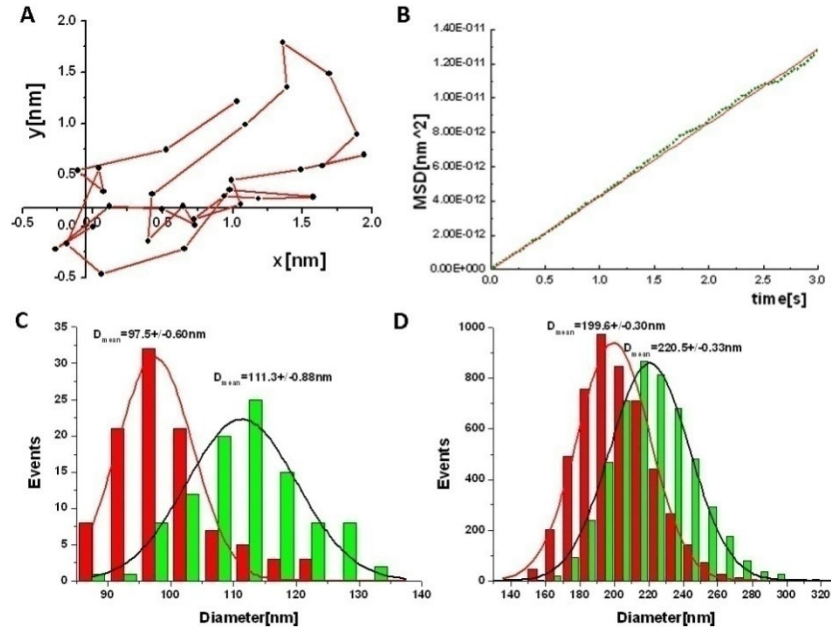


Fig 4.1.2 (A) A track showing the first 30 steps of random Brownian motion of a $d=140$ nm, $t=3$ s, $n=100$ steps particle (the rest 70 steps not shown). (B) After repeating the simulation based on the criteria given in (A) 500 times, MSD was plotted over time. As one can see, they are proportionally related and can be fit linearly. (C) and (D) Two examples showing the accuracy affected by the number of events. (C) Red: $D=100$ nm, green: $D=110$ nm, both: 100 particles, 5 seconds tracking, 30 fps. The s.e.m are 0.7 nm (red), and 1.2 nm (green). (D) Red: $D=200$ nm, green: $D=220$ nm, both: 5000 particles, 3 seconds tracking, 30 fps. The s.e.m is 0.5 nm (red), and 0.23% (green). Clearly, more events result in better accuracy.

The following tables show a systematical study on the influence of repetition time N , number of steps n , sampling time t and input particle size d on the accuracy of the output results.

Table 6: Testing the number of particles N ($d=240$ nm, $t=1$, steps=30)

N	10	30	50	100	500	1000
D(nm)	224.6	262.5	244.7	246.5	242.6	240.4
s.e.m (nm)	4.87	4.11	0.66	0.65	0.12	0.013

Conclusion: the calculation accuracy increases with the number of particles.

Table 7: Testing the number of steps n(d=240nm, t=1, N=200)

n	5	10	30	50	100	300
D(nm)	251.1	256.7	254.5	259.2	249.2	262.9
s.e.m (nm)	0.78	1.18	1.03	1.36	0.65	1.62

Conclusion: the calculation accuracy doesn't increase with number of steps.

Table 8: Testing the sampling time t (d=240nm, steps/t=10 fps, N=200)

t	0.5	1	3	10	30
Steps	5	10	30	100	300
D(nm)	240.8	254.6	239.6	221.0	220.9
s.e.m (nm)	0.06	1.03	0.03	1.34	1.35

Conclusion: the sampling time seems not related to the calculation, which may be correct for the simulation; but in experiment, due to the 3 dimensional movement of particles, longer sampling time is not recommended.

Table 9: Testing the input particle size d (Steps=10, t=1, N=200)

d(nm)	20	80	100	150	300	500
D(nm)	19.2	84.6	104.9	161.0	293.1	481.6
s.e.m (nm)	0.06	0.33	0.35	0.78	0.49	0.06

Conclusion: for simulation, the particle size may have no influence on the accuracy, however, in the experiments, too small particles may not be recognized by the microscope and camera, too large particles will lead to larger errors during tracking.

In general, the simulation shows 1) higher resolution of the particle sizes can be achieved by measuring more particles; 2) At least 100 particles are required for 10nm resolution; 3) Longer tracking time, higher frame rate do not really improve the accuracy. However in real experiments, more issues need to be considered. Firstly, longer sampling duration is not recommended, since the particles may go out of the view during tracking. Secondly, the instruments we use to image the particles have resolving limitations. If the particles are too small to be clearly distinguished, or too large to saturate the image, the determination of the position of the particles will be affected.

Experimental measurements

Monte Carlo simulations were conducted prior to the experiments to optimize the experimental parameters to be set. To perform single particle tracking, a dark field microscope with an Olympus Plan CN 100 \times /1.25 oil immersion objective with adjustable iris (Numerical aperture (N.A.) \sim 0.6-1.2) was constructed with an Olympus CX41RF upright microscope (Tokyo, Japan). A white light high power LED was placed under the specimen stage to illuminate the sample. A low noise EMCCD *Luca S* camera from *Andor* (Belfast, Ireland) with 658 \times 496 pixels was used to visualize and record the particle motion at the frame rate of 25 frames per second (fps). The tested samples were silica beads (50-500 nm in diameter) suspended in water as well as influenza A/X-31 viruses in PBS (grown in eggs, 676 ug/ml in concentration). The pH of PBS was controlled by adding 10 mM sodium acetate+150 mM NaCl. The viruses were incubated at low pH buffer at room temperature for 15 minutes before experiments. All virus samples were filtered through 220 nm filters to avoid clusters. All samples were pipetted into micro-chambers made from parafilm, and covered with cleaned cover glass. Each video was recorded for 5-10 seconds and was processed by GMimPro (NIMR, London), which is capable of tracking the movement of bright pixels in the video and exporting the time dependent coordinates. The tracks were further processed by *Mathematica* (Wolfram Research, Illinois) based program to obtain the statistics of the particle sizes. All tracking experiments were conducted at room temperature. All videos were recorded after equilibrating the sample for 1 minute to avoid drift.

Before carrying out the methods directly on viruses, tracking experiments on silica beads were performed to test the instrument. Two groups of silica beads ($D=575$ nm, $D=200$ nm, Seradyn, Indianapolis, USA) suspended in filtered water were tested. Videos of 230 beads (575 nm) and 425 beads (200 nm) were recorded and analyzed. The calculated diameters were plotted as histogram and fitted with a Gaussian. The average diameter and standard error were extracted from the fitting. The average size of 575 nm beads is 572 ± 20.5 nm, the average size of 200 nm beads is 224 ± 3.1 nm. Both results resemble the real diameter of the beads and demonstrate that the method works well. Next the method was applied to influenza viruses. X-31 viruses diluted 2000 times in neutral PBS (pH 7.2) and preincubated at low pH (pH 4.6) were tested. Tracking results of 659 pH 7.2 viruses showed an average diameter of 230.8 ± 5.0 nm; and 522 of pH 4.6 viruses showed an average diameter of 272.6 ± 6.6 nm. The average diameter of the viruses enlarged by ~ 40 nm at low pH.

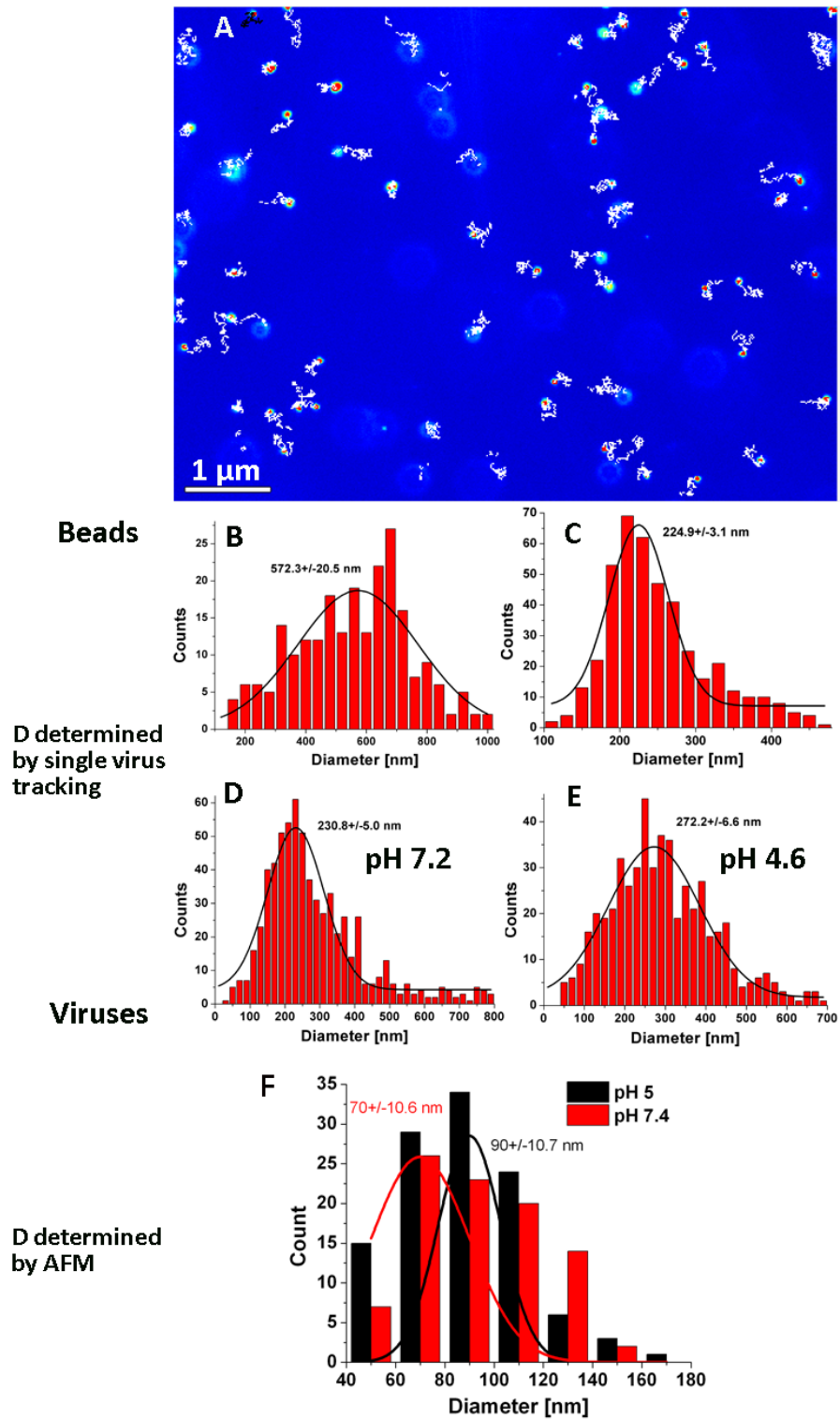


Fig 4.1.3 Size determination of silica beads and viruses by single particle tracking. (A) Example showing tracking of the Brownian motion of 200 nm beads. The white zigzag curves show the tracks of bead

motion. (B) and (C) Histogram of size distribution of 230 beads (575 nm) and 425 beads (200 nm), which were fitted with Gaussian. The average size of 575 nm beads is 572 ± 20.5 nm (standard error), the average size of 200 nm beads is 224 ± 3.1 nm. (D) and (E) X-31 viruses diluted in neutral PBS (pH 7.2) and preincubated at low pH (pH 4.6) were tracked. Tracking results of 659 pH 7.2 viruses showed an average diameter of 230.8 ± 5.0 nm; and 522 of pH 4.6 viruses showed an average diameter of 272.6 ± 6.6 nm. (F) The influenza viral diameters determined by AFM measurements were also plotted in histogram for comparison.

The viral diameters measured by this method are larger than that by the AFM (**Fig 4.1.3 F**). There are several reasons for this: 1) After being imaged by AFM, the particles may be deformed. 2) The sensitivity of the microscope made it difficult to clearly observe single viruses. Maybe the method selected only the largest viruses and ignored the smaller ones.

4.2. Characterization of AFM tip induced image artifacts

4.2.1. Tip shape characterization

According to **Fig 1.3.8 A**, the tip shape of bio-lever BL-RC150VB can be approximated as the upper part of a hyperbolic function:

$$y = b \sqrt{1 + \frac{x^2}{a^2}}$$

$$\frac{y^2}{b^2} - \frac{x^2}{a^2} = 1$$

(4.2.1)

where a and b are positive parameters.

Assuming that the hyperbolic tip exhibits radius of curvature TR and open angle ϑ , the hyperbolic parameter a and b will have to be converted to TR and ϑ for convenience.

Radius of curvature TR :

The radius of curvature is the reciprocal of the curvature of a curve.

For any curve described by a function $y=f(x)$, the curvature at (x_0, y_0) is:

$$k = \frac{y''}{(1+y'^2)^{3/2}} \text{ at } x=x_0, y=y_0$$

(4.2.2)

which can be written as the approximation:

$$k \approx \left| \frac{d^2y}{dx^2} \right|$$

(4.2.3)

Therefore

$$TR = \frac{1}{k} \xrightarrow{\text{bottom of the tip where } x=0, y=0} \frac{a^2}{b}$$

(4.2.4)

Open angle θ :

The boundaries of a hyperbola can be approximated as linear, as is shown in **Fig 4.2.1**. We use open angle ϑ to describe the half open angle of the hyperbola.

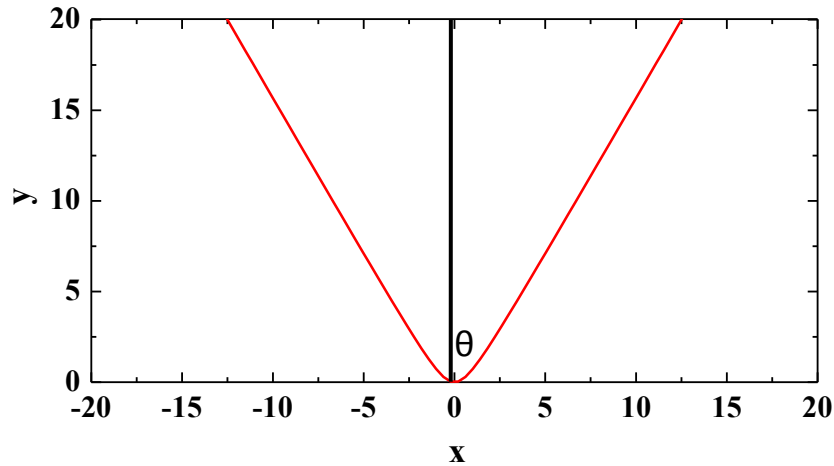


Fig 4.2.1 The tip can be approximated as a hyperbola, which boundaries can be assumed as linear.

Therefore ϑ can be characterized by a and b :

$$ctan\theta \approx \frac{y}{x} \approx b \sqrt{\frac{1}{x^2} + \frac{1}{a^2}} \approx \frac{b}{a} \tag{4.2.5}$$

at large x values.

From **equation (4.2.1), (4.2.4) and (4.2.5)**, the equation for a ϑ degree open angle and TR radius hyperbola upper part can be written as:

$$y = \frac{1}{\tan\theta} \left(\sqrt{x^2 + \frac{TR^2}{\tan^2\theta}} - \frac{TR}{\tan\theta} \right) \tag{4.2.6}$$

In which the last part $TR/\tan \vartheta$ is used to ensure $f(x=0)=0$.

Equation (4.2.6) is the universal hyperbolic shape tip function, with parameter ϑ and TR .

To give an example, **Fig 4.2.2** shows the dilation of a 70nm circle by this hyperbolic tip ($TR=20$ nm, $\theta=30^\circ$):

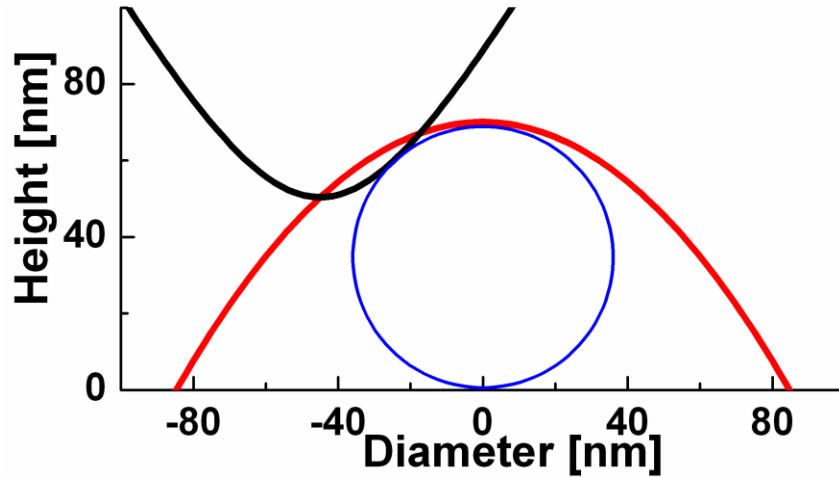


Fig 4.2.2 Simulation showing the image (red) of a circular object (blue, diameter=70 nm) is dilated by a hyperbolic AFM tip (black, $TR=20$ nm, $\theta=30^\circ$). The image width at $y=0$ is more than twice the original diameter of the object.

4.2.2. Shape dilation function calculation

It will be useful to derive the dilation trace equation which only contains the parameter TR , r (circle radius), and θ . Theoretically, this can be realized by solving the quadratic equation of both the tip function, and the circle function. The results are their intersections. There can be 4 results, if one forces them to be the same, the trace can be solved. Here we estimated the relation it by numerical fitting.

Fixing the tip geometry as $TR=20$ nm, $\theta=30^\circ$ (according to manufacturer's description), we have calculated the dependence of maximum image width on the radius of the circular object, which is plotted in **Fig 4.2.3**.

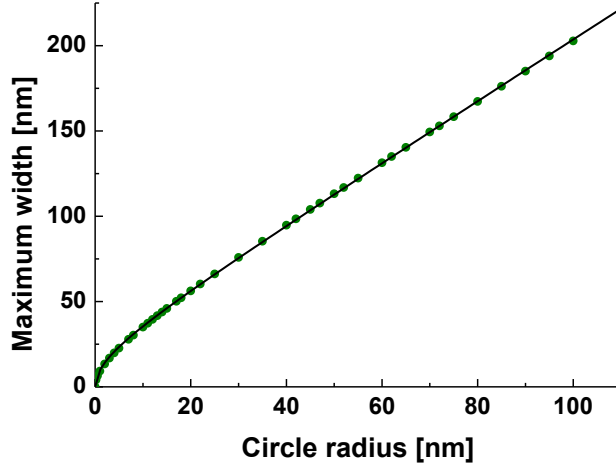


Fig 4.2.3 Maximum image width versus radius of the circular object. The green dots are the numerical simulated data points, the black force are the fitting of a hyperbolic function to the dots. The relation shows a clear hyperbolic behavior, however, it can be assumed to be linear when the circle radius is larger than 10 nm.

To prove the hyperbolic behavior of **Fig 4.2.3**, we assume the tip exhibits the geometry following **equation (4.2.6)**.

The image exhibits the geometry (opening downwards) following:

$$y = \frac{1}{\tan\phi} \left(-\sqrt{x^2 + \frac{R^2}{\tan^2\phi} + \frac{R}{\tan\phi}} \right) \quad (4.2.7)$$

where R is the radius at the top, ϕ is the half open angle.

Equation (4.2.7) must satisfy $y=2r$ when $x=0$, where r is the circle radius. Therefore:

$$y = \frac{1}{\tan\phi} \left(-\sqrt{x^2 + \frac{TR_2^2}{\tan^2\phi} + \frac{TR_2}{\tan\phi}} \right) + 2r \quad (4.2.8)$$

At $y=0$, the x value is the maximum width (L) of the image.

$$L = 2\sqrt{r^2 \tan^2\phi + r * TR_2} \quad (4.2.9)$$

which is also a hyperbola (dependent on the radius of the circle).

4.3. Low force mechanical measurements with AFM and optical tweezers

4.3.1. Mechanics of the cell membrane by AFM pulling experiments*

Introduction-Cholesterol activity in the neuron

Cholesterol is a basic building block for the construction and maintenance of plasma membranes. Defects in cholesterol synthesis may lead to devastating consequences on the developing nervous system, for example corpus callosum agenesis (203). The cholesterol activity in the adult brain is clearer: it is known that cholesterol is synthesized in the cortical and hippocampal neurons in the adult brain (204); glial cholesterol circulates in the brain, which can also be benefited by the neurons (205); some adult neurons no longer require endogenous cholesterol synthesis, and can rely on the surrounding cholesterol to meet their needs (206). However, the cholesterol activity in the premature brain is less known. For example, which cell types account for the cholesterol synthesis in the developing brain? Will cholesterol synthesis inactivation affect the survival of mature/premature neurons? To which degree cholesterol flux between cells can rescue cholesterol deficits? We have participated in a work which aimed at answering these questions (207). We characterized different neuron cells by measuring their tether forces. A tether, which is a nanotube formed from membrane, was shown to be extractable from cell plasma membrane (208). The tether force, which is the force required to pull this tether from the cell, is a measure for plasma membrane bending rigidity and interaction of the membrane with the underlying cytoskeleton (209). By applying AFM pulling experiments on cholesterol deficient mutant cells and control premature neurons in the presence or absence of exogenous cholesterol supply, we supported the idea that neurons can use external cholesterol to rescue the retarded development caused by their disability to produce their own cholesterol.

Results and discussion

To verify if the cholesterol synthesis prohibited premature neurons can be rescued by exogenous cholesterol supply, *SQS/Nex-cre* mice hippocampal neurons and their controls were prepared. The *SQS/Nex-cre* mice hippocampal neuron is a mutant neuron type, of which cholesterol synthesis is inactivated as early as embryonic day 11.5. Both mutant and control cells were kept in the presence or absence of exogenous cholesterol supply for 2 days *in vitro*.

The mechanical properties of these cells were measured by tether extraction using AFM (210). For the experiments we used Olympus biolevers with a calibrated spring constant of ~ 0.006 or ~ 0.03 N/m. The experiments were performed at 24°C. The AFM was placed onto a bright-field illuminated inverted optical microscope equipped with a 60x, 1.49 N.A. objective. First, a cell was selected with the optical

* This is part of the work was performed in collaboration with Dr. G.Saher from the Max Planck Institute for Experimental Medicine, Goettingen. The cells were provided by Saher. G, the AFM mechanical measurements were performed by me.

microscope and the AFM tip was positioned above the cell body. Then the tip was brought down to push the cell at ~ 250 pN and pulled away for a distance of 5 μm . A schematic in **Fig 4.3.1** shows the principle of the experiment.

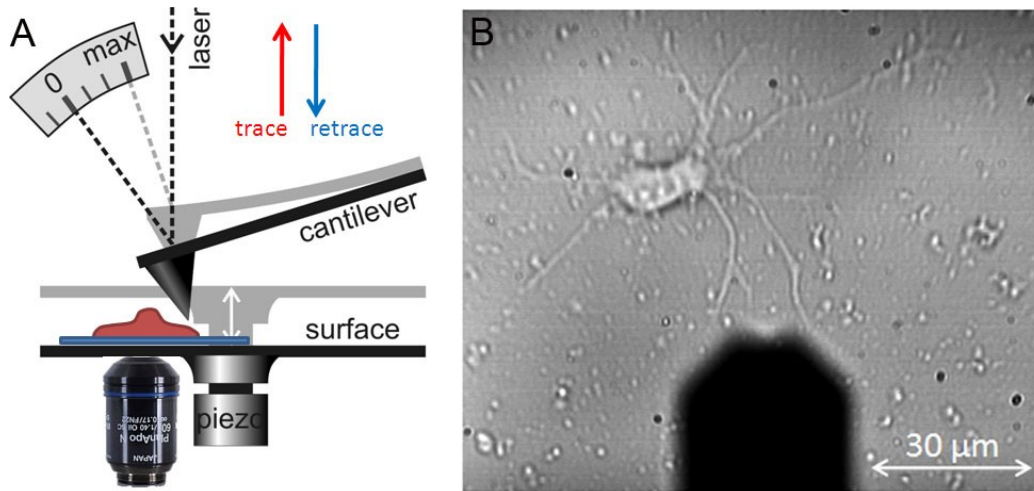


Fig 4.3.1 The principle of AFM measurements on cell tether force measurements. (A) A bright-field illuminated inverted optical microscope is combined with the AFM. An oil immersion objective is placed under the cell sample. Before the mechanical measurements, a neuron cell which exhibited a healthy morphology was selected by the optical microscope. Once the cell was selected, the tip was brought down to contact the cell and pulled away for a distance of 5 μm . (B) A view of a selected neuron and the cantilever out of focus (black).

Force-extension curves were recorded during the pushing and pulling process. In about 20 % of all curves a tether was extracted by the AFM tip, which was visible as constant force plateau when the tip was retracted (**Fig 4.3.2 A**). When the tether ruptures, the force returns to zero. The jump in force upon rupturing was measured as the tether force. Occasionally, multiple tethers were pulled, which is reflected on the multiple rupture events shown in the pulling curve (**Fig 4.3.2 B**). The tethers rupture one after another, because the gaps appear at different places on the x-axis. If multiple tethers were found in the force curves, only the last gap was measured. Since the tether force was measured at a relatively low pulling speed of 2 $\mu\text{m/s}$, the presented tether forces are 10-20% higher than the force F_0 that would be required to hold the tether at a constant length (211).

The tether force of 15–30 cells from 4 mice per genotype were measured and plotted as histogram (**Fig 4.3.2 C**). Gaussian fitting was performed to calculate the average tether forces (**Table 10**), which was plot in **Fig 4.3.2 D**. The mutant cells show a higher tether force than the control cells, therefore the cholesterol decreases the tether force. This is in agreement with (211). The addition of cholesterol

results in an almost identical tether force for the mutant and control cells. These findings indicate that neurons can use external cholesterol to rescue the retarded development caused by cholesterol deprivation.

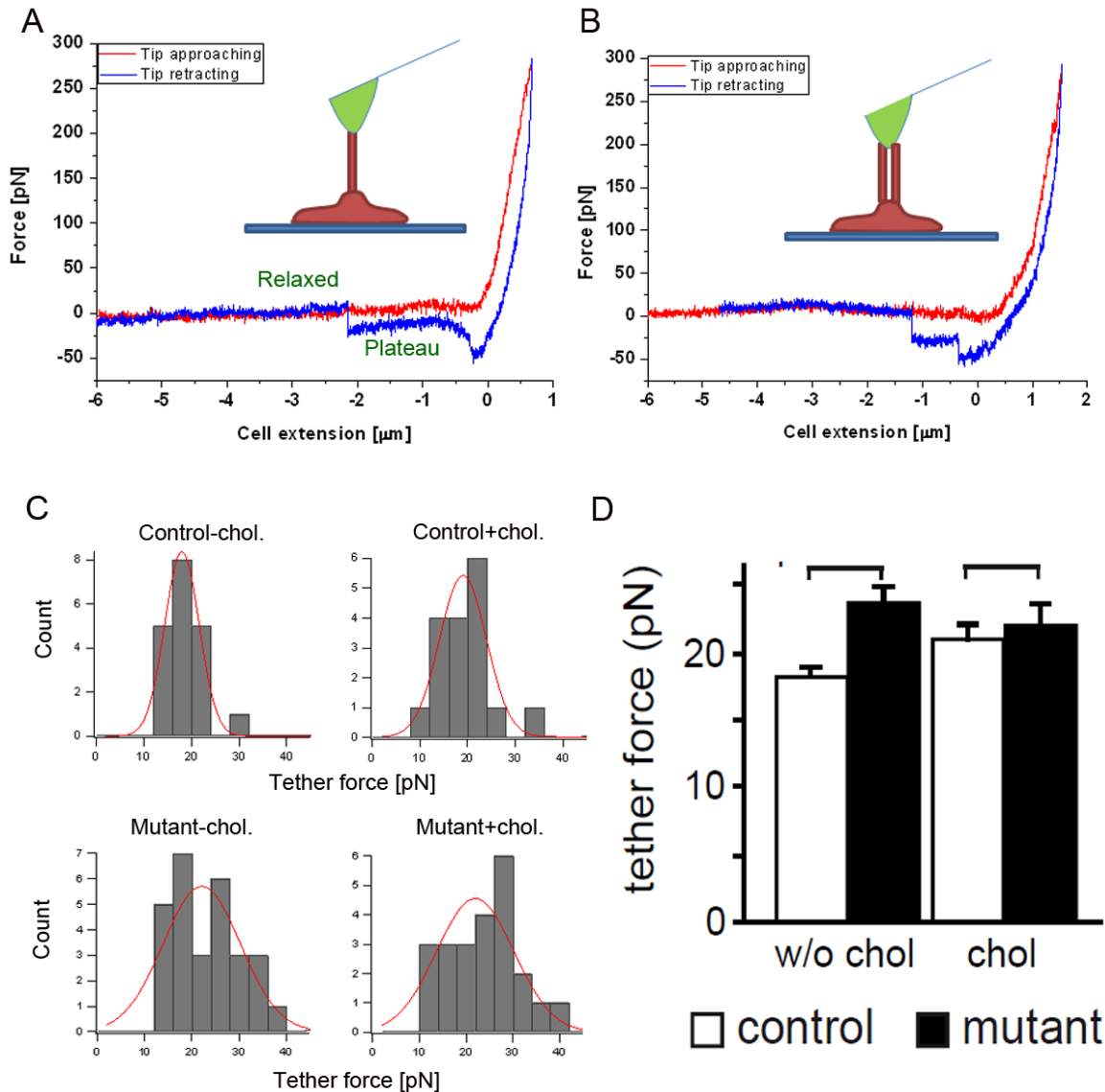


Fig 4.3.2 Tether force measurement on hippocampal cells. (A) and (B) Single and multiple tethers pulled by the tip are visible by the number of gaps on the force-extension curve. In each plot, the red curve represents the tip approaching to the cell; the blue curve represents the tip retracting from the cell. A constant force plateau indicates the existence of a tether pulled by the tip. The jump in force after rupture is the tether force. (C) The tether forces were measured for mutant and control premature neurons in the presence or absence of exogenous cholesterol supply, and plotted in histogram for

Gaussian fitting. (D) Interestingly, the membrane tension of mutant neurons was significantly higher, and this difference was leveled out by the addition of cholesterol.

Table 10: Average tether forces of mutant and control premature neurons in the presence or absence of exogenous cholesterol supply. The numbers in the parenthesis denote the number of measurements.

	without chol. (pN±s.e.m)	with chol. (pN±s.e.m)
control	18.2±0.5 (19)	20.9±1.3 (17)
mutant	23.6±1.2 (28)	21.9±1.7 (23)

4.3.2. Mechanics of cells by optical tweezers pushing[†]

Introduction: Cell mechanics measurements

The mechanical properties of cells can be used as an indicator to reflect the role of specific cell types and activities in a tissue (212). For example, cancer cells can be distinguished from their healthy counterparts by the fact that cancer cells are generally softer (213). Compared to viruses, the architecture of eukaryotic cells is highly complicated: they are wrapped by a lipid bilayer and a ~100 nm thin cortical layer which supports this membrane. This cortical network is composed of actin filaments, actin-binding proteins including myosin motors, and encloses a crowded liquid environment, the cytoplasm. The different components that make up the cell will all contribute to the measured cell response in a ratio that depends on the measurement technique and the timescale of the experiment. As a consequence, the cell mechanics can exhibit viscoelastic behavior, and the result is dependent on how fast the measurement is performed.

Many techniques are available to measure the cell mechanics, including micropipette aspiration, AFM, magnetic bead pulling, and optical tweezers (214). All the methods aim at observing the magnitude of active or passive deformation of the cell. The elastic constant (Young's modulus) of most animal cells are in the order of 0.1-100 kPa (215), considerably softer than that of non-enveloped viruses (~1 GPa) (32). Therefore the cell mechanical measurements require much higher force resolution and better signal-to-noise ratio. The lowest force that can be exerted by AFM is around 20 pN, since the cantilever is affected by the thermal noise in liquid (150). Indeed, most AFM experiments are performed from 0.1 up to several nN. With optical tweezers lower forces can be applied. The optical tweezers trap micrometer

[†] This is part of the work in collaboration with Prof. M. Simon from the Max Planck Institute for Experimental Medicine, Goettingen. Most of the measurements were performed by S. Nawaz and P. Sanchez. The optical-trap setup was in part constructed and calibrated by me. I also performed the initial experiments on cells.

beads by a focused laser beam. This technique has been applied to pull membrane tethers from the cell membrane (152). In conventionally configured optical tweezers the trapped bead is moved horizontally in the xy-plane to pull or push on the sample. When this configuration is used for cell measurements, the boundary conditions are no longer symmetric, and the interpretation of the results and the modelling of the experiment become much more complicated. In our studies, the vertical optical trapping method was developed to push on the 3T3 embryonic fibroblasts at different forces. The measurements were repeated by AFM for comparison. Part of this section has been published in (151).

Results and discussion

In order to deform cells in the vertical direction, perpendicular to the coverslip, we constructed an optical trap setup. The objective was mounted on a piezo element such that the optical focus and the position of the trapped bead could be changed simultaneously perpendicular to the coverslip (**Fig 4.3.3 A**). For our experiments it was essential to measure accurately the bead displacements along the z-axis, which is a less well established technique than position detection in the xy-plane. To test the linear range and resolution of the quadrant photo diode based detection system in the z-direction, we focused the trapping laser on a bead that was bound to the coverslip and moved the trap in the z-direction. When we moved the piezo with a square wave, we were able to record movements with a resolution in the nanometer range (**Fig 4.3.3 B**). The linear range of the trap was measured by moving it with a 3 μm triangular wave. For displacements of up to 500 nm out of the trap center, the signal was linearly proportional to the displacement (**Fig 4.3.3 C**).

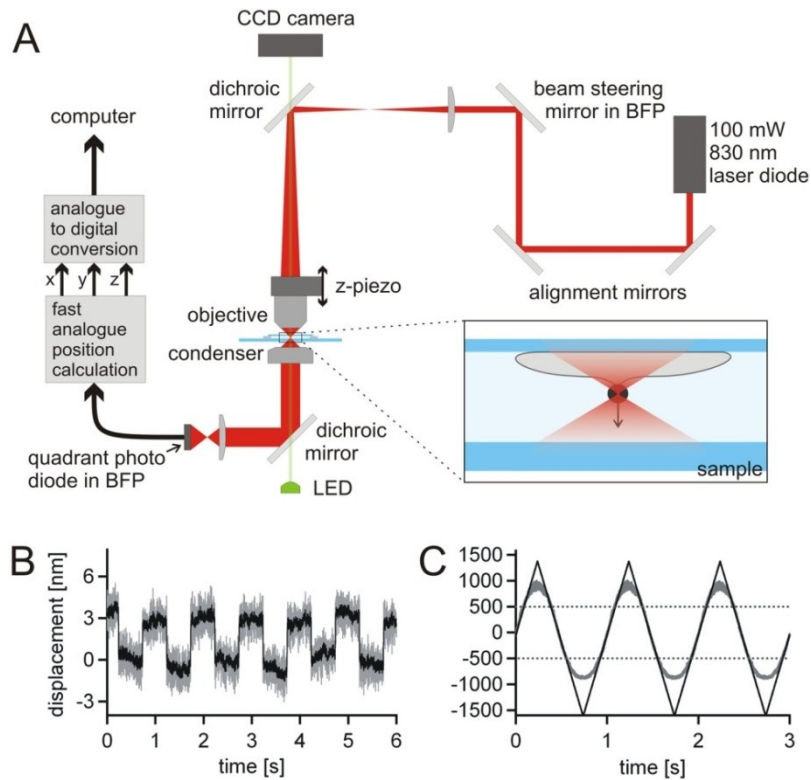


Fig 4.3.3 Laser trap setup to apply and measure forces in vertical direction. (A) A wavelength=975 nm laser beam was coupled into the optical path of a standard upright microscope via a dichroic mirror and focused into the sample by the water immersion objective. To monitor the displacement of the bead from the center of the trap, the laser light was collected by the condenser, coupled out of the optical path via a second dichroic mirror and cast onto a photodiode. The vertical position of the trap was controlled by a piezo element that moved the objective up and down. Inset) Cells were plated onto a poly-L lysine coated coverslip that was mounted in a closed sample chamber. (B) A bead fixed to the coverslip was trapped and the trap position was moved up and down with 3 nanometer steps. The trace was sampled at 1 kHz (in black, window averaged to 100 Hz) and shows a single nanometer resolution. (C) The same experiment as in B, but now the trap was moved with a triangular wave with a 3 μm maximum displacement (black trace). The response of the detector (gray trace) is linear proportional with the trap displacement up to ± 500 nm.

To calibrate the optical tweezers, polystyrene beads of 760 nm diameter were suspended in modified Krebs'-Ringer solution (containing 120 mM NaCl, 4.7 mM KCl, 1.2 mM CaCl₂, 0.7 mM MgSO₄, 10 mM Glucose, 10 mM Na-Hepes, pH 7.4) (216). The beads were sonicated in a water bath shortly before the experiment, and brought in a sample chamber that also contained the cells. The trap stiffness and the detector response were calibrated by recording the power spectrum of the noise and applying the equipartition theorem (217). We trapped a bead and recorded its noise during its approach towards the

cell and performed the calibration at intervals of 1 μm . By using a water immersion an almost constant trap stiffness can be achieved (218). For the cell indentation experiments we used the calibration value that was recorded at a height of 2 μm above the cell. During this approach a feedback loop was used to detect the contact of the bead with the cell. Once a force higher than ≈ 10 pN was detected the approach was stopped automatically. To test the linear range of the trap in z-direction we focused the trapping laser on a bead that was bound to the coverslip and moved the trap in the z-direction with a 3 μm triangular wave. For displacements of up to 500 nm out of the trap center, the signal was linearly proportional to the displacement. The axial spring constant of the trap was > 0.1 pN/nm, which gave a maximum force that could be reliably measured on the cell of up to 50 pN, which was sufficient for our measurements. The calibrated traces were window averaged to 1 kHz and showed displacement of the bead from the center of the trap. The force was calculated by multiplying the displacement with the trap stiffness. The cell deformation was computed from the displacement of the trap focus minus the displacement of the bead.

Next we investigated the cellular response by performing indentation measurements with an optical trap, which has a thermal force noise of less than 1 pN (219). Single cells were indented in vertical direction with a 760 nm diameter bead that was held by an optical trap. The force is obtained by measuring the vertical displacement of the bead out of the centre of the focused laser beam (**Fig 4.3.4 A**). When the cell is indented with these low forces, the indentation and retraction curves show little difference, indicating a response that is largely elastic (**Fig 4.3.4 E**).

We repeated the measurements with AFM at different forces. A 1.98 μm diameter bead was attached to an AFM cantilever and was used to indent the same cell type (**Fig 4.3.4 A**). In this scenario the applied force is measured via the bending of the cantilever. **Fig 4.3.4 B** shows that there is a considerable difference between the indentation and retraction curve when a cell is indented with a force of 140 pN. This hysteresis shows that the response is not elastic. Instead a viscous component is responsible for the dissipation of energy during indentation. We repeated the indentation experiments at lower forces. At a force of 75 pN the difference between the curves is less (**Fig 4.3.4 C**). **Fig 4.3.4 D** shows that the maximum applied force of 25 pN is almost on the same level as the noise, which makes these curves difficult to evaluate. A difference between the curves cannot be distinguished. Lower forces could not be tested due to the thermal noise limitations in liquid. The thermal noise of the AFM cantilevers we used is around 20 pN (150).

To extract the elastic Young's modulus E for the cell we fitted the optical tweezers curves to the Hertz model that describes the indentation of a large elastic body with a rigid spherical indenter:

$$F(d_z) = \frac{4E}{3(1-\nu^2)} * R_b^{1/2} d_z^{3/2} \quad (4.3.1)$$

where R_b is the bead radius, d_z is the indentation, and ν is the Poisson's ratio for which we choose 0.4 (220).

Equation (4.3.1) predicts the force F to increase with the indentation d_z to the 3/2 power. This non linear increase is the result from the increasing contact area between the cell and the indenter; the larger the contact area gets the harder it will be to further indent the cell. Applying the equation to analyze the force curves obtained by optical tweezers, the cell Young's modulus was estimated to be 100.3 ± 10.2 Pa ($n=90$). We fitted the low force part of the AFM curves (7-30 pN) to the Hertz model, and found the Young's modulus is consistent to that obtained from optical tweezers, although the AFM curves show higher noises. We suggest that, the optical tweezers can be used as an alternative to AFM to apply lower forces which may be useful for very soft samples.

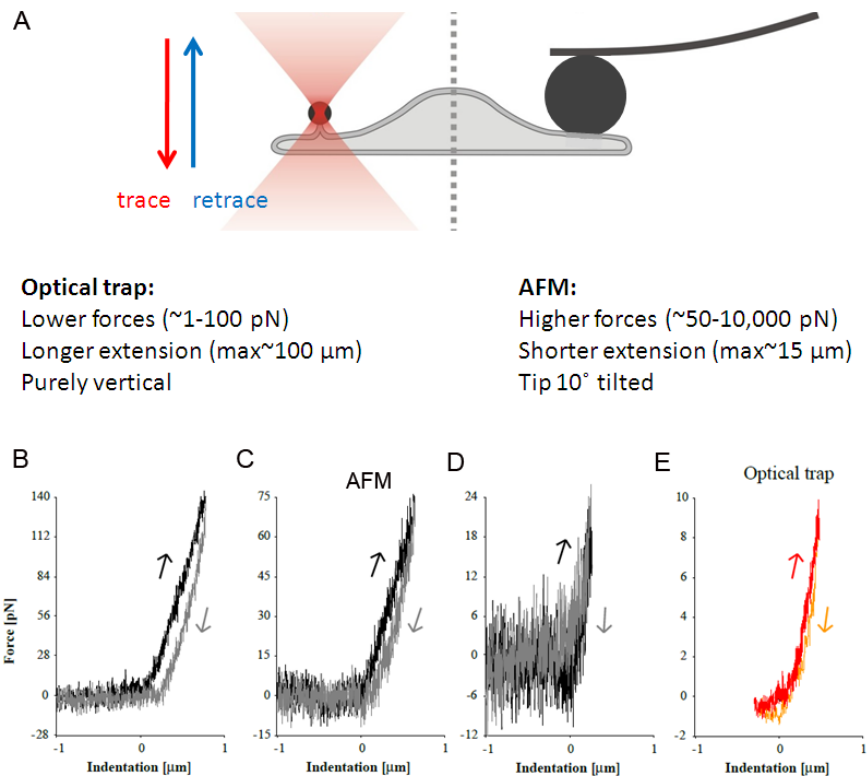


Fig 4.3.4 Comparison between AFM and optical tweezers on the low force measurements of cell mechanics. (A) Schematic showing how the cell mechanics are measured by optical tweezers (left) and AFM (right). The optical tweezers apply a laser-trapped bead to push or stretch on the cell membrane; the AFM applies a bead ($d=1.98 \mu\text{m}$) which is associated to the cantilever to do the same task. The advantages of using optical tweezers over AFM for low force measurements are summarized below. (B), (C) and (D) show AFM single indentation (black) and retraction (grey) curves exerted on a 3T3 fibroblasts cell up to 140 pN, 75 pN and 25 pN. The area of hysteresis between indentation (black) and retraction (grey) curves is inversely proportional to the maximum force. (E) Optical tweezers single indentation (red) and retraction (orange) curves exerted on the same cell up to only 10 pN. No obvious hysteresis is visible, and the plot shows much better signal-to-noise ratio.

REFERENCES

1. Iyer LA, Balaji S, Koonin EV, & Aravind L (2006) Evolutionary genomics of nucleo-cytoplasmic large DNA viruses. *Virus research* 117(1):156-184.
2. La Scola B, *et al.* (2003) A giant virus in amoebae. *Science* 299(5615):2033-2033.
3. Arslan D, Legendre M, Seltzer V, Abergel C, & Claverie JM (2011) Distant Mimivirus relative with a larger genome highlights the fundamental features of Megaviridae. *Proceedings of the National Academy of Sciences of the United States of America* 108(42):17486-17491.
4. Agbandje-McKenna M, Llamas-Saiz AL, Wang F, Tattersall P, & Rossmann MG (1998) Functional implications of the structure of the murine parvovirus, minute virus of mice. *Struct Fold Des* 6(11):1369-1381.
5. Caspar DL & Klug A (1962) Physical principles in the construction of regular viruses. *Cold Spring Harb Symp Quant Biol* 27:1-24.
6. Baker TS, Olson NH, & Fuller SD (1999) Adding the third dimension to virus life cycles: Three-dimensional reconstruction of icosahedral viruses from cryo-electron micrographs. *Microbiol Mol Biol R* 63(4):862.
7. Newcomb WW, Booy FP, & Brown JC (2007) Uncoating the herpes simplex virus genome. *Journal of molecular biology* 370(4):633-642.
8. Simpson AA, *et al.* (2000) Structure of the bacteriophage phi 29 DNA packaging motor. *Nature* 408(6813):745-750.
9. Harris A, Forouhar F, Qiu S, Sha B, & Luo M (2001) The crystal structure of the influenza matrix protein M1 at neutral pH: M1-M1 protein interfaces can rotate in the oligomeric structures of M1. *Virology* 289(1):34-44.
10. Mercer J, Schelhaas M, & Helenius A (2010) Virus entry by endocytosis. *Annual review of biochemistry* 79:803-833.
11. Whittaker GR, Kann M, & Helenius A (2000) Viral entry into the nucleus. *Annu Rev Cell Dev Bi* 16:627-651.
12. Ivanovska IL, *et al.* (2004) Bacteriophage capsids: tough nanoshells with complex elastic properties. *Proceedings of the National Academy of Sciences of the United States of America* 101(20):7600-7605.
13. Roos WH, Ivanovska IL, Evilevitch A, & Wuite GJL (2007) Viral capsids: Mechanical characteristics, genome packaging and delivery mechanisms. *Cellular and Molecular Life Sciences* 64(12):1484-1497.
14. Stephanidis B, Adichtchev S, Gouet P, McPherson A, & Mermet A (2007) Elastic properties of viruses. *Biophysical journal* 93(4):1354-1359.
15. Moffitt JR, *et al.* (2009) Intersubunit coordination in a homomeric ring ATPase. *Nature* 457(7228):446-U442.
16. Smith DE, *et al.* (2001) The bacteriophage phi 29 portal motor can package DNA against a large internal force. *Nature* 413(6857):748-752.
17. Gittes F & Schmidt CF (1998) Interference model for back-focal-plane displacement detection in optical tweezers. *Opt Lett* 23(1):7-9.

18. Kuznetsov YG, *et al.* (2010) Atomic force microscopy investigation of the giant mimivirus. *Virology*.
19. Kuznetsov Y, Gershon PD, & McPherson A (2008) Atomic force microscopy investigation of vaccinia virus structure. *J Virol* 82(15):7551-7566.
20. Carrasco C, *et al.* (2006) DNA-mediated anisotropic mechanical reinforcement of a virus. *Proceedings of the National Academy of Sciences of the United States of America* 103(37):13706-13711.
21. Falvo MR, *et al.* (1997) Manipulation of individual viruses: Friction and mechanical properties. *Biophysical journal* 72(3):1396-1403.
22. Roos WH, *et al.* (2009) Scaffold expulsion and genome packaging trigger stabilization of herpes simplex virus capsids. *Proceedings of the National Academy of Sciences of the United States of America* 106(24):9673-9678.
23. Ivanovska IL, *et al.* (2004) Bacteriophage capsids: Tough nanoshells with complex elastic properties. *Proceedings of the National Academy of Sciences of the United States of America* 101(20):7600-7605.
24. Roos WH, *et al.* (2012) Mechanics of bacteriophage maturation. *Proceedings of the National Academy of Sciences of the United States of America* 109(7):2342-2347.
25. Michel JP, *et al.* (2006) Nanoindentation studies of full and empty viral capsids and the effects of capsid protein mutations on elasticity and strength. *Proceedings of the National Academy of Sciences of the United States of America* 103(16):6184-6189.
26. Kol N, *et al.* (2007) A stiffness switch in human immunodeficiency virus. *Biophysical journal* 92(5):1777-1783.
27. Mateu MG (2012) Mechanical properties of viruses analyzed by atomic force microscopy: A virological perspective. *Virus research* 168(1-2):1-22.
28. Roos WH, Bruinsma R, & Wuite GJL (2010) Physical virology. *Nat Phys* 6(10):733-743.
29. Schaap I, Eghiaian F, des Georges A, & Veigel C (2012) Effect of envelope proteins on the mechanical properties of influenza virus. *Journal of Biological Chemistry*.
30. Li S, Eghiaian F, Sieben C, Herrmann A, & Schaap IA (2011) Bending and puncturing the influenza lipid envelope. *Biophysical journal* 100(3):637-645.
31. Thomas Y, *et al.* (2008) Survival of influenza virus on banknotes. *Applied and environmental microbiology* 74(10):3002-3007.
32. Mateu MG (2012) Mechanical properties of viruses analyzed by atomic force microscopy: A virological perspective. *Virus research*.
33. Georgens C, Weyermann J, & Zimmer A (2005) Recombinant virus like particles as drug delivery system. *Curr Pharm Biotechno* 6(1):49-55.
34. Lee ES, Kim D, Youn YS, Oh KT, & Bae YH (2008) A virus-mimetic nanogel vehicle. *Angew Chem Int Ed Engl* 47(13):2418-2421.
35. Ma Y, Nolte RJ, & Cornelissen JJ (2012) Virus-based nanocarriers for drug delivery. *Advanced drug delivery reviews* 64(9):811-825.
36. Fischlechner M & Donath E (2007) Viruses as building blocks for materials and devices. *Angew Chem Int Edit* 46(18):3184-3193.

37. Falkner JC, *et al.* (2005) Virus crystals as nanocomposite scaffolds. *J Am Chem Soc* 127(15):5274-5275.
38. Lee BY, *et al.* (2012) Virus-based piezoelectric energy generation. *Nat Nanotechnol* 7(6):351-356.
39. Canchaya C, Fournous G, Chibani-Chennoufi S, Dillmann ML, & Brussow H (2003) Phage as agents of lateral gene transfer. *Curr Opin Microbiol* 6(4):417-424.
40. Hippocrates & Adams F (1938) *Hippocrates, selected works* (Edwards Brothers, Inc., Ann Arbor, Mich.,) p 109 p.
41. Ali A, Avalos RT, Ponimaskin E, & Nayak DP (2000) Influenza virus assembly: Effect of influenza virus glycoproteins on the membrane association of M1 protein. *Journal of Virology* 74(18):8709-8719.
42. Noda T, *et al.* (2006) Architecture of ribonucleoprotein complexes in influenza A virus particles. *Nature* 439(7075):490-492.
43. Chen RB & Holmes EC (2006) Avian influenza virus exhibits rapid evolutionary dynamics. *Mol Biol Evol* 23(12):2336-2341.
44. Centers_for_disease_control_and_prevention (2009) Influenza Virus Types, Subtypes, and Strains. <http://www.cdc.gov/flu/avian/gen-info/flu-viruses.htm>.
45. Nayak DP, Balogun RA, Yamada H, Zhou ZH, & Barman S (2009) Influenza virus morphogenesis and budding. *Virus research* 143(2):147-161.
46. Wilson IA, Skehel JJ, & Wiley DC (1981) Structure of the Hemagglutinin Membrane Glycoprotein of Influenza-Virus at 3-Å Resolution. *Nature* 289(5796):366-373.
47. Air GM & Laver WG (1989) The Neuraminidase of Influenza-Virus. *Proteins* 6(4):341-356.
48. Barman S, *et al.* (2004) Role of transmembrane domain and cytoplasmic tail amino acid sequences of influenza A virus neuraminidase in raft association and virus budding. *Journal of Virology* 78(10):5258-5269.
49. Pinto LH, Holsinger LJ, & Lamb RA (1992) Influenza-Virus M2 Protein Has Ion Channel Activity. *Cell* 69(3):517-528.
50. Izquierdo-Useros N, *et al.* (2012) Sialyllactose in Viral Membrane Gangliosides Is a Novel Molecular Recognition Pattern for Mature Dendritic Cell Capture of HIV-1. *Plos Biol* 10(4).
51. Sha BD & Luo M (1997) Structure of a bifunctional membrane-RNA binding protein, influenza virus matrix protein M1. *Nature structural biology* 4(3):239-244.
52. Martin K & Helenius A (1991) Nuclear transport of influenza virus ribonucleoproteins: the viral matrix protein (M1) promotes export and inhibits import. *Cell* 67(1):117-130.
53. Bucher DJ, *et al.* (1980) Incorporation of Influenza-Virus M-Protein into Liposomes. *Journal of Virology* 36(2):586-590.
54. Gregoriades A & Frangione B (1981) Insertion of Influenza M Protein into the Viral Lipid Bilayer and Localization of Site of Insertion. *Journal of Virology* 40(1):323-328.
55. Ruigrok RW, *et al.* (2000) Membrane interaction of influenza virus M1 protein. *Virology* 267(2):289-298.
56. Bui M, Whittaker G, & Helenius A (1996) Effect of M1 protein and low pH on nuclear transport of influenza virus ribonucleoproteins. *Journal of Virology* 70(12):8391-8401.
57. Nayak DP, Hui EK, & Barman S (2004) Assembly and budding of influenza virus. *Virus research* 106(2):147-165.

58. Calder LJ, Wasilewski S, Berriman JA, & Rosenthal PB (2010) Structural organization of a filamentous influenza A virus. *Proceedings of the National Academy of Sciences of the United States of America* 107(23):10685-10690.
59. Cros JF & Palese P (2003) Trafficking of viral genomic RNA into and out of the nucleus: influenza, Thogoto and Borna disease viruses. *Virus research* 95(1-2):3-12.
60. Russell RJ, *et al.* (2008) Structure of influenza hemagglutinin in complex with an inhibitor of membrane fusion. *Proceedings of the National Academy of Sciences of the United States of America* 105(46):17736-17741.
61. Smith AE & Helenius A (2004) How viruses enter animal cells. *Science* 304(5668):237-242.
62. Wagner R, Matrosovich M, & Klenk HD (2002) Functional balance between haemagglutinin and neuraminidase in influenza virus infections. *Rev Med Virol* 12(3):159-166.
63. van Riel D, *et al.* (2006) H5N1 virus attachment to lower respiratory tract. *Science* 312(5772):399-399.
64. Herfst S, *et al.* (2012) Airborne Transmission of Influenza A/H5N1 Virus Between Ferrets. *Science* 336(6088):1534-1541.
65. Imai M, *et al.* (2012) Experimental adaptation of an influenza H5 HA confers respiratory droplet transmission to a reassortant H5 HA/H1N1 virus in ferrets. *Nature* 486(7403):420-U163.
66. Kumar N, Liang YH, Parslow TG, & Liang YY (2011) Receptor Tyrosine Kinase Inhibitors Block Multiple Steps of Influenza A Virus Replication. *Journal of Virology* 85(6):2818-2827.
67. Naim HY & Roth MG (1994) Characteristics of the Internalization Signal in the Y543 Influenza-Virus Hemagglutinin Suggest a Model for Recognition of Internalization Signals Containing Tyrosine. *Journal of Biological Chemistry* 269(6):3928-3933.
68. Lakadamyali M, Rust MJ, & Zhuang X (2004) Endocytosis of influenza viruses. *Microbes and infection / Institut Pasteur* 6(10):929-936.
69. Marsh M & Helenius A (2006) Virus entry: open sesame. *Cell* 124(4):729-740.
70. Conner SD & Schmid SL (2003) Regulated portals of entry into the cell. *Nature* 422(6927):37-44.
71. Ghigo E, *et al.* (2008) Ameobal pathogen mimivirus infects macrophages through phagocytosis. *Plos Pathog* 4(6).
72. Nichols BJ & Lippincott-Schwartz J (2001) Endocytosis without clathrin coats. *Trends Cell Biol* 11(10):406-412.
73. Matlin KS, Reggio H, Helenius A, & Simons K (1981) Infectious Entry Pathway of Influenza-Virus in a Canine Kidney-Cell Line. *J Cell Biol* 91(3):601-613.
74. Sieczkarski SB & Whittaker GR (2002) Influenza virus can enter and infect cells in the absence of clathrin-mediated endocytosis. *Journal of Virology* 76(20):10455-10464.
75. Rust MJ, Lakadamyali M, Zhang F, & Zhuang X (2004) Assembly of endocytic machinery around individual influenza viruses during viral entry. *Nature structural & molecular biology* 11(6):567-573.
76. Hinrichsen L, Meyerhoiz A, Groos S, & Ungewickell EJ (2006) Bending a membrane: How clathrin affects budding. *Proceedings of the National Academy of Sciences of the United States of America* 103(23):8715-8720.
77. Sieczkarski SB & Whittaker GR (2003) Differential requirements of Rab5 and Rab7 for endocytosis of influenza and other enveloped viruses. *Traffic* 4(5):333-343.

78. Skehel JJ & Wiley DC (2000) Receptor binding and membrane fusion in virus entry: The influenza hemagglutinin. *Annual review of biochemistry* 69:531-569.
79. Yoshimura A & Ohnishi S (1984) Uncoating of Influenza-Virus in Endosomes. *Journal of Virology* 51(2):497-504.
80. Fields BN, Knipe DM, Howley PM, & Griffin DE (2001) *Fields virology* (Lippincott Williams & Wilkins, Philadelphia) 4th Ed pp xix, 3087 p.
81. Blaas D, Patzelt E, & Kuechler E (1982) Identification of the Cap Binding-Protein of Influenza-Virus. *Nucleic acids research* 10(15):4803-4812.
82. Braam J, Ulmanen I, & Krug RM (1983) Molecular-Model of a Eukaryotic Transcription Complex - Functions and Movements of Influenza-P Proteins during Capped Rna-Primed Transcription. *Cell* 34(2):609-618.
83. Bui M, Wills EG, Helenius A, & Whittaker GR (2000) Role of the influenza virus M1 protein in nuclear export of viral ribonucleoproteins. *Journal of Virology* 74(4):1781-1786.
84. Hirayama E, Atagi H, Hiraki A, & Kim J (2004) Heat shock protein 70 is related to thermal inhibition of nuclear export of the influenza virus ribonucleoprotein complex. *Journal of Virology* 78(3):1263-1270.
85. Kash JC, Goodman AG, Korth MJ, & Katze MG (2006) Hijacking of the host-cell response and translational control during influenza virus infection. *Virus research* 119(1):111-120.
86. Rossman JS & Lamb RA (2011) Influenza virus assembly and budding. *Virology* 411(2):229-236.
87. Barman S & Nayak DP (2000) Analysis of the transmembrane domain of influenza virus neuraminidase, a type II transmembrane glycoprotein, for apical sorting and raft association. *Journal of Virology* 74(14):6538-6545.
88. Schroeder C, Heider H, Moncke-Buchner E, & Lin TI (2005) The influenza virus ion channel and maturation cofactor M2 is a cholesterol-binding protein. *Eur Biophys J Biophys* 34(1):52-66.
89. Enami M, Sharma G, Benham C, & Palese P (1991) An Influenza-Virus Containing 9 Different Rna Segments. *Virology* 185(1):291-298.
90. Fournier E, *et al.* (2012) A supramolecular assembly formed by influenza A virus genomic RNA segments. *Nucleic acids research* 40(5):2197-2209.
91. Noda T, *et al.* (2012) Three-dimensional analysis of ribonucleoprotein complexes in influenza A virus. *Nat Commun* 3.
92. Gomez-Puertas P, Albo C, Perez-Pastrana E, Vivo A, & Portela A (2000) Influenza virus matrix protein is the major driving force in virus budding. *Journal of Virology* 74(24):11538-11547.
93. Latham T & Galarza JM (2001) Formation of wild-type and chimeric influenza virus-like particles following simultaneous expression of only four structural proteins. *J Virol* 75(13):6154-6165.
94. Roberts PC, Lamb RA, & Compans RW (1998) The M1 and M2 proteins of influenza A virus are important determinants in filamentous particle formation. *Virology* 240(1):127-137.
95. Liu T (2002) Association of Influenza Virus Matrix Protein with Ribonucleoproteins May Control Viral Growth and Morphology. *Virology* 304(1):89-96.
96. Bourmakina SV (2003) Reverse genetics studies on the filamentous morphology of influenza A virus. *Journal of General Virology* 84(3):517-527.
97. Rossman JS, *et al.* (2010) Influenza virus m2 ion channel protein is necessary for filamentous virion formation. *J Virol* 84(10):5078-5088.

98. Rossman JS, Jing X, Leser GP, & Lamb RA (2010) Influenza virus M2 protein mediates ESCRT-independent membrane scission. *Cell* 142(6):902-913.
99. Lee KK (2010) Architecture of a nascent viral fusion pore. *The EMBO journal* 29(7):1299-1311.
100. Lasic DD (1998) Novel applications of liposomes. *Trends Biotechnol* 16(7):307-321.
101. Lasic DD & Needham D (1995) The "Stealth" liposome: A prototypical biomaterial. *Chem Rev* 95(8):2601-2628.
102. Evans EA, Waugh R, & Melnik L (1976) Elastic, Area Compressibility Modulus of Red-Cell Membrane. *Biophysical journal* 16(2):A167-A167.
103. Evans EA (1974) Bending Resistance and Chemically-Induced Moments in Membrane Bilayers. *Biophysical journal* 14(12):923-931.
104. Helfrich W (1973) Elastic properties of lipid bilayers: theory and possible experiments. *Zeitschrift fur Naturforschung. Teil C: Biochemie, Biophysik, Biologie, Virologie* 28(11):693-703.
105. Bloom M, Evans E, & Mouritsen OG (1991) Physical-Properties of the Fluid Lipid-Bilayer Component of Cell-Membranes - a Perspective. *Q Rev Biophys* 24(3):293-397.
106. Rawicz W, Olbrich KC, McIntosh T, Needham D, & Evans E (2000) Effect of chain length and unsaturation on elasticity of lipid bilayers. *Biophysical journal* 79(1):328-339.
107. Lentz BR, Carpenter TJ, & Alford DR (1987) Spontaneous Fusion of Phosphatidylcholine Small Unilamellar Vesicles in the Fluid Phase. *Biochemistry* 26(17):5389-5397.
108. Lipowsky R & Sackmann E (1995) *Structure and dynamics of membranes* (Elsevier Science, Amsterdam ; New York) pp v. <1A-1B, >.
109. Scheiffele P, Rietveld A, Wilk T, & Simons K (1999) Influenza viruses select ordered lipid domains during budding from the plasma membrane. *Journal of Biological Chemistry* 274(4):2038-2044.
110. Polozov IV, Bezrukov L, Gawrisch K, & Zimmerberg J (2008) Progressive ordering with decreasing temperature of the phospholipids of influenza virus. *Nature chemical biology* 4(4):248-255.
111. Kwok R & Evans E (1981) Thermoelasticity of Large Lecithin Bilayer Vesicles. *Biophysical journal* 35(3):637-652.
112. Kummrow M & Helfrich W (1991) Deformation of Giant Lipid Vesicles by Electric-Fields. *Phys Rev A* 44(12):8356-8360.
113. Sakurai I & Kawamura Y (1983) Magnetic-Field-Induced Orientation and Bending of the Myelin Figures of Phosphatidylcholine. *Biochim Biophys Acta* 735(1):189-192.
114. Svoboda K, Schmidt CF, Branton D, & Block SM (1992) Conformation and Elasticity of the Isolated Red-Blood-Cell Membrane Skeleton. *Biophysical journal* 63(3):784-793.
115. Schneider MB, Jenkins JT, & Webb WW (1984) Thermal fluctuations of large quasi-spherical bimolecular phospholipid vesicles. *Journal de Physique* 45(9):1457-1472.
116. Duwe HP & Sackmann E (1990) Bending Elasticity and Thermal Excitations of Lipid Bilayer Vesicles - Modulation by Solutes. *Physica A* 163(1):410-428.
117. Meleard P, *et al.* (1997) Bending elasticities of model membranes: Influences of temperature and sterol content. *Biophysical journal* 72(6):2616-2629.
118. Liang XM, Mao GZ, & Ng KYS (2004) Probing small unilamellar EggPC vesicles on mica surface by atomic force microscopy. *Colloid Surface B* 34(1):41-51.
119. Hennesthal C & Steinem C (2000) Pore-spanning lipid bilayers visualized by scanning force microscopy. *J Am Chem Soc* 122(33):8085-8086.

120. Steltenkamp S, *et al.* (2006) Mechanical properties of pore-spanning lipid bilayers probed by atomic force microscopy. *Biophysical journal* 91(1):217-226.
121. Lenard J & Compans RW (1974) The membrane structure of lipid-containing viruses. *Biochim Biophys Acta* 344(1):51-94.
122. Sun X & Whittaker GR (2003) Role for Influenza Virus Envelope Cholesterol in Virus Entry and Infection. *Journal of Virology* 77(23):12543-12551.
123. Andreeva-Kovalevskaya ZI, Solonin AS, Sineva EV, & Ternovsky VI (2008) Pore-Forming Proteins and Adaptation of Living Organisms to Environmental Conditions. *Biochemistry-Moscow+* 73(13):1473.
124. Tosteson MT & Tosteson DC (1981) The Sting - Melittin Forms Channels in Lipid Bilayers. *Biophysical journal* 36(1):109-116.
125. Degrado WF, Musso GF, Lieber M, Kaiser ET, & Kezdy FJ (1982) Kinetics and Mechanism of Hemolysis Induced by Melittin and by a Synthetic Melittin Analog. *Biophysical journal* 37(1):329-338.
126. Wolfe SL (1993) *Molecular and cellular biology* (Wadsworth Pub. Co., Belmont, Calif.) pp xviii, 1145 p.
127. Vogel H & Jahnig F (1986) The Structure of Melittin in Membranes. *Biophysical journal* 50(4):573-582.
128. Farsad K & De Camilli P (2003) Mechanisms of membrane deformation. *Current Opinion in Cell Biology* 15(4):372-381.
129. Binnig G, Quate CF, & Gerber C (1986) Atomic Force Microscope. *Physical Review Letters* 56(9):930-933.
130. Grunewald K, *et al.* (2003) Three-dimensional structure of herpes simplex virus from cryo-electron tomography. *Science* 302(5649):1396-1398.
131. Fischer N, Konevega AL, Wintermeyer W, Rodnina MV, & Stark H (2010) Ribosome dynamics and tRNA movement by time-resolved electron cryomicroscopy. *Nature* 466(7304):329-333.
132. Carrasco C, Ares P, de Pablo PJ, & Gomez-Herrero J (2008) Cutting down the forest of peaks in acoustic dynamic atomic force microscopy in liquid. *Review of Scientific Instruments* 79(12).
133. Burnham NA, *et al.* (2003) Comparison of calibration methods for atomic-force microscopy cantilevers. *Nanotechnology* 14(1):1-6.
134. Proksch R, Schaffer TE, Cleveland JP, Callahan RC, & Viani MB (2004) Finite optical spot size and position corrections in thermal spring constant calibration. *Nanotechnology* 15(9):1344-1350.
135. Scheuring S, Reiss-Husson F, Engel A, Rigaud JL, & Ranck JL (2001) High-resolution AFM topographs of Rubrivivax gelatinosus light-harvesting complex LH2. *Embo Journal* 20(12):3029-3035.
136. Dufrene YF (2004) Using nanotechniques to explore microbial surfaces. *Nature Reviews Microbiology* 2(6):451-460.
137. Martinez-Martin D, *et al.* (2012) Resolving Structure and Mechanical Properties at the Nanoscale of Viruses with Frequency Modulation Atomic Force Microscopy. *Plos One* 7(1).
138. Horber JKH & Miles MJ (2003) Scanning probe evolution in biology. *Science* 302(5647):1002-1005.

139. Rief M, Gautel M, Oesterhelt F, Fernandez JM, & Gaub HE (1997) Reversible unfolding of individual titin immunoglobulin domains by AFM. *Science* 276(5315):1109-1112.
140. Kufer SK, Puchner EM, Gump H, Liedl T, & Gaub HE (2008) Single-molecule cut-and-paste surface assembly. *Science* 319(5863):594-596.
141. Machida S, *et al.* (2010) Direct manipulation of intracellular stress fibres using a hook-shaped AFM probe. *Nanotechnology* 21(38).
142. Ando T, *et al.* (2001) A high-speed atomic force microscope for studying biological macromolecules. *Proceedings of the National Academy of Sciences of the United States of America* 98(22):12468-12472.
143. Kodera N, Yamamoto D, Ishikawa R, & Ando T (2010) Video imaging of walking myosin V by high-speed atomic force microscopy. *Nature* 468(7320):72.
144. Ando T, *et al.* (2003) A high-speed atomic force microscope for studying biological macromolecules in action. *Chemphyschem* 4(11):1196-1202.
145. Casuso I, Kodera N, Le Grimellec C, Ando T, & Scheuring S (2009) Contact-Mode High-Resolution High-Speed Atomic Force Microscopy Movies of the Purple Membrane. *Biophysical journal* 97(5):1354-1361.
146. Fantner GE, Barbero RJ, Gray DS, & Belcher AM (2010) Kinetics of antimicrobial peptide activity measured on individual bacterial cells using high-speed atomic force microscopy. *Nat Nanotechnol* 5(4):280-285.
147. Han WH, Mou JX, Sheng J, Yang J, & Shao ZF (1995) Cryo Atomic-Force Microscopy - a New Approach for Biological Imaging at High-Resolution. *Biochemistry* 34(26):8215-8220.
148. Zhang YY, Sheng ST, & Shao ZF (1996) Imaging biological structures with the cryo atomic force microscope. *Biophysical journal* 71(4):2168-2176.
149. Zhang YY, Shao ZF, Somlyo AP, & Somlyo AV (1997) Cryo-atomic force microscopy of smooth muscle myosin. *Biophysical journal* 72(3):1308-1318.
150. Eghiaian F & Schaap IA (2011) Structural and dynamic characterization of biochemical processes by atomic force microscopy. *Methods Mol. Biol.* 778:71-95.
151. Nawaz S, *et al.* (2012) Cell Visco-Elasticity Measured with AFM and Optical Trapping at Sub-Micrometer Deformations. *Plos One* 7(9):e45297.
152. Dai J & Sheetz MP (1995) Mechanical properties of neuronal growth cone membranes studied by tether formation with laser optical tweezers. *Biophysical journal* 68(3):988-996.
153. B. Harke JVC, H. Haschke, C. Canale, A. Diaspro (2012) A novel nanoscopic tool by combining AFM with STED microscopy. *Optical Nanoscopy* 1(3).
154. Ivanovska I, Wuite G, Jonsson B, & Evilevitch A (2007) Internal DNA pressure modifies stability of WT phage. *Proceedings of the National Academy of Sciences of the United States of America* 104(23):9603-9608.
155. Bean B, *et al.* (1982) Survival of influenza viruses on environmental surfaces. *The Journal of infectious diseases* 146(1):47-51.
156. Larocca JN & Norton WT (2007) Isolation of myelin. *Current protocols in cell biology / editorial board, Juan S. Bonifacino ... [et al.]* Chapter 3:Unit3 25.
157. Hsu C, *et al.* (2010) Regulation of exosome secretion by Rab35 and its GTPase-activating proteins TBC1D10A-C. *J Cell Biol* 189(2):223-232.

158. O'Brien JS & Sampson EL (1965) Lipid composition of the normal human brain: gray matter, white matter, and myelin. *Journal of lipid research* 6(4):537-544.
159. Folch J, Lees M, & Stanley GHS (1957) A Simple Method for the Isolation and Purification of Total Lipides from Animal Tissues. *Journal of Biological Chemistry* 226(1):497-509.
160. Korte T, Ludwig K, Huang Q, Rachakonda PS, & Herrmann A (2007) Conformational change of influenza virus hemagglutinin is sensitive to ionic concentration. *Eur Biophys J Biophys* 36(4-5):327-335.
161. Bligh EG & Dyer WJ (1959) A Rapid Method of Total Lipid Extraction and Purification. *Can J Biochem Phys* 37(8):911-917.
162. Boettcher C, Pries C, & Vangent CM (1961) A Rapid and Sensitive Sub-Micro Phosphorus Determination. *Anal Chim Acta* 24(2):203-&.
163. Roschlau P, Bernt E, & Gruber W (1974) Enzymatic Determination of Total Cholesterol in Serum. *Z Klin Chem Klin Bio* 12(9):403-407.
164. Olson F, Hunt CA, Szoka FC, Vail WJ, & Papahadjopoulos D (1979) Preparation of Liposomes of Defined Size Distribution by Extrusion through Polycarbonate Membranes. *Biochim Biophys Acta* 557(1):9-23.
165. Mui B, Chow L, & Hope MJ (2003) Extrusion technique to generate liposomes of defined size. *Method Enzymol* 367:3-14.
166. Laney DE, Garcia RA, Parsons SM, & Hansma HG (1997) Changes in the elastic properties of cholinergic synaptic vesicles as measured by atomic force microscopy. *Biophysical journal* 72(2):806-813.
167. Haines TH (1994) Water Transport across Biological-Membranes. *FEBS letters* 346(1):115-122.
168. Blough HA (1971) Fatty Acid Composition of Individual Phospholipids of Influenza Virus. *Journal of General Virology* 12(Sep):317-&.
169. Huang RTC (1976) Sphingolipids of Influenza-Viruses. *Biochim Biophys Acta* 424(1):90-97.
170. Siegel GJ (2006) *Basic neurochemistry : molecular, cellular, and medical aspects* (Elsevier, Amsterdam ; Boston) 7th Ed pp xxiv, 992 p.
171. Delorme N & Fery A (2006) Direct method to study membrane rigidity of small vesicles based on atomic force microscope force spectroscopy. *Physical Review E* 74(3).
172. Feng F & Klug WS (2006) Finite element modeling of lipid bilayer membranes. *Journal of Computational Physics* 220(1):394-408.
173. Dimova R, Pouligny B, & Dietrich C (2000) Pretransitional effects in dimyristoyl-phosphatidylcholine vesicle membranes: Optical dynamometry study. *Biophysical journal* 79(1):340-356.
174. Schaap IAT, Carrasco C, de Pablo PJ, MacKintosh FC, & Schmidt CF (2006) Elastic response, buckling, and instability of microtubules under radial indentation. *Biophysical journal* 91(4):1521-1531.
175. De Benedictis P, Beato MS, & Capua I (2007) Inactivation of avian influenza viruses by chemical agents and physical conditions: A review. *Zoonoses Public Hlth* 54(2):51-68.
176. Labhasetwar V, Mohan MS, & Dorle AK (1994) A Study on Zeta-Potential and Dielectric-Constant of Liposomes. *J Microencapsul* 11(6):663-668.

177. Moncelli MR, Becucci L, & Guidelli R (1994) The intrinsic pKa values for phosphatidylcholine, phosphatidylethanolamine, and phosphatidylserine in monolayers deposited on mercury electrodes. *Biophysical journal* 66(6):1969-1980.
178. van Meer G, Voelker DR, & Feigenson GW (2008) Membrane lipids: where they are and how they behave. *Nat Rev Mol Cell Bio* 9(2):112-124.
179. Roos WH, Ivanovska IL, Evilevitch A, & Wuite GJ (2007) Viral capsids: mechanical characteristics, genome packaging and delivery mechanisms. *Cellular and molecular life sciences : CMLS* 64(12):1484-1497.
180. Klug W, *et al.* (2006) Failure of Viral Shells. *Physical Review Letters* 97(22).
181. Jin AJ, Prasad K, Smith PD, Lafer EM, & Nossal R (2006) Measuring the elasticity of clathrin-coated vesicles via atomic force microscopy. *Biophysical journal* 90(9):3333-3344.
182. Schonherr H, Johnson JM, Lenz P, Frank CW, & Boxer SG (2004) Vesicle adsorption and lipid bilayer formation on glass studied by atomic force microscopy. *Langmuir* 20(26):11600-11606.
183. Mui BLS, Cullis PR, Evans EA, & Madden TD (1993) Osmotic Properties of Large Unilamellar Vesicles Prepared by Extrusion. *Biophysical journal* 64(2):443-453.
184. Needham D, McIntosh TJ, & Evans E (1988) Thermomechanical and Transition Properties of Dimyristoylphosphatidylcholine Cholesterol Bilayers. *Biochemistry* 27(13):4668-4673.
185. Kol N, *et al.* (2006) Mechanical properties of murine leukemia virus particles: effect of maturation. *Biophysical journal* 91(2):767-774.
186. Nikolaus J, *et al.* (2010) Hemagglutinin of Influenza Virus Partitions into the Nonraft Domain of Model Membranes. *Biophysical journal* 99(2):489-498.
187. Sackmann E (1994) The seventh Datta Lecture. Membrane bending energy concept of vesicle- and cell-shapes and shape-transitions. *FEBS letters* 346(1):3-16.
188. Chen BJ, Leser GP, Morita E, & Lamb RA (2007) Influenza virus hemagglutinin and neuraminidase, but not the matrix protein, are required for assembly and budding of plasmid-derived virus-like particles. *J Virol* 81(13):7111-7123.
189. Korte T & Herrmann A (1994) Ph-Dependent Binding of the Fluorophore Bis-Ans to Influenza-Virus Reflects the Conformational Change of Hemagglutinin. *Eur Biophys J Biophys* 23(2):105-113.
190. Brand CM & Skehel JJ (1972) Crystalline antigen from the influenza virus envelope. *Nature: New biology* 238(83):145-147.
191. Harris A, *et al.* (2006) Influenza virus pleiomorphy characterized by cryoelectron tomography. *Proceedings of the National Academy of Sciences of the United States of America* 103(50):19123-19127.
192. Remeta DP, *et al.* (2002) Acid-induced changes in thermal stability and fusion activity of influenza hemagglutinin. *Biochemistry* 41(6):2044-2054.
193. Krumbiegel M, Herrmann A, & Blumenthal R (1994) Kinetics of the low pH-induced conformational changes and fusogenic activity of influenza hemagglutinin. *Biophysical journal* 67(6):2355-2360.
194. Helenius A, Kartenbeck J, Simons K, & Fries E (1980) Entry of Semliki Forest Virus into BHK-21-Cells. *J Cell Biol* 84(2):404-420.

195. Elms PJ, Chodera JD, Bustamante C, & Marqusee S (2012) The molten globule state is unusually deformable under mechanical force. *Proceedings of the National Academy of Sciences of the United States of America* 109(10):3796-3801.
196. Baudin F, Petit I, Weissenhorn W, & Ruigrok RWH (2001) In vitro dissection of the membrane and RNP binding activities of influenza virus M1 protein. *Virology* 281(1):102-108.
197. Ye Z, Liu T, Offringa DP, McInnis J, & Levandowski RA (1999) Association of influenza virus matrix protein with ribonucleoproteins. *J Virol* 73(9):7467-7473.
198. Le Blanc I, *et al.* (2005) Endosome-to-cytosol transport of viral nucleocapsids. *Nature cell biology* 7(7):653-U625.
199. Rachakonda PS, *et al.* (2007) The relevance of salt bridges for the stability of the influenza virus hemagglutinin. *Faseb J* 21(4):995-1002.
200. Fontana J, Cardone G, Heymann JB, Winkler DC, & Steven AC (2012) Structural Changes in Influenza Virus at Low pH Characterized by Cryo-Electron Tomography. *Journal of Virology* 86(6):2919-2929.
201. Finder C, Wohlgemuth M, & Mayer C (2004) Analysis of particle size distribution by particle tracking. *Part Part Syst Char* 21(5):372-378.
202. Einstein A (1905) Über die von der molekularkinetischen Theorie der Wärme geforderte Bewegung von in ruhenden Flüssigkeiten suspendierten Teilchen. *Annalen der Physik* 322(8):549-560.
203. Waterham HR (2002) Inherited disorders of cholesterol biosynthesis. *Clin Genet* 61(6):393-403.
204. Lein ES, *et al.* (2007) Genome-wide atlas of gene expression in the adult mouse brain. *Nature* 445(7124):168-176.
205. Hayashi H, Campenot RB, Vance DE, & Vance JE (2004) Glial lipoproteins stimulate axon growth of central nervous system neurons in compartmented cultures. *The Journal of biological chemistry* 279(14):14009-14015.
206. Funfschilling U, Saher G, Xiao L, Mobius W, & Nave KA (2007) Survival of adult neurons lacking cholesterol synthesis in vivo. *BMC neuroscience* 8:1.
207. Funfschilling U, *et al.* (2012) Critical Time Window of Neuronal Cholesterol Synthesis during Neurite Outgrowth. *J Neurosci* 32(22):7632-7645.
208. Raucher D & Sheetz MP (1999) Characteristics of a membrane reservoir buffering membrane tension. *Biophysical journal* 77(4):1992-2002.
209. Sheetz MP & Dai JW (1996) Modulation of membrane dynamics and cell motility by membrane tension. *Trends Cell Biol* 6(3):85-89.
210. Sun M, *et al.* (2005) Multiple membrane tethers probed by atomic force microscopy. *Biophysical journal* 89(6):4320-4329.
211. Sun M, *et al.* (2007) The effect of cellular cholesterol on membrane-cytoskeleton adhesion. *Journal of cell science* 120(Pt 13):2223-2231.
212. Lu YB, *et al.* (2006) Viscoelastic properties of individual glial cells and neurons in the CNS. *Proceedings of the National Academy of Sciences of the United States of America* 103(47):17759-17764.
213. Guck J, *et al.* (2005) Optical deformability as an inherent cell marker for testing malignant transformation and metastatic competence. *Biophysical journal* 88(5):3689-3698.

214. Hoffman BD & Crocker JC (2009) Cell Mechanics: Dissecting the Physical Responses of Cells to Force. *Annu Rev Biomed Eng* 11:259-288.
215. Kuznetsova TG, Starodubtseva MN, Yegorenkov NI, Chizhik SA, & Zhdanov RI (2007) Atomic force microscopy probing of cell elasticity. *Micron* 38(8):824-833.
216. Varnai P & Balla T (1998) Visualization of phosphoinositides that bind pleckstrin homology domains: calcium- and agonist-induced dynamic changes and relationship to myo-[3H]inositol-labeled phosphoinositide pools. *J. Cell. Biol.* 143(2):501-510.
217. Gittes F & Schmidt CF (1998) Signals and noise in micromechanical measurements. *Methods Cell Biol.* 55:129-156.
218. Vermeulen KC, Wuite GJL, Stienen GJM, & Schmidt CF (2006) Optical trap stiffness in the presence and absence of spherical aberrations. *Appl Optics* 45(8):1812-1819.
219. Gittes F & Schmidt CF (1998) Thermal noise limitations on micromechanical experiments. *Eur. Biophys. J. Biophys. Lett.* 27(1):75-81.
220. Mahaffy RE, Park S, Gerde E, Kas J, & Shih CK (2004) Quantitative analysis of the viscoelastic properties of thin regions of fibroblasts using atomic force microscopy. *Biophys. J.* 86(3):1777-1793.

CURRICULUM VITAE

Education

Ph.D. in Biophysics, November, 2012

“Atomic force microscopy study on the mechanics of influenza viruses and liposomes”

Georg-August-University of Goettingen, Goettingen, Germany

GGNB program-Physics of biological and complex systems

M.Sc. in Physics, 2008

“Thermal lens effect in an end-pumped Yb:KGW slab laser”

University of Stuttgart, Stuttgart, Germany

B.Sc. in Applied Physics, 2006

Wuhan University, Wuhan, China

Employment

Postdoctoral Research Fellow, Starting December, 2012

Wellcome Trust Centre for Human Genetics, University of Oxford, UK

Research experience

Doctoral thesis: ‘*Atomic force microscopy study on the mechanics of influenza viruses and lipid bilayers.*’ 01/2009-11/2012, Atomic force microscopy group, 3rd Physics Institute, Georg-August-University of Goettingen, Goettingen, Germany

(Supervisor: Dr. Iwan A. T. Schaap)

- Engaged in nanobiomechanics. Combined Atomic Force Microscopy (AFM) and Finite Element Methods (FEM) to investigate the mechanics of nanometer scale biological samples, focused on the mechanics of influenza virus envelopes protection and unpacking.
- Also participated in the studies of cell mechanics using AFM, FEM, optical tweezers and conventional microscopic methods.

Master thesis: ‘*Thermal lens effect in an end-pumped Yb:KGW slab laser*’

11/2007-11/2008, 4th physics Institute, University of Stuttgart, Stuttgart, Germany

(Supervisor: Dr. Felix Hoos, Prof. Dr. Harald Giessen)

- Studied the heat dissipation and thermal stress related thermo-mechanical deformation of laser crystal when heated by pump beam. Combined *Comsol* FEM and *Matlab* to simulate the thermal lens effect of laser crystal. Designed and constructed laser cavities. Measured focal length of the thermal lens experimentally.

- Contributed to construction of a high power femtosecond supercontinua white light laser.

Bachelor thesis: *'Quality factors of qubit rotations in single semiconductor quantum dots.'*

1/2006- 8/2006, Optics group, Department of Physics, Wuhan University, Wuhan, China

(Supervisor: Prof. Dr. Wang Ququan)

Research interests

Physical virology: mechanics of viruses; structural virology; viral activities

Mechanobiology: mechanics of cell, virus or other biological organisms

Bio-material: fabrication of bio-related materials; mechanics of bio-materials

Finite element modeling: simulation of mechanical process of complicated systems

Laboratory skills

Microscopy: Atomic force microscopy, Cryo-Electron microscopy, Confocal microscopy, TIRF microscopy

Other techniques: Optical tweezers, Dynamic light scattering, Time-Correlated Single Photon Counting, Differential scanning calorimetry

Computer skills

Finite Element Method (FEM): *Comsol Multiphysics*

Mathematical & programming: *Mathematica, Matlab, Origin, Labview, Igor*

Graphic and image processing: *Photoshop, AutoCAD, Coral Draw, WSxM*

Single particle tracking: *GMImpro, ImageJ*

Laser design: *Winlase*

Teaching experience

March-October 2011, Introduction in biophysics and complex systems, teaching assistant

September 2011, Mechanics of viruses, DPI summer school, lecturer

October 2011- February 2012, Physics laboratory, laboratory demonstrator

Professional memberships

DPG (German Physical Society), 2009-2012

CMPB (Research center molecular physiology of the brain, DFG), 2009-2010

SFB 860 (German collaborative research center), 2010-2012

Social services

At the University of Stuttgart:

Constructed and showed physical experiments in several scientific exhibitions for public educational purpose.

At the Georg-August-University of Goettingen:

05.2009 -10.2010: Member of the Chinese Student & Scholars' Association in Goettingen.

11.2009-now: Cofounder and director of the Goettingen Chinese Student & Scholars' Colloquium.

10.2010-08.2012: President of the Chinese Student & Scholars' Association in Goettingen.

Language proficiency

Chinese (Native)

English (fluent) (TOEFL, GRE)

German (satisfactory) (600 German class hours+6 years of stay in Germany)

Publications

pH-controlled two-step unpacking of influenza virus

[Sai Li](#), Christian Sieben, Frederic Eghiaian, Kai Ludwig, Andreas Herrmann and Iwan A.T. Schaap
Submitted

Cell visco-elasticity measured with AFM and optical trapping at sub-micrometer deformations

Schanila Nawaz, Paula Sanchez, Kai Bodensiek, [Sai Li](#), Mikael Simons, Iwan A. T. Schaap
PLoS ONE, (2012) 7, 9, e45297

Critical time window of neuronal cholesterol synthesis during neurite outgrowth

Ursula Fünfschilling, Wolf Jockusch, Nandhini Sivakumar, Wiebke Möbius, Kristina Corthals, [Sai Li](#), Susanne Quintes, Younghoon Kim, Iwan Schaap, Jeong-Seop Rhee, Klaus-Armin Nave, and Gesine Saher
Journal of Neuroscience, May 30, 2012 • 32(22):7632–7645

Bending and puncturing the influenza lipid envelope

[Sai Li](#), Frederic Eghiaian, Christian Sieben, Andreas Herrmann and Iwan A.T. Schaap
Biophysical Journal, 2011 Feb 2; 100 (3):637-45.
Featured article

Femtosecond high-power Yb:KGW slab laser oscillator pumped by a single broad-area diode

Felix Hoos, Todd Meyrath, [Sai Li](#), Bernd Braun, and Harald Giessen
Applied Physics B, (2009) 96: 5–10

Thermal lensing in an end-pumped Yb:KGW slab laser with high power single emitter diodes

Felix Hoos, [Sai Li](#), Todd Meyrath, Bernd Braun, and Harald Giessen
Optics Express, 16, 6041 (2008).

International conferences

March 2012, Berlin, Germany, **Annual conference of the German Physical Society** (DPG Frühjahrstagung)

Poster presentation: Unpacking the influenza virus at low pH

November 2011, Shanghai, China, **International Symposium on Mechanobiology** (The 5th Shanghai International Conference on Biophysics and Molecular Biology)

Oral presentation: Mechanics of influenza virus

January 2011, Ventura, California, USA, **Physical virology** (Gordon research conferences)

Poster presentation: Bending and puncturing the influenza lipid envelope

March 2011, Dresden, Germany, **Annual conference of the German Physical Society**

Oral presentation: Bending and puncturing the influenza lipid envelope

March 2010, Regensburg, Germany, **Annual conference of the German Physical Society**

Poster presentation: Physical properties of small unilamellar vesicles

ACKNOWLEDGEMENTS

It is difficult to find words to fully express my gratitude for Dr. Iwan A.T. Schaap. He introduced me into AFM and biophysics, and shed lights on the path of my exploration in science. I would not have gone this far without his guidance and encouragements. Being his first doctoral student, of which I am so proud, I have witnessed and participated in the establishment of this lab. His passion and attitude for science, his enthusiasm and diligence in work, his patience and kindness for others have all set examples to me, both in career and life.

Having a colleague like Dr. Frederic Eghiaian is as lucky as win a lottery. He played a crucial role in my transition from a physical to a biophysical student, since my basic knowledge of biology and bio-experimental skills were established with his guidance. None of my projects would have been accomplished without his participation. I am grateful and amazed about his enthusiasm in teaching me guitar, of course, charge free.

I deeply appreciate Christian Sieben and Prof. Andreas Herrmann from the Department of Biology, Humboldt-Universität zu Berlin. For the 2 projects we collaborated for almost 3 years, I was continuously supported by their biological samples and experiments. They warmly hosted my experiments in their lab.

I would like to thank Prof. Christoph Schmidt for creating a comfortable working environment. I would like to thank Prof. Bert de Groot and Prof. Andreas Janshoff for being my thesis committee members and their suggestions.

Thank all my colleagues in the III. Physikalisches Institut, especially my old officemates Alexander Benkstein and Kai Bodensiek, for their encouragements in weal and woe, and advices for my life in Germany.

I gratefully acknowledge CMPB (Research center molecular physiology of the brain) and SFB 860 (German collaborative research center No. 860) for financing my doctoral work, GGNB (Göttingen Graduate School for Neurosciences, Biophysics, and Molecular Biosciences) and PBCS (Physics of Biological and Complex Systems) for offering me various training opportunities and travel grants.

The 4-year experience in Goettingen is truly the highlight of my life. I have met more friends here than anywhere else, and I appreciate them for making my memories of Goettingen so colorful. I want to especially thank all the members of the Chinese Student and Scholars' Association during 2010-2012, together we worked hard to serve the Chinese community in Goettingen, and have won their respects.

Thank my parents so much. They always give me full freedom in having dreams and support me to achieve them. They never stop expressing their pride of me.

